EVALUATION OF VARIOUS ESTIMATION EQUATIONS FOR PARTICLE-FLUID INTERACTION FORCES AND MODELING OF HEAT TRANSFER BETWEEN PARTICLES FOR DEM SIMULATIONS

By

AZRI BIN ALIAS

Thesis for Doctor of Philosophy in Engineering
Okayama University of Science
Okayama City,
Okayama Prefecture,
Japan
2013

Thesis Approved:

Associate Professor Dr. Kuwagi Kenya
Thesis Advisor,
Dept. of Mechanical System Engineering,
Okayama University of Science

Professor Dr. Takami Toshihiro
Internal Examiner,
Dept. of Mechanical System Engineering,
Okayama University of Science

Professor Dr. Maruyama Yuuichi
Internal Examiner,
Dept. of Mechanical System Engineering,
Okayama University of Science

Professor Dr. Hirano Hiroyuki
Internal Examiner,
Dept. of Biotechnology and Applied Chemistry,
Okayama University of Science

Professor Dr. Yanase Shinichiro
External Examiner,
Graduate School of Natural Science and Technology,
Okayama University

ACKNOWLEDGMENTS

This dissertation would not have been possible without the guidance and the help of several individuals whose sincerity and encouragement I will never forget. These individuals in one way or another contributed and extended their valuable assistance in my thesis preparation and also the completion of my study at the Graduate School of Engineering, Okayama University of Science, Okayama Prefecture, Japan.

Firstly, I offer my sincerest gratitude to my supervisor, Dr Kuwagi Kenya, who has supported me throughout my research works with his patience and knowledge for almost6-7 years from my undegraduate study. Because of his friendlyness nature and his optimistic attitude, he always gives me the room to work in my own way and give a good guidance. He has been my inspiration as I hurdle all the obstacles in the completion this research work. I attribute the level of my Doctoral degree to his encouragement and effort and without him this thesis, too, would not have been completed or written. I simply could not wish for a better or friendlier supervisor than him.

Besides Dr. Kuwagi, I would also like to express my sincere appreciations to the fellow members of the PhD Examination Committee:

Dr. Takami Toshihiro, a Professor at the Department of Mechanical Systems Engineering, for being my second important supervisor at the lab. His outstanding ideas and advises during my final thesis defense has encouraged me to be more confident with my own research in the future. His energetic attitude also has kept me ready to endure the busy days at the university.

Dr. Hirano Hiroyuki, a Professor at the Department of Biotechnology and Applied Chemistry, for his amazing comments and discussions regarding my experimental results.

My study partially involved modifying several Fortran simulation codes which extensively contain those sub-routines written by him. I always felt I could turn to him if I had any questions or concerns.

Dr. Kataoka Katsumi, a Professor at the Department of Mechanical Systems Engineering, for his unselfish and unfailing support during the preparation of my dissertation thesis; I will never forget his friendly smiles and greetings every time we met.

Dr. Maruyama Yuuichi, a Professor at the Department of Mechanical Systems Engineering, for his teaching and support during my study. I will never forget his kindness and help during classes.

Dr. Yanase Shinichiro, a Professor at the Graduate School of Natural Science and Technology (Doctor Course), Division of Industrial Innovation Sciences at the Okayama University. I want to thank him for agreeing to undertake the role of being an External Examiner to my thesis dissertation. His assistance and advice was invaluable.

In the various laboratories and workshops I have been aided for many years in running the equipment by Mr. Muhammad Arif Mokhtar, who was my senior and he always teach and guided me toward my study. Also, I want to thank Mr. Shimoyama and also Mr Nakamoto, a graduate Master student for the long hours in the fields or lab to assist with data collection. I also would like to thank My Kogane this year he is firt year Master student because of his help. Also I want to thanks my colleagues and the staffs in the Mechanical Engineering Department for the use of facilities in the ME and EE Laboratory as well as Mechanical Engineering students whose undoubtly were assistance especially during the experimental works in the laboratory. I am also very thankful to numerous investigators in various branches of engineering disciplines whose technical and scientific reports are being cited in the thesis.

My great appreciation goes to Yayasan Pelajaran MARA (YPM) through HELP II and HELP III projects for making my life of student a start-to-finish success. YPM's financial support including university fees and living allowance for my undegradute studies has kept me in the right track as a student in Japan. Also, I would like to thanks University Malasyia Pahang for the financial support for my Master and PHd studies here.

Last but not the least, I would like to thanks my beloved family, my father Alias Bin Yahya, my mother Azma Binti Senun because of their full suppert in my study and also be patient of me. And also my brothers and sisters that has always supported me from the back.

And the One above all of us, Allah S.W.T, for answering my prayers every time I put my both hands in the air.

Thank You.

AZRI BIN ALIAS
10.6.2013

TABLE OF CONTENTS

LIST OF TABLES

LIST OF FIGURES

CHAPTER 1

INTRODUCTION

1.1 Research background

Fluidization is commonly defined as *“the operation by which the fine solids are transformed into a fluid-like state through contact with a gas or liquid”* [1]. This process occurs when a fluid whether a liquid or gas is passed up through the granular material. When a fluid flow is introduced from the bottom of a bed of solid particles, the fluid will move upwards through the bed via the empty spaces between the solid particles. At low fluid velocities, an aerodynamic drag on each particle is also low, and thus the bed remains in a fixed state. By this time, the static bed is called as a fixed fluidized bed. By increasing the velocity of the fluid flow, the aerodynamic drag forces will begin to counteract the gravitational forces, causing the bed to expand in volume as the particles move away from each other.

As further increasing in the fluid velocity, it will reach a critical value at which the upward drag forces will exactly equal to the downward gravitational forces, causing the particles to become suspended within the bed. At this critical value (minimum fluidization velocity), the bed is said to be fluidized and will exhibit fluidic behavior. By further increasing fluid velocity, the bulk density of the bed will continue to decrease, and its fluidization becomes more violent, until the particles no longer form a bed and conveyed upwards by the fluid flow.

When fluidization occured, a bed of solid particles will behave as a fluid, like a liquid or gas. The bed will conform to the volume of the chamber, its surface remaining perpendicular to gravity; objects with a lower density than the bed density will float on its surface, blobbing up and down if pushed downwards, while objects with a higher density sink to the bottom of the bed. These fluidic behavior allows the particles to be transported like a fluid, channeled through pipes and holes in machines. Thus, there is no need in requiring the mechanical transport (e.g. conveyer belt).

Fluidized beds are known for their high heat and mass transfer coefficients, due to the high surface area-to-volume ratio of fine particles. Fluidized beds are used in a wide variety of industrial processes such cracking and reforming of hydrocarbons, reaction, drying, mixing, granulation, gasification of coal, coating, heating and cooling as well as garbage burning process. An example of an industrial application of fluidized beds is circulating fluidized bed boiler type as shown in Figure 1.1 [2] and also the incinerator shown in Figure 1.2 [2].

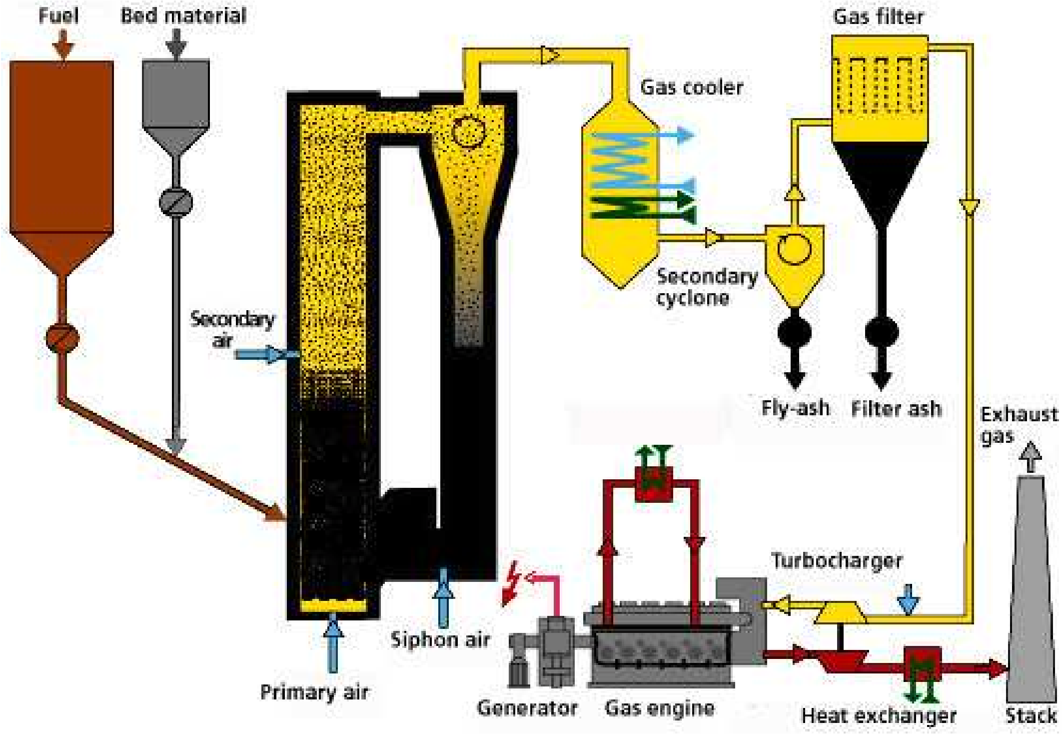

Figure 1.1: Example of circulating fluidized bed boiler type [2]

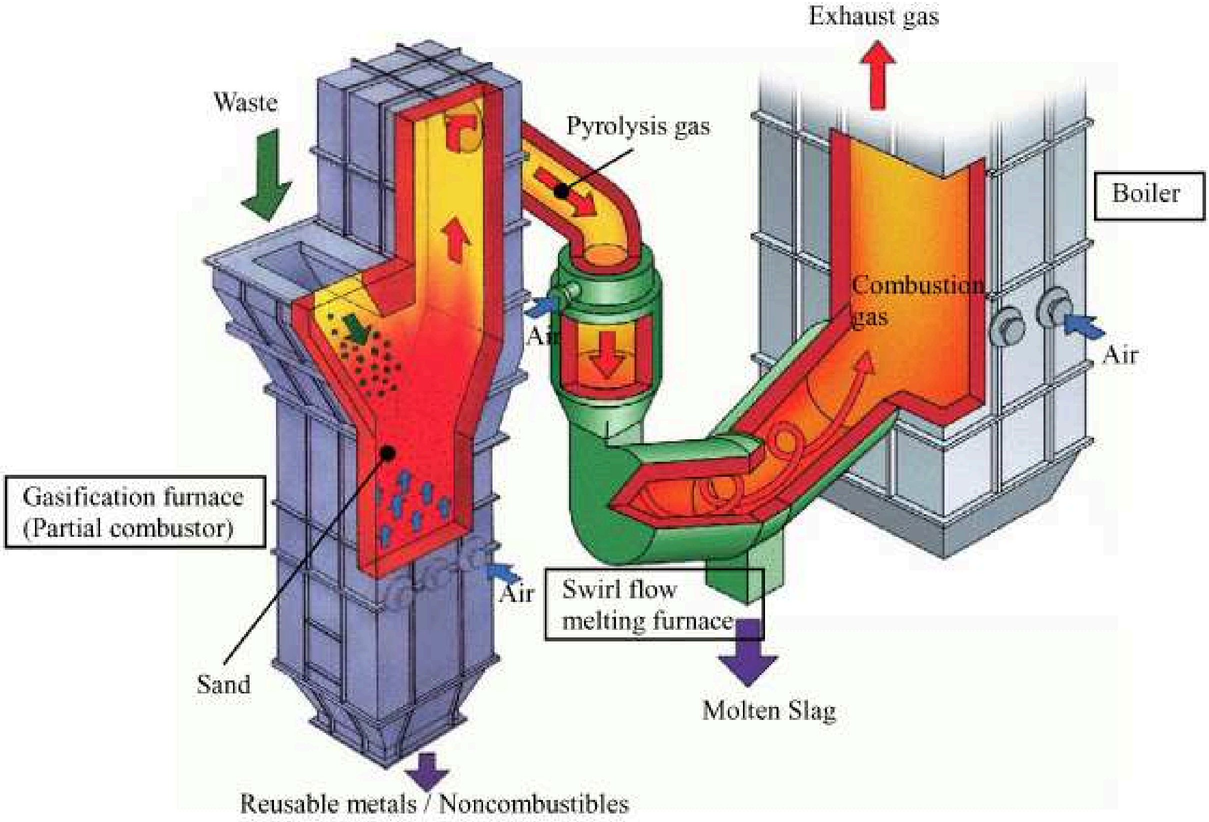

Figure 1.2: Example of the incinerator [2]

The phenomena in fluidization can be classified into a few group such as explained before. These group in fluidized bed can be called fixed bed, homogeneous fluidized bed, bubbling fluidized bed and also turbulant fluidized bed as shown in Figure 1.3.

Firstly, the explanation of fixed bed in fluidization. When a fluid of gas or liquid flow were injected from the bottom at a low rate of a bed made by solid particles, and the fluid were just pass through the void spaces of the bed without disturbing the movement of the bed it is called a fixed bed.

On the other hand, when pressure drop or the force acting on the solid particles, the fluid flowing through the bed equals or exceeds the weight of the particles bed, the fixed bed expended and the solids particle behave like a liquid behavior. This behaviour of the particles bed we called homogeneous fluidized bed. When the flow rates exceeds the minimum velocity of fluid, the solid particles bed expands and bubble seem to be appearing in the bed, it is called a bubbling fluidized bed.

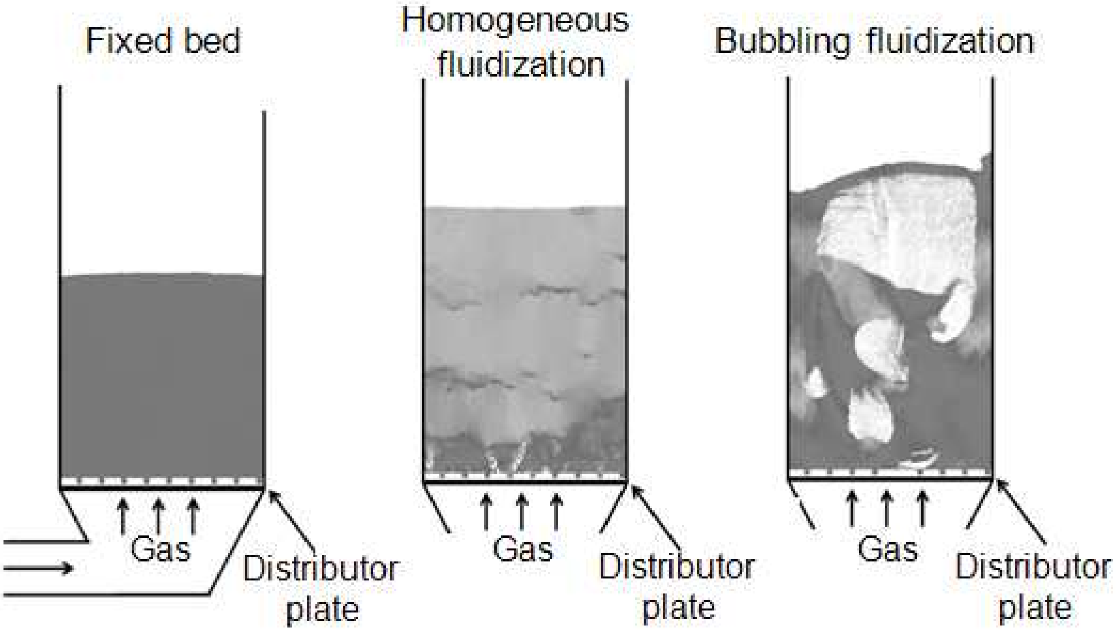

Figure 1.3: Classification of fluidized state with increased gas velocity

1.2 Application of fluidized bed in industrial

As we all know, there are a lot of applications of fluidization not only for the circulating fluidized bed (CFB) boiler and also incinerator but also in the gasoline refining as a catalyst and in the medicine manufacturing as granular and coating. The fluidized bed technology also was being applied mineral and metallurgical process.

Fluidized bed combustion (FBC) is the major application for the fluidization technology mainly used for power plants. Fluidized beds suspend solid fuels on upward-blowing jets of air during the combustion process. The result is a turbulent mixing of gas and solids. The tumbling action, much like a bubbling fluid, provides more effective chemical reactions and heat transfer. There is a rapid increase of FBC in combustors. The reasons are because of a lot of choice in respect of fuels in general, not only the possibility of using fuels which are difficult to burn using other technologies, is an important advantage of FBC. The second reason is which it has become increasingly important is because of the possibility of achieving, during combustion, a low emission of nitric oxides and the possibility of removing sulfur in a simple manner by using limestone as bed material. FBC were able to control pollutant emissions without external emission controls. The technology burns fuel at temperatures of 750-900°C well below the threshold where nitrogen oxides form at approximately 1400°C.

One of the new applicapable process is chemical looping combustion (CLC) [3] that are new application of fluidization technology which has not been yet commercialized. To reduce the potential effect of global warming, it is very important to sequestrate the carbon dioxide that was generated by fuel combustion such as in the power station. Gas nitrogen is mostly produce in regular combustion with air which prevents the economical sequestration. Chemical looping uses a metal oxide as a solid oxygen carrier. Metal oxide particles replace air to react with a solid, liquid or gaseous fuel in combustion, producing solid metal particles from the reduction of the metal oxides and a mixture of carbon dioxide and water vapor which is the major products of combustion reaction. The water vapor then was condensed, leaving pure carbon dioxide which can be sequestered.

As for the solid metal particles are circulated to another fluidized bed where they react with air, producing heat and regenerating metal oxide particles that are re-circulated to the fluidized bed combustor as shown in Figure 1.4 [4] below.

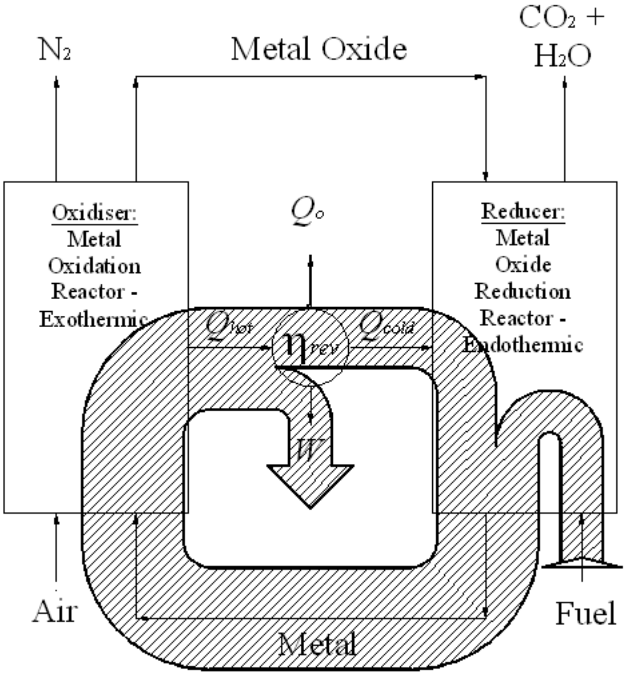

Figure 1.4: Sankey diagram of energy fluxes in a reversible CLC system [4]

1.3 Motivation and research purpose

1.3.1 Analysis on small scale phenomenon

As we all know, Discrete Element Method (DEM) is a very useful tool to analyze a fluidized bed for various powder processes also possible to incorporate problem–factors in the level of particle size. DEM is also used to investigate the hydrodynamic behavior of gas–solid interactions. However, in spite of the fact that DEM can be applied to problem pertaining to cohesion, heat transfer and chemical reaction, it is impossible to use DEM for dealing with phenomena whose scale is smaller than the particle size, such as the heat transfer between the colliding particles, the effect of drag, lubrication, and lift forces.

In DEM, there is equations for fluid and also particle motion equations. However, to make a more perfect simulation constitution, several equation are still needed. Some of the example are the equations for particle–fluid interaction force, such as drag, lift force and viscous torque. The heat transfer between the particles are also needed to incorporate with DEM.

In order to examine and clarify the small scale phenomena occurred in fluidized bed, we had utilized and experiments and also using a direct numerical simulations, such as IBM in this study.

CHAPTER 2

INTRODUCTION OF DISCRETE ELEMENT METHOD (DEM)

2.1 Introduction

With the improvements in computer performance in recent years, numerical simulation has been utilized in many various fields. In these present years, personal computer that cost around 10-20 thousand yen also has reached a commercial software are also available at the level 3D single phase flow heat computational fluid dynamics (CFD). The information such as the trouble factors, new process development that can reduce the risk that and also potential that cannot be obtained from the experiments can be easily obtained using the numerical simulations has become indispensable in industrial tools. This situation for the fluidized bed field also has no exception. One of the numerical method for solid-gas two phase flow with mixed powder that is DEM, were also become a mainstream in fluidized bed simulations.

2.2 Discrete Element Method

2.2.1 DEM in various numerical analysis method for solid-gas two-phase flow

The type and various of numerical analysis method for solid-gas two-phase flow is shown in Table 2.1.

Two-Fluid Model (TFM) for powder is a Euler basic (which treats the same way as a fluid), the number of particles is not limited and it is possible to analyze larger reactor relatively, this can be incorporated into a lot of commercial code. However, it is shown as "‘low”’ in table 2.1, because in powder industry problem, the particles adherence and the

Table 2.1: Numerical analysis method for solid-gas two-phase flow

	Fluid	Powder	Appicability	Computer load
Two-Fluid Model (TFM)	Euler	Euler	Low	Low
DSMC	Euler	Lagrange	Medium	Medium
DEM	Euler	Lagrange	Medium $\sim$ high	Medium $\sim$ high
DNS	Euler	Boundary	High	High

applicability to simulate various phenomena is difficult and also need to take into account.

In Direct Simulation Monte Carlo (DSMC), by representing one particle in the pack of particles, is a method that simulates stochastically collisions of the particles and it is effective for most systems that have a lot of particles. Tanaka *et al.* [5] have succeeded to simulate cluster formation in the riser of the circulating fluidized bed using this technique. It is an effective method for simulation of the circulating fluidized bed, however similar to TFM, the deposition of the particles is considered difficult.

The original DEM concept based was derived by Cundall and Strack [6] in the field of geo-mechanics. Discrete element method (Discrete Element Method, DEM) was developed by Tsuji *et al.* [7] by incorporating the Computer Fluid Dynamics (CFD) into the DEM. To distinguish the DEM from the original, they referred it as DEM + CFD model, but here we just assumed it to be simply expressed as DEM. In order to calculate the contact force of the particles (impact force), this approach has an advantage as the particles adhesion can be easily considered. However, there are also disadvantages in the DEM, such as the computation time is relatively long because of the need to reduce the time step of the calculation, and also the need to continue the calculation of the contact force with respect to all the contacting particles in the collision process.

However, due to advances in computer performance even a hundred thousand of particles can be calculated in 2D calculations, and it is also possible for a 3D calculation for a numbers of particles.It is believed that the benefits of DEM and the easiness of incorporating the reaction, heat transfer and particle adhesion, it seems researchers using DEM is also increased.

Finally, the Direct Numerical Simulation (DNS), is a method by providing computational mesh (grid) around the powder solved as boundary condition for the powder surface, and if necessary the calculation of the powder portion (for example, stress and also temperature field calculation). This technique predefined models to be used can be reduced and the accuracy of the information obtained the highest between the other methods, however, for this simulations the computer load is the greatest. For the present calculations, a need to limit the analysis region at a certion area, and it is used for the basic reserach. From the above points, numerical simulation of the fluidized bed, DEM is the mostly will be the mainstream for now.

2.3 Governing equations for DEM simulation

As described above, Euler treated at the fluid phase and Lagrangian treated at particle phase, the basic equation of DEM can be expressed as follows:

Fluid phase:

Equation of continuity

$$\frac{\partial(\varepsilon\rho_f)}{\partial t} + \nabla(\varepsilon\rho_f \boldsymbol{u}) = 0 \tag{2.1}$$

where ε is the fluid voidage and u is the upward superficial fluid velocity. The following equation denotes the momentum conservation of fluid:

Momentum conservation equation

$$\frac{\partial(\varepsilon\rho_f \boldsymbol{u})}{\partial t} + \nabla(\varepsilon\rho_f \boldsymbol{u}\boldsymbol{u}) = -\varepsilon\nabla p + \boldsymbol{F}_f + \varepsilon\rho_f \boldsymbol{g} \tag{2.2}$$

In the right-hand side of the above equation, $\boldsymbol{F}_f$ represents the force acting on the fluid cell from the particles. On the other hand, as described above, the particle motion is based on Newton's equation of motion and is described using the Lagrangian approach with two-way coupling between the fluid phase and the particle phase. This equation takes the following form:

$$\rho_{p(i)}(\frac{\pi}{6}d^3_{p(i)})\frac{d\boldsymbol{v}_{(i)}}{dt} = \sum_{i\neq j}\boldsymbol{F}_{p(ij)} + \boldsymbol{F}_{fp(i)} + \rho_{p(i)}(\frac{\pi}{6}d^3_{p(i)})\boldsymbol{g} + \boldsymbol{F}_{coh} \tag{2.3}$$

where $\rho_{p(i)}$ is the particle density, d_p is the particle diameter, and i, j denote the particle indices.

The next one is the equation of motion of the particle phase. The concepts are to unravel the expression based on the Newton's equation of motion to particles one by one respectivley. In the concentrated system where the contact of particles become dominant, as shown in Figure 2.1, at each normal direction and tangential direction, dashpot and spring are considered in DEM (the theoretical overlap amount) by calculating the amount of deformation of particles, the equations of motion are resolved based on the repulsive force. Based on the idea above, the equation of motion of particle i can be expressed as follow:

Normal direction

$$m_{pi}\frac{dv_i}{dt} = F_{fi} + \sum_{j\neq i}F_{nij} + m_{pi}g \tag{2.4}$$

The force caused by the tangential contact gives the particle a rotational motion. Thus, the torque balance equation for the rotational motion of the particle can be given by:

Tangential direction

$$I_i\frac{d\omega_i}{dt} = (\sum_{j\neq i}F_{tij})\cdot r_{pi} \tag{2.5}$$

Here, m_{pi} is particle mass, F_{fi} is particle-fluid interaction force(drag), F_{pij} is particle-fluid interaction force (contact force) for normal direction whereas F_{tij} is for tangential direction, and r_{pi} is particle radius.

The contact force can be obtained by the following equation modeling shown in Figure 2.1 below.

$$F_{nij} = kx_n - \eta \frac{dx_n}{dt} \tag{2.6}$$

$$F_{tij} = kx_t - \eta \frac{dx_t}{dt} \qquad\qquad (F_t < \eta F_n) \tag{2.7}$$

$$F_{tij} = \mu |F_{nij}| \frac{x_t}{|x_t|} \qquad\qquad (F_t < \eta F_n) \tag{2.8}$$

Here, k represent the spring rate, η repressent the damping coefficient, μ represent the friction coefficient whereas x_n and x_t represent the displacement for normal and tangential direction, respectively.

In non adherent particles where the heat transfer is not considered, it is well known that the contact force does not significantly affect the flow behavior, and in order to reduce computation time a much smaller value of linear spring is used than the actual spring rate.

However, in the actual plant, where the phenomena of particles adhesion, reaction, and heat transfer become a problem, it may depends on the contact time and also contact forces. So, in this kind of cases, the actual particle spring rate should be used or some correction should be done.

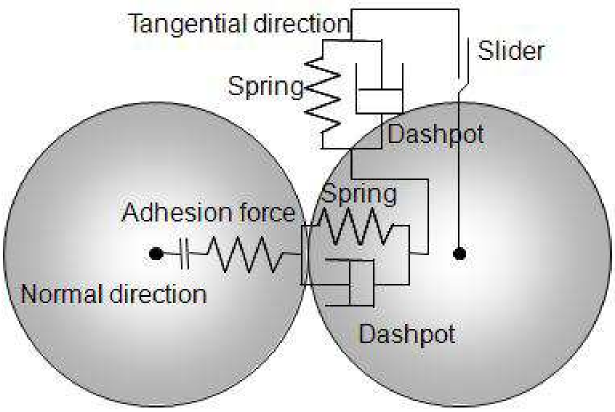

Figure 2.1: Model of particle contact force

2.4 Application of DEM in fluidization

The original DEM concept based on the soft sphere contacts was derived by Cundall and Strack [6] in the field of geomechanics. The DEM simulation technique has gained serious attention from academia and has spread through multiscale industries in which powder technology is applied. The key feature of the DEM is the ability to account for several realistic behaviors of particulate systems in numerical analyses, for example in agglomeration.

Mikami *et al.* [8] developed a numerical simulation code called SAFIRE (Simulation of Agglomerating Fluidization for Industrial Reaction Engineering) which took into account the liquid bridging force.

Following the work of Tsuji *et al.* [7], several researchers have attempted to incorporate real-world problems that occur in industrial fluidization processes into DEM simulations. These include cohesive forces, which mainly cause agglomeration and also maybe the clinker formation.

For metallic surface diffusion sintering, i.e., solid bridging force, Kuwagi *et al.* [9] simulated the process of sintering agglomerates and defluidization using the relationship between the neck growth time and the neck radius derived by Kuczynski [10].

Cohesive forces are not the only cause of problems in industrial processes that deal with particles and powders. Rong and Horio [11] developed the SAFIRE Ver. 6 simulation code for particle collision heat transfer and solid combustion. They successfully analyzed the thermodynamic characteristics and NO_x emission of burning chars in a fluidized bed.

These studies and others, have demonstrated the capability of the DEM as a powerful tool for investigating practical problems that occur in industrial particulate processes.

CHAPTER 3

AN ATTEMPT TO CALCULATE LIFT FORCE AND VISCOUS TORQUE OF A PARTICLE USING IMMERSED BOUNDARY METHOD (IBM)

3.1 Introduction

The gas-solid two-phase flow takes a very important role in various industries such as medicine manufacturing, food processing, and combustion or gasification of coal. Although these wide applications of the gas-solid two-phase flow have led to extensive researches, this phenomenon is very complicated and difficult to implement an experimental investigation of the flow characteristics. On the other hand, not only the abilities of computers, but also the numerical algorithms to solve the phenomena coupled of fluid and particles have been developed. As a result, numerical approaches have been introduced to design the powder processing industries.

The numerical simulation methods for gas-solid two-phase flow can be basically divided into three kinds of methods, i.e. the TFM (two-fluid model), the DEM (discrete element method) and CFD (computational fluid dynamics) coupling model, and the DNS (direct numerical simulation).

In the TFM, both gas (fluid) and solid (particle) phases are solved with Eulerian method, i.e. particles are treated as a fluid. On the other hand, in the DEM-CFD coupling model, the motion of each particle is solved with Lagrangian method, and the motion equation for all particles needs to be solved. Accordingly, the computational time of the DEM-CFD coupling model depends on the number of particles, and the computational load caused by the large number of particles sometimes brings serious problem. In these two models, some constitution equations for particle-gas interaction forces, e.g. drag and lift forces, are required. Meanwhile the DNS does not basically require any constitution equations for particle-gas interaction forces. So far various methods for the DNS have been derived, e.g. the finite element method (FEM), the boundary-fitted coordinates systems (BFC), the volume of fraction method (VOF), and the Immersed Boundary method (IBM).

In the previous studies on the gas-solid two-phase flow with the DNS approach, Pan *et al.* [12], carried out the direct numerical calculation of particulate flow using FEM with the methodology of the combination of a distributed Lagrange-multiplier-based fictitious domain method (DLM) and the operator splitting methods by Glowinski *et al.* [13]. Glowinski *et al.* [13], proposed the idea that the fluid fills the space inside as well as outside of the particle boundaries. The fluid flow problem was then posed as a one larger domain, which allows the regular mesh to be used in the whole analysis domain. As the larger domain is also time-independent, the same mesh can be used for the entire simulation domain, eliminating the need for repeated re-meshing. Although this method can save much time in the solution technique it requires the large amount of computer memory.

Although the DNS does not need any constitution equation for particle- fluid interaction forces, the validity of the algorithm and the program code should be examined. Kuwagi *et al.* [14] using IBM carried out the numerical computation to estimate the drag force acting on the system of dilute and dense particles by simulating the flow around each particle.

Kurose and Komori [15] using BFC, has carried out the three-dimensional direct numerical simulation to evaluate the drag and lift forces acting on the rotating rigid sphere in the range of particle Reynolds number Re_p 1 until 500. They found that the direction of the lift force acting on a rigid sphere at higher Reynolds number is opposite to the prediction by the low Reynolds number theory, and the lift force can be explained by considering the contributions of pressure and viscous force to the total lift in the flow separation.

The behaviour of lift force and lift coefficient with the DNS was also studied by Sugioka and Komori [16]. Drag and lift forces acting on a spherical water droplet in a homogeneous linear shear air flow were also studied and carried out on three-dimensional direct numerical simulation based on the cell (MAC) method by Sugioka and Komori [17]. The drag and lift forces on a rotating sphere in a solid body rotating flow were also investigated by Bluemink *et al.* [18].

Viscous flow induced by the slow rotation of a solid sphere immersed in an infinite incompressible viscous flow was studied by Takagi [19]. In the study, Takagi [19] derived a calculation of the viscous torque using a basis of Navier-Stokes equation. The viscous torque at low Reynolds number up to about $Re_{\mathrm{R}} = 12$ has been studied.

In the researches for various forces caused by a rotational motion of a spherical particle in flow, viscous torque that acting on an object rotating in a fluid anticipated was also studied by Grugel, [20]. Grugel has utilized the Stokes' and Newton's models of a viscous drag force that are commonly used to describe the damping force acting on an object moving through a fluid and it was found that viscous torque and angular velocity is dependent on the shape of the object.

The dominant factors in the gas-particle two-phase systems, e.g. particle-gas and particle-particle interaction forces, can vary due to particle concentration. For instance, while particle-particle collision is dominant in dense-particle system, various particles-gas interaction forces, e.g. drag and lift forces, and viscous torque, are dominant in dilute-particle system. Saffman *et al.* [21] considered single stationary particles with no initial spin by the flow with the velocity gradient and the Saffman lift force was obtained by a series of Navier-Stokes equations. The lift force caused by the rotational motion by a particle in a uniform flow was called Magnus force (Magnus *et al.* [22]). From the study, these two additional forces, Saffman and Magnus forces are both important in both low and high Reynolds number.

In this chapter of study, an attempt to estimate the lift forces (Saffman force and Magnus force) and viscous torque in the various gas-solid two-phase flow systems using the DNS with the IBM.

3.2 Numerical Analyses

3.2.1 Differences between IBM and DEM

In this study, we have used the body-force-type IBM proposed by Kajishima *et al.* [23]. Here, we will be described and compared the differences between IBM and DEM.

Figure 3.1 below represents the difference in the size of the simulation mesh of IBM and DEM. In these two figures for the left and right hand, the particles in green colors were defined as the same size particles. On the left hand side is DEM, the average of the fluid velocity is expressed as one speed in one cell. Here, as one cell is a few times greater than the particles, it is impossible to determine the behavior of the phenomenon below the particle scale. Thus, to determine the behavior below the particles scale, it is necessary to use an experimental analysis and other methods, such as DNS.

On the other hand, one of the DNS that is IBM, the numerical simulation treated the particles boundary condition as a solid wall, and from the figure on the right hand side, one cell is smaller than the particles, it is possible to determine the behavior below the particles scale such as lift, drag force and also viscous torque.

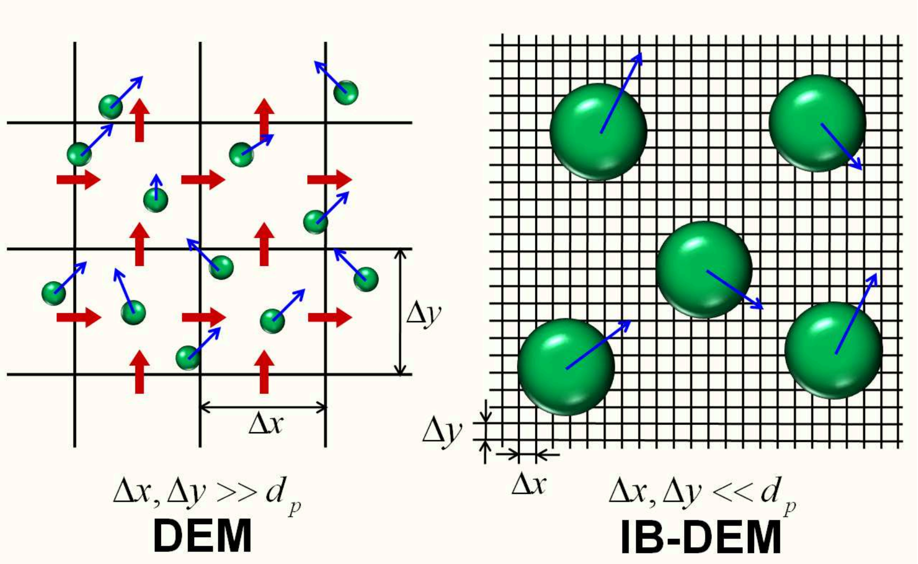

Figure 3.1: Difference between the simulation mesh of IBM and DEM

3.2.2 Calculation flow of IBM

Figure 3.2 represents the calculation procedure of the body force type IBM. In IBM, the particles are solved as it does not exist first. It means that, at first the entire calculation regions were solved as the fluid in figure (a). However, in fact there are particles in the calculation region; it should be the particle velocity in the calculation cell that has the particle. Therefore, the volume force is calculated in order to force the particle velocity in a particle cell (b). Then the volumetric force then forced as particle velocity as shown in (c). Then, the forces and moments acting by the fluid can be determined by the volume integral of the body force.

The calculation of time can be proceeds and become possible by repeating the following steps below.

1. In each calculation cell, volume fraction of the particles is calculate
2. The fluid are calculated from an equation (3.1) and (3.2) and velocity field are seek
3. The force were determined by (3.3)
4. Velocity of the coupling velocity field is modified
5. The forces acting on particles are calculated
6. The particles velocity, angular velocity, and position are updated

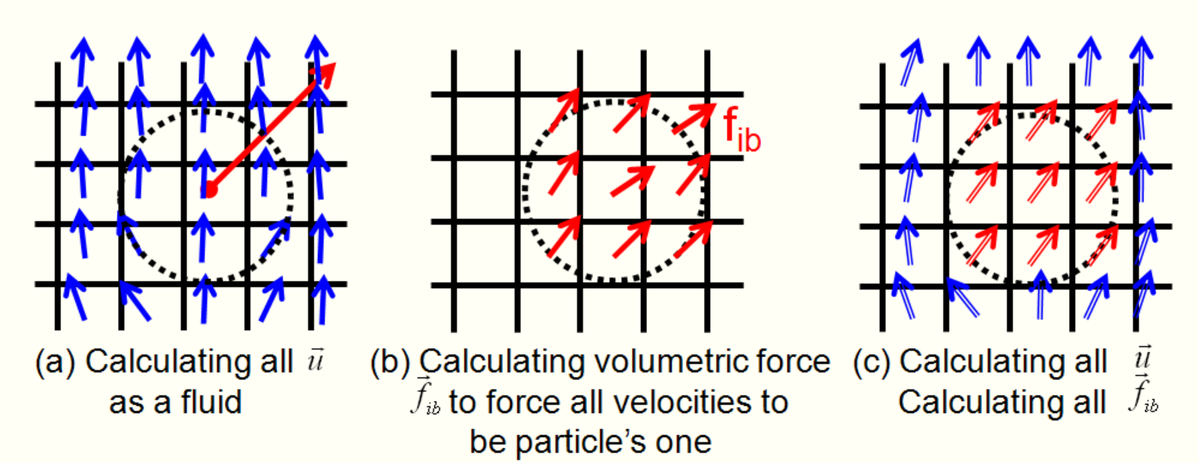

Figure 3.2: Calculation procedure of the body force type IBM

3.2.3 Introduction of IBM

The IBM was applied to analyses and calculate the drag force acting on particles. Deen *et al.* [24] simulated a complex multi–fluid flow by using a model that combined the front tracking (FT) model, developed by van der Hoef *et al.* [25], and the IBM. However, the numerical procedure for the FT model is relatively complicated. On the other hand, the body–force–type IBM developed by Kajishima *et al.* [23] provides a simple numerical procedure. Therefore, the IBM was adopted in the present numerical study. The governing equations are as follows:

Gas phase,

The equations for mass and momentum conservations are as follows:

$$\nabla \cdot u = 0 \tag{3.1}$$

$$\frac{D\vec{u}}{Dt} = -\frac{1}{\rho_g}\nabla p + \vec{f}_{\mathrm{vis}} + \vec{f}_{\mathrm{ib}} + \vec{g} \tag{3.2}$$

where $\vec{f}_{\mathrm{ib}}$ is the body force term. Because of this force, the velocity of a particle in a fluid cell is equal to the velocity in the cell. In the present simulation, the following equation (Kajishima *et al.*, [23]) was used.

$$\vec{f}_{\mathrm{ib}} = \frac{\varepsilon_{\mathrm{p}}(\vec{\nu}_{\mathrm{p}} - \vec{u})}{\Delta t} \tag{3.3}$$

The particle volume fraction ε_p at a computational cell including an interface between gas and solid was calculated with the method using sub-mesh system proposed by Tsuji *et al.* [26].

Particle phase,

The motion equations in the translational and rotational directions are as follows:

$$\frac{\mathrm{d}(m_\mathrm{p}\vec{\nu}_\mathrm{p})}{\mathrm{d}t} = -\rho_g \int_{V_\mathrm{p}} \vec{f}_\mathrm{ib}\mathrm{d}V + \sum_{j\neq 1} \vec{F}_\mathrm{nij} + m_\mathrm{p}\vec{g} \tag{3.4}$$

$$\frac{\mathrm{d}(\vec{I}_\mathrm{p} \cdot \vec{\omega}_\mathrm{p})}{\mathrm{d}t} = -\rho_g \int_{V_\mathrm{p}} r_\mathrm{p} \times \vec{f}_\mathrm{ib}\mathrm{d}V + \left(\sum_{j\neq 1} \vec{F}_\mathrm{tij} \right) \cdot r_\mathrm{p} \tag{3.5}$$

where the second term on the right-hand side in equation (3.4) denotes the particle–particle interaction force, i.e., the collision force in the direction normal to a particle's surface at the contact point. The second term on the right–hand side in equation (3.5) denotes the particle–particle interaction moment. $\vec{F}_\mathrm{tij}$ is the contact force in the tangential direction, and r_p is the particle radius. Since only one particle was treated in this study, these terms naturally become zero.

In the standard DNS, the particle-fluid interaction force is usually calculated using the surface integral of the stress acting on a particle surface. On the other hand, in the body–force–type IB method, it is calculated using the volume integral of the body force term $\vec{f}_\mathrm{ib}$, represented by the first term on the right-hand side in equation (3.4). The angular momentum equation can be calculated using this body force term too, given by equation (3.5).

3.3 Analysis conditions

The schematic of the problem is shown in Figure 3.3. A single spherical particle was set at the center of the analysis domain for calculation of the lift forces in case 1-1, 1-2, 2-1, 2-2, and 2-3 and in viscous torque analyses, whereas the spherical particle sphere was set at one third of the analysis domain for the other case of the lift forces.

Figure 3.3 shows the basic analysis domain for the spherical particle sphere set at the center of the analysis domain. The thickness of the domain basically was set to be equal to the particle diameter. However, the thickness was changed in some simulations to examine the effect of analysis domain size. The size of the analysis area and calculation mesh was also changed to examine the accuracy of the model.

For the simulation in Saffman force, the fluid flow with dimensionless velocity gradient is injected from the bottom wall in a of the domain area and for the Magnus force simulation, the fluid flow in injected from the bottom wall equally with rotating spherical particle, for viscous torque, while no fluid flow is injected, only the particle rotates.

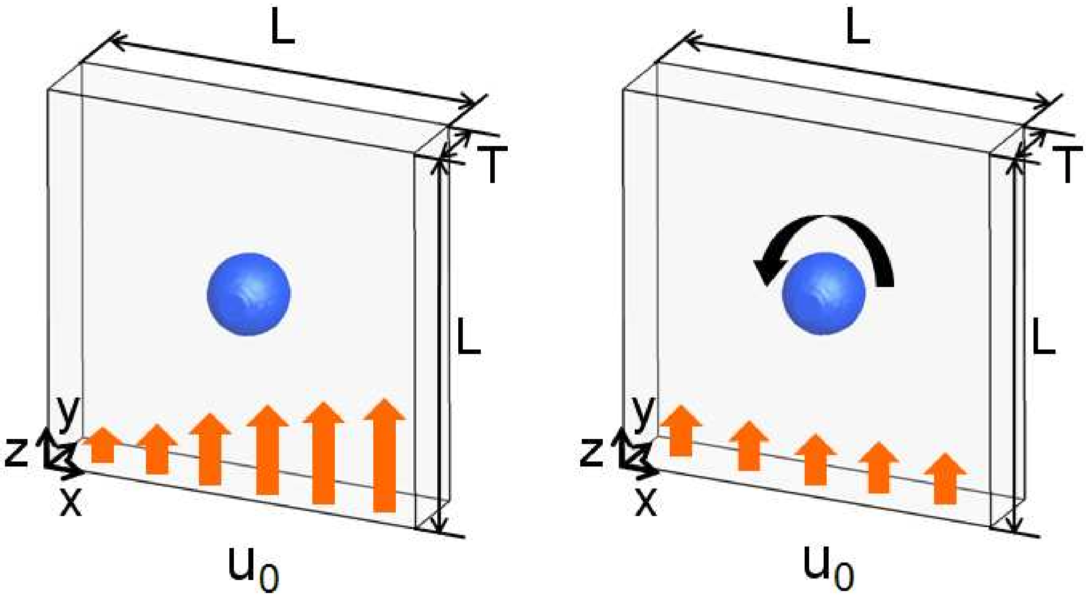

(a) Saffman force (b) Magnus force

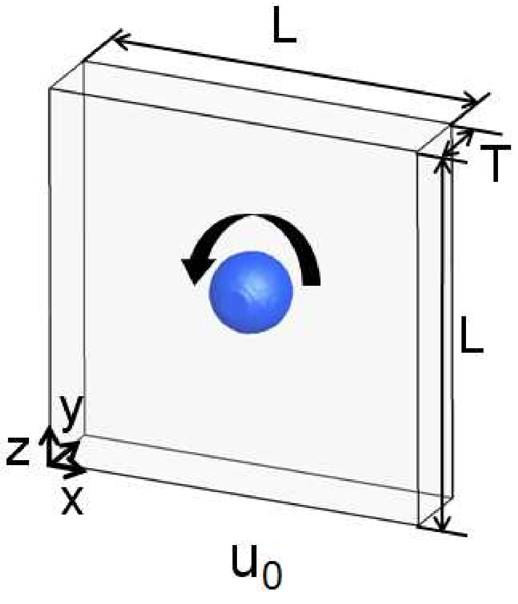

(c) Viscous torque

Figure 3.3: Schematic of the problem

3.3.1 Numerical procedure

Time discretization was approximated by an explicit method and the inertial terms by 3rd order up-wind scheme. The pressure distribution was solved with the HS-MAC (SOLA) method. The boundary conditions for lift force and viscous torque analyses are as follows:

$$u_x = u_y = 0, \frac{\partial u_z}{\partial x} = 0 \quad \text{at } x = 0, L \text{ (} u_z = 0 \text{ for viscous torque analysis)} \tag{3.6}$$

$$u_y = 0, \frac{\partial u_x}{\partial y} = \frac{\partial u_z}{\partial y} = 0 \text{ (planes of } y = 0 \text{ and } T \text{)} \tag{3.7}$$

$$u_x = u_y = 0, u_z = u_0 \quad \text{at } z = 0 \text{ (} u_z = 0 \text{ for viscous torque analysis)} \tag{3.8}$$

$$\frac{\partial u_x}{\partial z} = \frac{\partial u_y}{\partial z} = \frac{\partial u_z}{\partial z} \quad \text{at } z = L \text{ (} u_x = u_y = u_z = 0 \text{ for viscous torque analysis)} \tag{3.9}$$

In equation 3.8, for the velocity u_0, in Saffman lift force, the lift force caused by the flow with the velocity gradient injected from the the bottom wall and for Magnus lift force, the flow was injected at the bottom wall equally whereas for the viscous torque, no fluid flow was injected.

The simulated results were examined in the terms of lift coefficient and dimensionless torque against particle Reynolds number and particle rotation Reynolds number which are defined as follows:

$$C_{\mathrm{L}} = \frac{F_{\mathrm{L}}}{\frac{1}{2}\rho_{\mathrm{g}} u^2 A} \tag{3.10}$$

$$C_{\mathrm{LR}} = \frac{F_{\mathrm{LR}}}{\frac{1}{2}\rho_{\mathrm{g}} \frac{|\vec{u}_{\mathrm{r}}|}{|\vec{\omega}_{\mathrm{r}}|} \vec{u_{\mathrm{r}}} \times \vec{\omega}_{\mathrm{r}} A} \qquad \vec{\omega}_{\mathrm{r}} = \vec{\omega}_{\mathrm{p}} - \frac{1}{2}\vec{\omega}_{\mathrm{g}} \tag{3.11}$$

$$C_{\mathrm{T}} = \frac{-T_{\mathrm{f}}}{\frac{1}{2}\rho_{\mathrm{g}} r^5 |\vec{\omega}_{\mathrm{r}}| \vec{\omega}_{\mathrm{r}}} \tag{3.12}$$

$$Re_{\mathrm{p}} = \frac{\rho_{\mathrm{g}} d_{\mathrm{p}} |\vec{u}_{\mathrm{r}}|}{\mu_{\mathrm{g}}} = \frac{d_{\mathrm{p}} |\vec{u}_{\mathrm{r}}|}{\nu_{\mathrm{g}}} \tag{3.13}$$

$$Re_{\mathrm{R}} = \frac{|\vec{\omega}_{\mathrm{r}}| {d_{\mathrm{p}}}^2}{4\nu_{\mathrm{g}}} \tag{3.14}$$

The computational simulation mesh is shown in Figure 3.4. In order to calculate the volume fraction of fluid or phase particle in all simulation meshes at the interface of fluid and particle are further divided into smaller size of mesh which we called sub-mesh proposed by Tsuji [26]. Compared with the method proposed by Kajishima [23], that by Tsuji [26], provides easier algorithm.

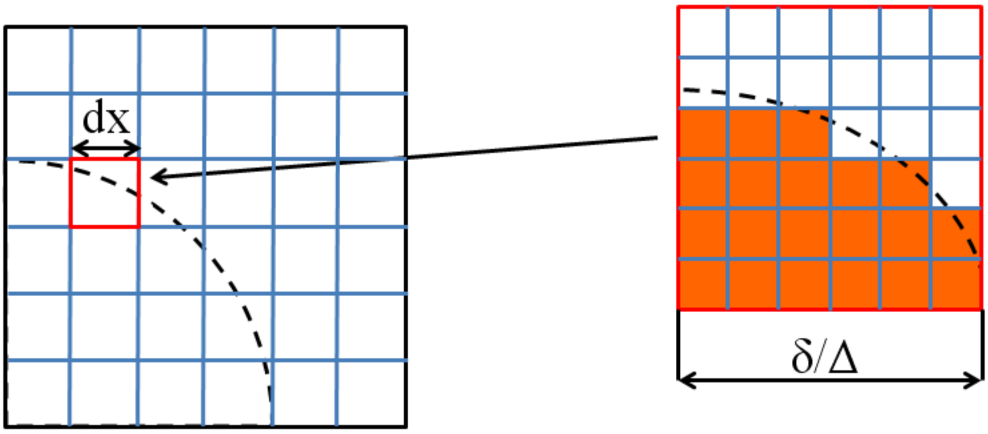

Figure 3.4: Computational mesh calculation for IB method

The analysis conditions for the lift forces and viscous torque are shown in the Table 3.1. The particle diameter used in the simulation is 1.0mm whereas the gas properties are as shown in table 1. In the case of Saffman force, the dimensionless velocity gradient of fluid used is $a^* = 0.1$.

Table 3.1: Simulation conditions

Particle diameter $[m]$	$1.0 \times \ 10^{-3}$
Particle density $[kg/m^3]$	$2.65 \times \ 10^{3}$
Particle number	1
Gas density $[kg/m^3]$	1.20
Gas viscosity $[Pas]$	$1.86 \times \ 10^{-5}$
Case 1 (Saffman force)	
Particle Reynolds number Re_{p} [-]	$1.374, 3.434, 13.74, 68.68, 137.4, 274.4, 480.8$
Dimensionless velocity gradient : $a^* = \frac{r_{\mathrm{p}} \partial w}{w_{\mathrm{i}} \partial x}$	0.1
Case 2 (Magnus force)	
Particle Reynolds number Re_{p} [-]	$1.099, 5.495, 32.97, 65.93, 82.42, 109.9$
Rotation Reynolds number Re_{R} [-]	$0.137, 0.275, 0.412, 0.549, 0.687, 1.374$
Case 3 (Viscous torque)	
Rotation Reynolds number Re_{R} [-]	$0.137, 0.275, 0.412, 0.549, 0.687, 1.374$

The sizes of the analysis area and simulation mesh size are shown in Table 3.2. The sizes of the analysis area, particle diameter mesh size calculated and set as the case number. The ratio of the size of the analysis area L/d_p is 5 or 10, whereas the ratio of the thickness of the analysis area to the particle diameter T/d_p is 1 or 5 to the particles diameter. the ratio of the simulation mesh size Δ, was changed from 1/10 to 1/20, whereas the ratio of the simulation sub-mesh size to the mesh size δ/Δ, was also changed to 4, 10, 15, and 20 times smaller to study the effect on the volume fraction.

Table 3.2: Analysis area and calculation mesh conditions

Case number	L/d_p	T/d_p	Δ/d_p	δ/Δ
1-1	5	1	1/10	1/4
1-2	5	5	1/10	1/4
1-3	10	1	1/10	1/4
1-4	10	1	1/20	1/4
1-5	10	1	1/10	1/10
1-6	10	1	1/10	1/15
1-7	10	1	1/10	1/20
2-1	5	1	1/10	1/4
2-2	5	5	1/10	1/4
2-3	5	1	1/20	1/4
2-4	10	1	1/10	1/4
2-5	10	1	1/20	1/4
2-6	10	1	1/10	1/10
2-7	10	1	1/10	1/15
2-8	10	1	1/10	1/20
3-1	5	1	1/10	1/4
3-2	10	1	1/10	1/4
3-3	5	1	1/20	1/4
3-4	5	1	1/10	1/10
3-5	5	1	1/10	1/15

Δ : Simulation mesh size

δ : Simulation sub- mesh size

3.4 Results and Discussion for chapter 3

3.4.1 Saffman force

The lift coefficient of Saffman force which is the lift force caused by the flow with velocity gradient acting around a particle sphere are studied using the immersed boundary method. In order to confirm the accuracy of the present simulation, the simulated results were compared with the results by McLaughlin [27] and Kurose and Komori [15].

Figure 3.5 shows the streamlines from the bottom wall at the dimensionless velocity gradient of fluid $a^* = 0.1$. The streamlines were drawn at the center of the analyses domain and the Reynolds number at $Re_\mathrm{p} = 1.37$ for all the cases. Cases 1-1 and 1-2 show the streamlines for the same length of analysis and simulation mesh size Δ/d_p at 1/10 with simulation sub-mesh size δ/Δ at 1/4. However, the thickness of case 1-2 is 5 times larger than case of 1-1. From the streamlines, there are not much differences in the figure of cases 1-1 and 1-2, shows that the thickness of the analysis domain did not affect much of the simulation analyses.

In cases of 1-3 and 1-4, the domain analysis size is 2 times larger than case 1-1 and 1-2. The simulation mesh size were also changed to Δ/d_p at 1/10 and 1/20 in cases 1-3 and 1-4 but the simulation sub-mesh was not change in both cases. The simulation mesh size for case 1-5 to case 1-7 has been change from 1/10, 1/15, and 1/20. In cases 1-1 and 1-4, the domain size of case 1-4 is 2 times bigger than case 1-1, but as the simulation mesh size also two times smaller, it is considered that the cases are almost the same but only differences in the simulation sub-mesh size. From these results, although they have different analysis domain, simulation mesh and simulation sub-mesh size, there is not much differ in the streamlines.

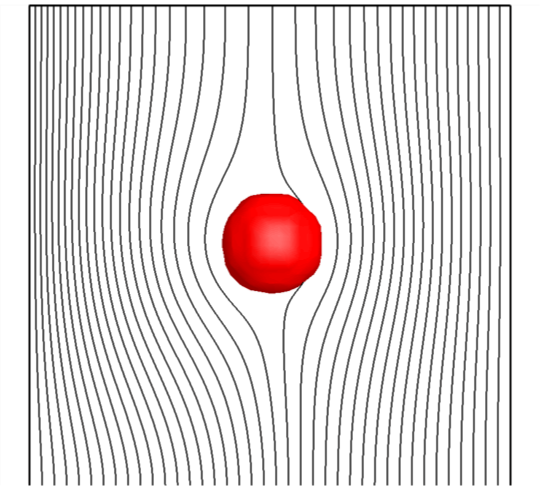

(a) Case 1-1 $\mathrm{Re_p} = 1.37$

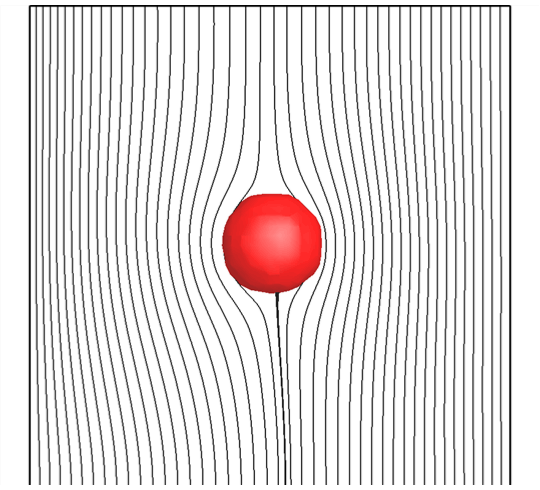

(b) Case 1-2 $\mathrm{Re_p} = 1.37$

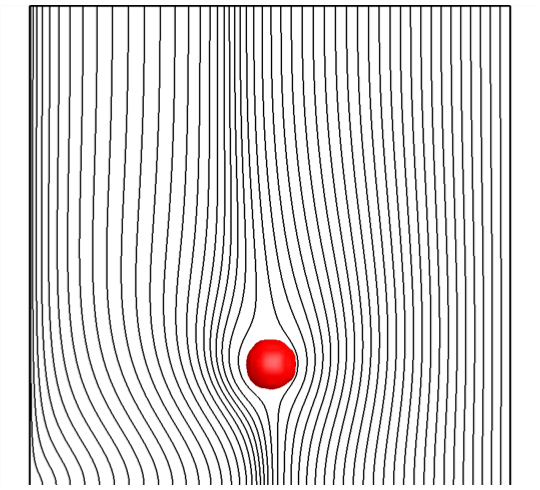

(c) Case 1-3 $\mathrm{Re_p} = 1.37$

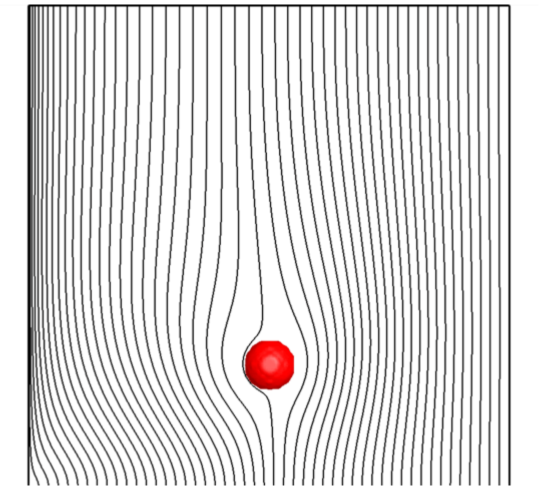

(d) Case 1-4 $\mathrm{Re_p} = 1.37$

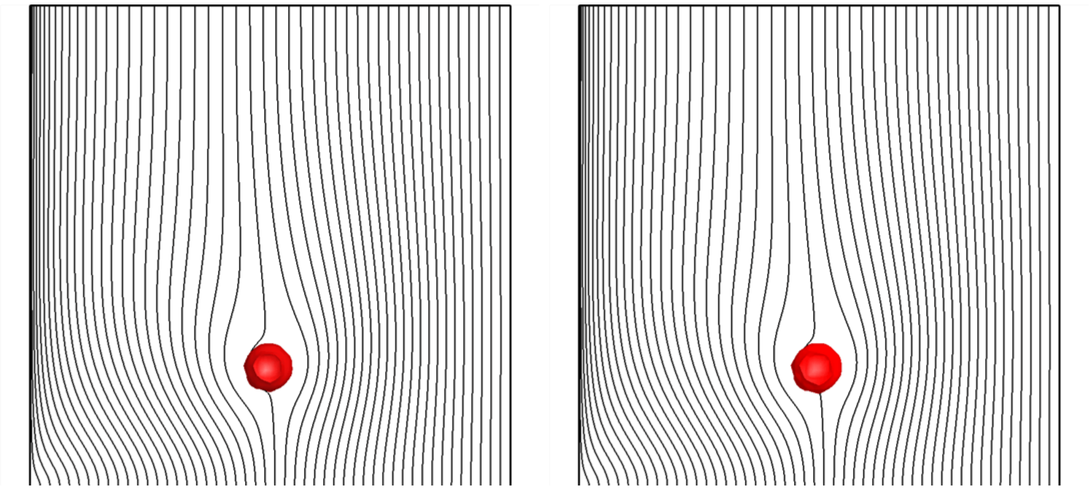

(e) Case 1-5 $\mathrm{Re_p} = 1.37$ (f) Case 1-6 $\mathrm{Re_p} = 1.37$

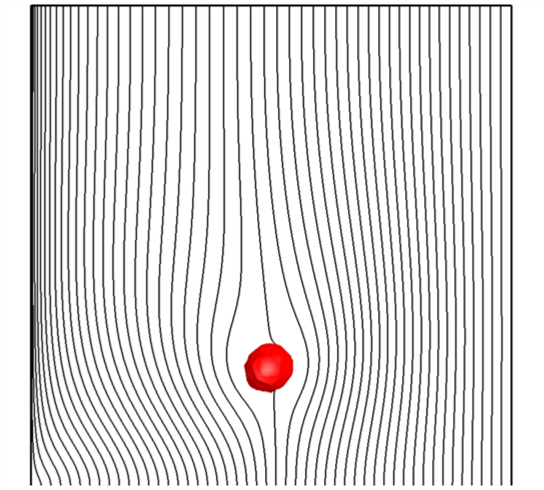

(g) Case 1-7 $\mathrm{Re_p} = 1.37$

Figure 3.5: Streamlines from bottom wall

Figure 3.6 shows the relationship between the lift coefficient and Reynolds number. The graph shows the simulated results of the cases 1-1 to 1-4 and the results by McLaughlin [27] and Kurose and Komori [15]. In case 1-1, at the low Reynolds number, $Re_\mathrm{p} \leqq 10$, the simulated value is larger than the results by McLaughlin [27] and Kurose and Komori [15]. In case 1-2, the results are slightly larger than in the case 1-1 and with the compared result. As for case 1-2, the analysis area is 5 times bigger, at the low Reynolds number, the size of analysis area should be affected the simulation results.

On the other hand, in case 1-3, where the domain size is 2 times larger, simulated result values are closer to the results by McLaughlin [27] and Kurose and Komori [15]. In addition, simulation mesh size was change to 1/20 for case 1-4, at the low Reynolds number, $Re_{\mathrm{p}} \leqq 10$, the simulated valued are larger than case 1-3. However, the simulated valued in case 1-4 become closer to the results by McLaughlin [27] than case 1-3 in the region of Reynolds number, $70 \leqq Re_{\mathrm{p}} \leqq 500$. From these results in cases 1-1 to 1-4,the lift force is considered to be affected by the analysis region of the flow direction, as well as the size of the simulation mesh size than the thickness of the analysis domain.

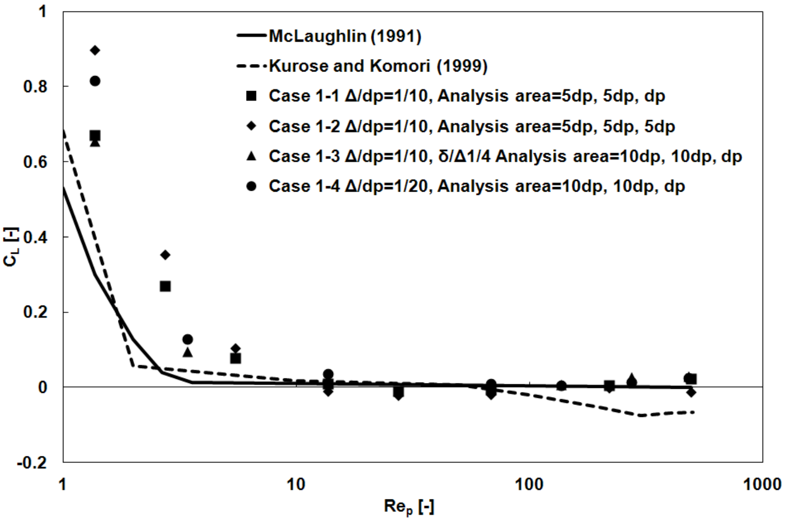

Figure 3.6: Influence of analysis domain and computational mesh sizes

Figure 3.7 shows the relationship between the lift coefficient and Reynolds number for cases 1-3, 1-5, 1-6, and 1-7. At low Reynolds number region, $1 \leqq Re_{\mathrm{p}} \leqq 15$, the simulated value in case 1-5 is larger than the results by McLaughlin [27]. In case 1-6, the simulated result is larger than case 1-5 in the same region of Re_{p}. However, at higher Reynolds number, $70 \leqq Re_{\mathrm{p}} \leqq 500$, the simulated result becomes smaller than case 1-5.

Though the simulation sub-mesh for case 1-7 is 2 times smaller than the case 1-5, almost same values can be seen over the entire region of Reynolds number. From these results, the effect of analysis region size would be more significant as the increase of simulation sub-mesh value.

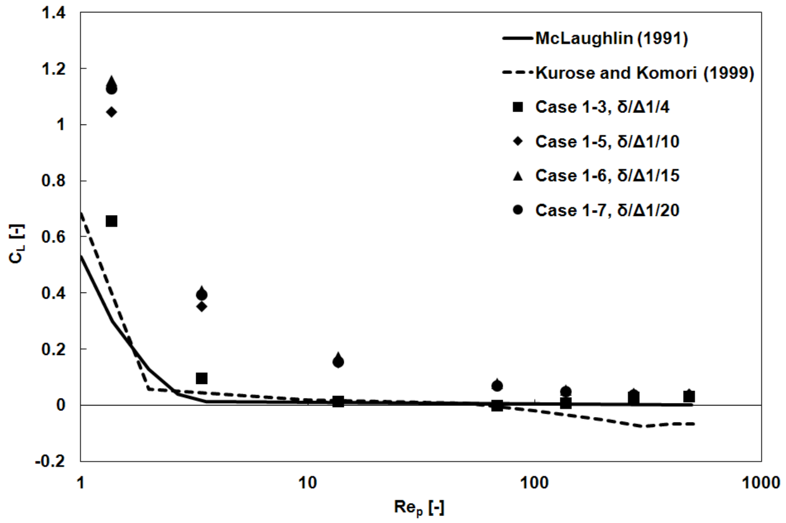

Figure 3.7: Influence of sub-mesh size on lift coefficient

3.4.2 Magnus force

The lift coefficient of Magnus force which is caused by the rotational motion by a particle was also studied. Particle rotation Reynolds number was set to $Re_{\mathrm{R}} = 0.412$. This corresponds to the rotational angular velocity of $\omega_{\mathrm{p}} = 30\mathrm{rad/s}$ when the particle diameter $d_{\mathrm{p}} = 1.0\mathrm{mm}$. This value was obtained from the DEM simulation in a fluidized bed (Kuwagi *et al.*, [28]).

Figure 3.8 shows the streamlines simulated for cases 2-1 to 2-8. The streamlines were drawn at the center of the analyses domain and the Reynolds number at $Re_{\mathrm{p}} = 5.49$ for all the cases. In cases 2-1 until 2-3, the analysis area is 5 times larger than the particle size whereas in case 2-3 until 2-8, the analysis domain area is 10 times larger than the particle size. In case 2-2, where the thickness of analysis domain is 5 times larger than the particle size, the streamlines around the particle can be seen more than in case 1-1 whereas there in not much flow differences around the particle in other cases.

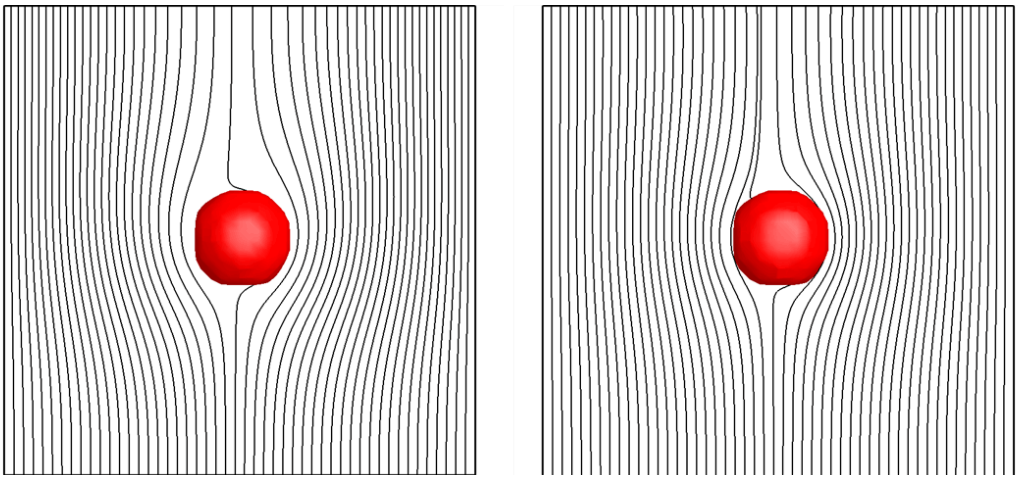

(a) Case 2-1 $\mathrm{Re}_{\mathrm{p}} = 5.49$ (b) Case 2-2 $\mathrm{Re}_{\mathrm{p}} = 5.49$

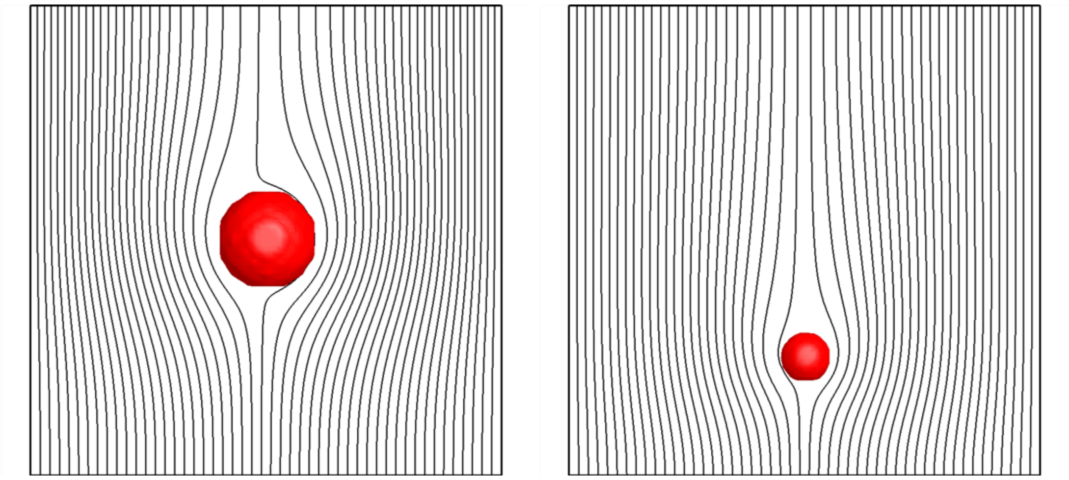

(c) Case 2-3 $\mathrm{Re_p} = 5.49$ (d) Case 2-4 $\mathrm{Re_p} = 5.49$

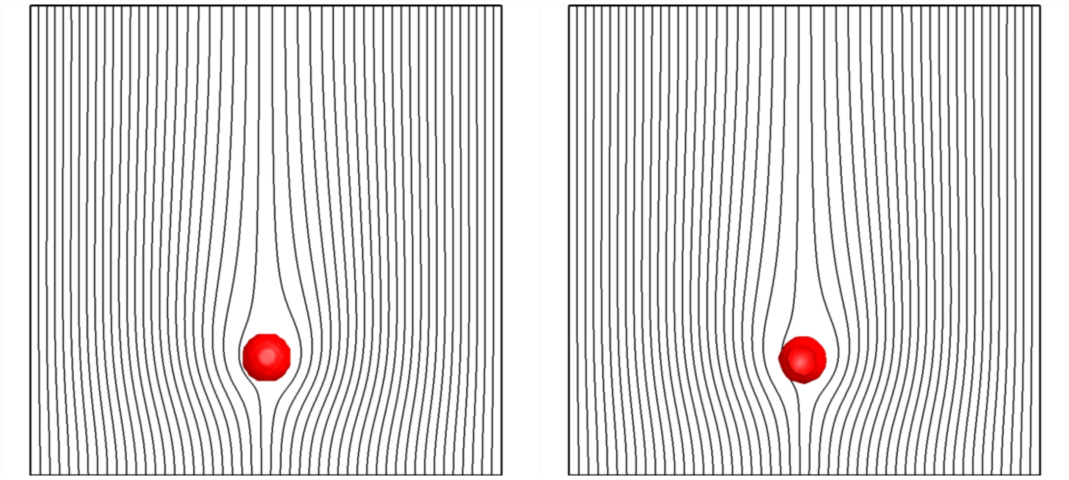

(e) Case 2-5 $\mathrm{Re_p} = 5.49$ (f) Case 2-6 $\mathrm{Re_p} = 5.49$

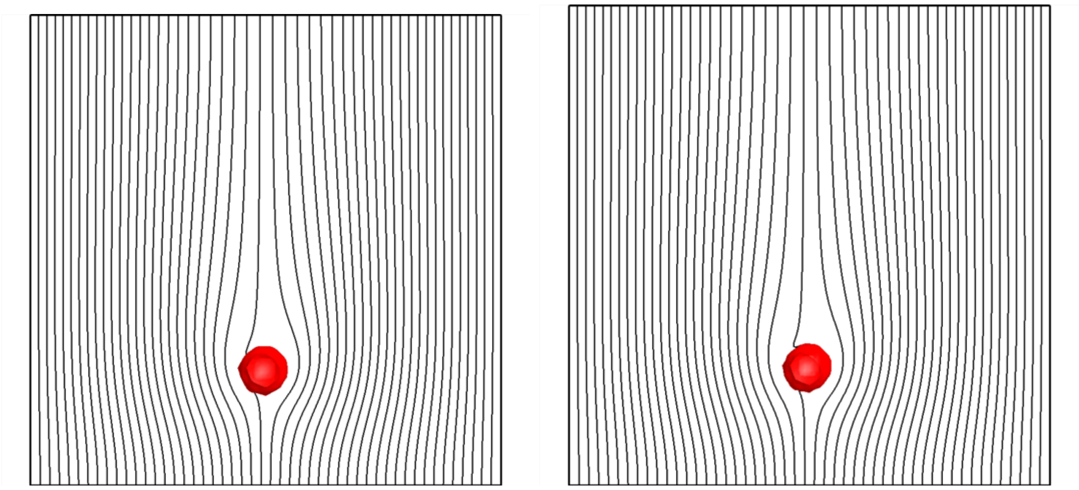

(g) Case 2-7 $\mathrm{Re_p} = 5.49$ (h) Case 2-8 $\mathrm{Re_p} = 5.49$

Figure 3.8: Streamlines flow of the simulation result for magnus force

Figure 3.9 shows the lift coefficient caused by rotational motion of particle i.e., Magnus force. The simulated results are compared with the results by Oesterle and Dinh [29]. In case 2-1, overall, a good agreement of the simulated result with the result by Oesterle and Dinh [29] can be seen. However, the tendency is different at the high Reynolds number region, $Re_\mathrm{p} > 20$. In case 2-2, the thickness is 5 times larger than case 2-1, the simulated values are smaller than case 2-1 at low Reynolds numbers. On the other hand, case 2-3, where the simulation mesh size is 2 times smaller than case 2-1, the simulated results are slightly smaller at low Reynolds number, $1 \leqq Re_\mathrm{p} \leqq 30$. On the other hand, the value becomes larger at Reynolds number, $30 \leqq Re_\mathrm{p} \leqq 100$. In case 2-4, which domain analysis area is 2 times larger than case 2-1, the simulated results are smaller. Moreover, in case 2-5, there are merely not many differences with the simulated value for case 2-4. From these results, as is the case in Saffman force, the analysis region for flow direction as well as the size of the simulation mesh size more significantly affects the result of lift force than the thickness of the analysis domain.

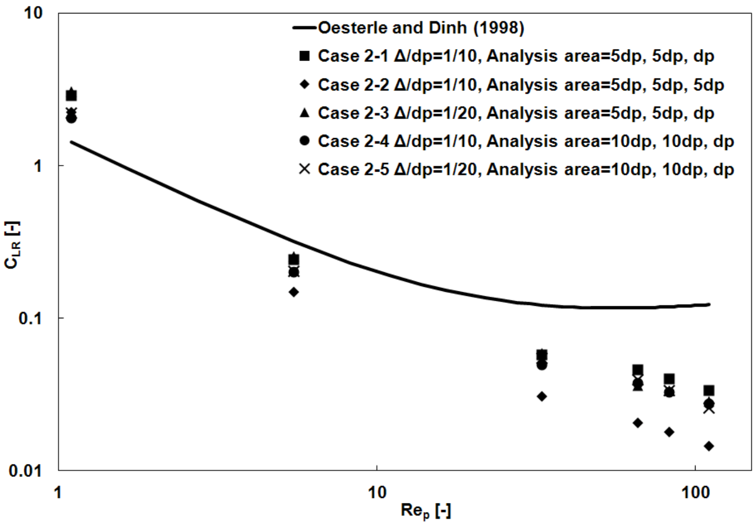

Figure 3.9: Influence of analysis domain and computational mesh sizes on lift coefficient due to rotation

Furthermore, the effect of simulation sub-mesh size to determine the volume fraction also has been examined for Magnus force. Figure 3.10 shows the simulated lift coefficients caused by rotational motion of particle and compared with the result by Oesterle and Dinh [29]. These results are for cases 2-4, 2-6, 2-7, and 2-8. The simulation sub-mesh size for case 2-6 to case 2-8 has been changed from 1/10 to 1/20.

From this figure, although the simulated results in case 2-6 are smaller than case 2-4 at low Reynolds number, the values well agrees at high Reynolds number, respectively. Moreover, the simulated values in case 2-7, are larger than case 2-6 and closer to the results by Oesterle and Dinh [29]. However, the simulated values in case 2-8 become smaller than case 2-7 as the simulation sub-mesh size becomes smaller.

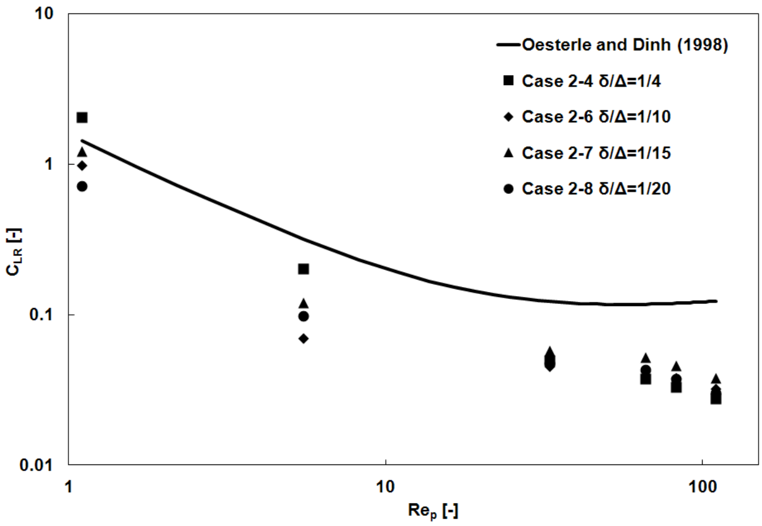

Figure 3.10: Influence of sub-mesh size on lift coefficient due to rotation

3.4.3 Viscous torque

Figure 3.11 shows the simulated streamlines of cases 3-1 to 3-5. The times of computational simulation conducted is 0.005 seconds. The streamlines were taken at particle rotation Reynolds number Re_{R} = 0.412, which corresponds to the rotational angular velocity of ω_{p} = 30rad/s. In figure 3.11, the symmetry streamlines can be seen in most of the figures.

Though the cylindrical shape of analysis region should be used in the simulations, this is contrary to the advantage that the IB method can treat an irregular shaped immersed object with rectangles computational meshes. The square-shaped analysis domain for the simulations would generate the square-shaped outer streamlines. However, the shape of streamlines is round shaped around the particle in the figures, the square shaped domain area would not significantly affect the viscous torque.

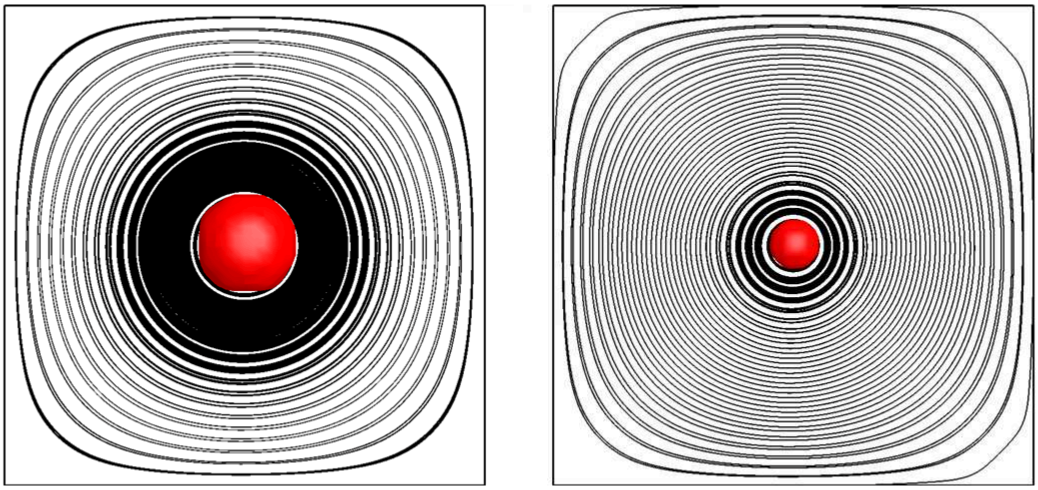

(a) Case 3-1 $\mathrm{Re_R} = 0.412$ (b) Case 3-2 $\mathrm{Re_R} = 0.412$

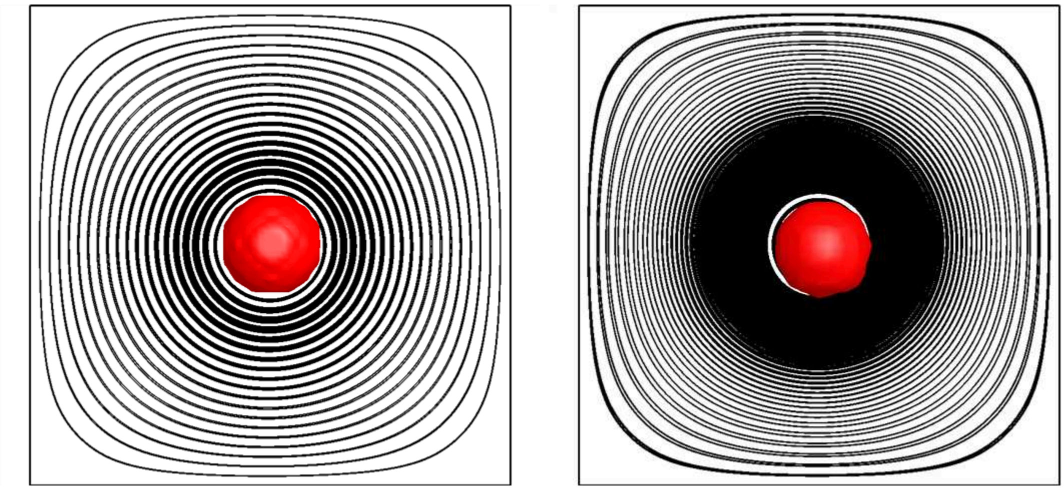

(c) Case 3-3 $\mathrm{Re_R} = 0.412$

(d) Case 3-4 $\mathrm{Re_R} = 0.412$

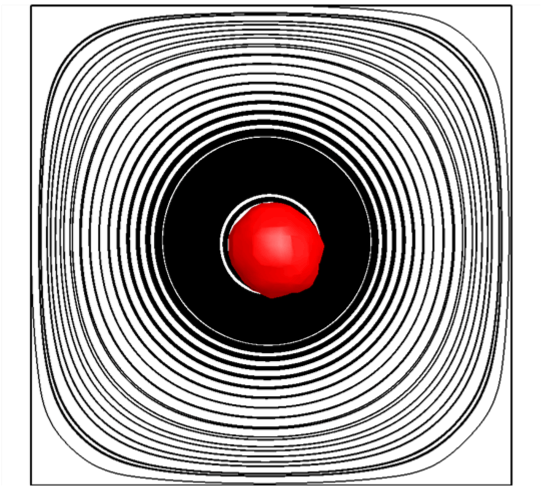

(e) Case 3-5 $\mathrm{Re_R} = 0.412$

Figure 3.11: Streamlines flow of the simulation result for viscous torque

Figure 3.12 shows the torque coefficient. The simulated results are compared with the results by Takagi [19] for cases 3-1, 3-2, and 3-3. The simulation results in case 3-1 was qualitatively same as Takagi's analytical solutions. However, the values are 50% less than results of Takagi [19]. Case 3-2 was then carried out to study the effect of flow area. However, the result became smaller than in the case 3-1. When the simulation mesh is changed to smaller size in case 3-3, the results are much larger than the case 3-1 and closer to results of Takagi [19]. Furthermore, the effect of simulation sub-mesh size to calculate the volume fraction was performed for viscous torque as shown in cases 3-4 and 3-5.

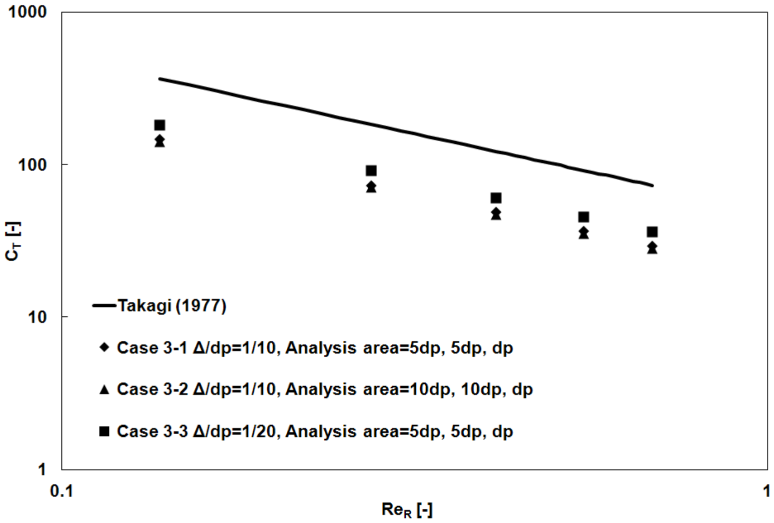

Figure 3.12: Influence of analysis domain and computational mesh sizes on viscous torque

Figure 3.13 shows the influence of sub-mesh size on the viscous torque. The results for cases 3-4 and 3-5 are compared with the result of Takagi [19] and the case 3-1. The result value in case 3-4 is smaller than in case 3-1. In addition, the values for case 3-5 also smaller than case 3-4. In the results, it would be considered that the simulation sub-mesh size gave less effect on viscous torque.

From the results in cases 3-1, 3-2, 3-4, and 3-5, the analysis region size and the simulation sub-mesh size would not give a significant effect on the viscous torque. However, the simulation mesh size in case 3-5 gave a significant effect on the viscous torque calculation. From these results, in order to calculate the viscous torque accurately in a gas-particle two-phase flow, a much finer simulation mesh system especially near particle surface would be needed.

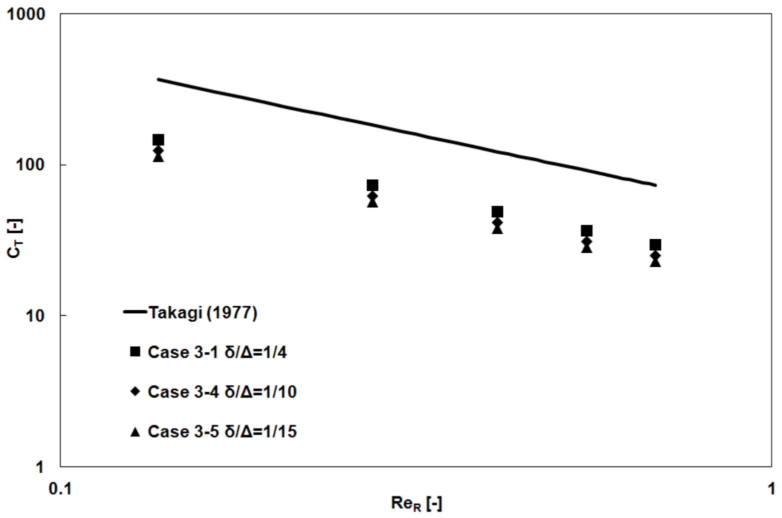

Figure 3.13: Influence of the sub-mesh size on viscous torque

3.5 Chapter conclusions

Studies on lift forces and viscous torque have been carried out in an attempt of using the body-force-type Immersed Boundary method for multiphase flow. The study has been implemented for the effect of calculation of the analysis domain size, simulation mesh size, and simulation sub-mesh size.

From the results, for the Saffman force, it can be considered that domain analysis region for flow direction, the size of the computational mesh size more significantly affect on the lift force than the thickness of analysis domain region and the simulation sub-mesh size. Furthermore, the simulation sub mesh size did not significantly affect on the analysis.

In the study of the lift force due to the particle rotation in Magnus force, the analysis region as well as the size of the simulation mesh size did not affect the results of lift force than the thickness of the analysis domain. On the other hand, simulation sub-mesh size affect at the simulated results at low Reynolds number but not significantly affect much at the high Reynolds numbers.

In the study on viscous torque, although the simulated values were 50% less than the results by Takagi [19], the simulated results qualitatively agreed. Furthermore, the influence of the analysis domain, the simulation mesh size and simulation sub-mesh size were examined. From these results, it is considered the influence of the simulation sub-mesh size gives less effect to the analysis results, a much finer simulation mesh system would be needed for the present simulation.

CHAPTER 4

EXAMINATION OF VARIOUS ESTIMATION EQUATION FOR DRAG FORCE BY USING IMMERSED BOUNDARY METHOD (IBM)

4.1 Introduction

Powder processing industry requires a method by which the mass transfer of solid materials can be handled efficiently. Since gases have a continuous phase, they can be used for the transportation of non–continuous phase materials such as solid particles. The mechanism for such transportation is usually complex. Fluidized bed is one of the systems that can control the interactions between the particles and their transporter (gas). However, because gas–solid flow involves complex phenomena, numerical approaches are being employed as a feasible way of obtaining useful analysis data.

As a numerical approach, the discrete element method (DEM) is used to investigate the hydrodynamic behavior of gas–solid interactions in a fluidized bed. However, in spite of the fact that DEM can be applied to problem pertaining to cohesion, heat transfer and chemical reaction, it is impossible to use DEM for dealing with phenomena whose scale is smaller than the particle size, such as the effect of drag, lubrication, and lift forces. Thus, some constitution equations to account for such phenomena must be included in a DEM simulation. The accuracy of such constitution equations often has a significant effect on the final results. Accordingly, the accuracy of a constitution equation included in a DEM simulation should be confirmed from the viewpoint of process intensification in the powder industry. For example, the authors have carried out numerical simulations on a fluidized bed and compared the results obtained using a DEM simulation with those obtained using a direct numerical simulation (DNS) which does not require any constitution equations to account for the particle–fluid interaction force, including the drag force (Kuwagi *et al.*, [14]). From the results obtained using a DNS, some differences between these results and those obtained using a DEM simulation, e.g., activity of particles, were observed. This would have been partially caused by the estimation of the drag force by using a DEM simulation.

For drag force calculation, the Wen and Yu [30] equation is often used when particles are dilute, while the Ergun [31] equation is adopted when particles are dense. In a DEM simulation, these two equations are used interchangeably. However, there often exists a discontinuity between the two equations. Di Felice [32] derived a drag equation that can be applied to systems ranging from densely packed to extremely dilute. Koch and Hill [33] proposed a drag relation that was based on the lattice Boltzmann simulations. They also investigated the effect of particle arrays on the drag force acting on particles (Hill *et al.*, [33], [34]). Recently, Cello *et al.* [35] have derived a new semi–empirical model for the drag force.

In the chapter, the IBM, which is a DNS, was used to study the drag force acting on both dilute and dense particles. In order to examine the effect of particle arrays and the relationship between the drag force and flow in a simple manner, particles were arranged in a two–dimensional pattern. Since the thickness of an analysis domain corresponds to the particle diameter, the analysis domain is a monolayer of particles. Here, it should be noted that for analyzing the gas phase, a three–dimensional simulation was employed. The simulation results were compared with the results estimated using the Wen and Yu [30], [31], and Cello *et al.* [35] equations.

4.2 Numerical Analyses

The equations for mass and momentum conservations for the gas and particle phase in IBM was explained in the previous chapter 3.

4.2.1 Drag force models

When particles are dilute, the Wen and Yu [30] equation shown below is often used.

$$F_{\mathrm{D}} = \beta(v_{\mathrm{p}} - u) \tag{4.1}$$

$$\beta = \frac{3}{4} C_{\mathrm{D}} \frac{\mu(1-\varepsilon)}{d_{\mathrm{p}}^2} \varepsilon^{-2.7} Re_{\mathrm{p}\varepsilon} \tag{4.2}$$

where $Re_{\mathrm{p}\varepsilon}$ is the particle Reynolds number with voidage defined as follows:

$$Re_{\mathrm{p}\varepsilon} = \frac{u \rho_{\mathrm{f}} \varepsilon d_{\mathrm{p}}}{\mu} \tag{4.3}$$

C_{D} is the drag coefficient for a single particle and can be calculated using the Schiller and Naumann [36] equation for low Reynolds numbers ($Re_{\mathrm{p}\varepsilon} < 1000$), as shown below:

$$C_{\mathrm{D}} = \left\{ \begin{array}{ll} \frac{24(1+0.15 Re_{\mathrm{p}\varepsilon}^{0.687})}{Re_{\mathrm{p}\varepsilon}} & Re_{\mathrm{p}\varepsilon} \leq 1000 \\ 0.43 & Re_{\mathrm{p}\varepsilon} > 1000 \end{array} \right\} \tag{4.4}$$

On the other hand, the drag force acting on dense particles is calculated using the Ergun [31] equation. The drag force per unit volume is expressed as follows:

$$f_{\mathrm{D}} = 150\frac{(1-\varepsilon)^2}{\varepsilon^3}\frac{\mu(v_{\mathrm{p}}-u)}{d_{\mathrm{p}}^2} + 1.75\frac{(1-\varepsilon)}{\varepsilon^3}\frac{\rho_{\mathrm{f}}(v_{\mathrm{p}}-u)^2}{d_{\mathrm{p}}} \tag{4.5}$$

The drag force acting on a particle can be expressed as follows:

$$F_{\mathrm{D}} = \frac{f_{\mathrm{D}}V_{\mathrm{p}}}{1-\varepsilon} \tag{4.6}$$

where V_{p} is the particle volume.

In a general DEM simulation, the above two equations of drag force are often used by switching between them at certain values of voidage, e.g., $\varepsilon = 0.8$. On the other hand, Cello *et al.* [35] derived the following drag model, which cover the entire range.

$$f = K_1 + K_2\varepsilon^4 + K_3(1-\varepsilon^4) \tag{4.7}$$

where the dimensionless drag force f is defined as follows:

$$f \equiv \frac{F_{\mathrm{D}}}{F_{\mathrm{D,stokes}}} \tag{4.8}$$

$F_{\mathrm{D,stokes}}$ is the drag force in the Stokes flow.

$$\begin{aligned} K_0 &= \frac{1-\varepsilon}{1+3\varepsilon}, K_1 = \frac{1+128K_0+715K_0^2}{\varepsilon^2(1+49.5K_0)}, \\ K_2 &= \frac{1+0.130Re_{\mathrm{p}}+6.66\times10^{-4}Re_{\mathrm{p}}^2}{1+3.42\times10^{-2}Re_{\mathrm{p}}+6.92\times10^{-6}Re_{\mathrm{p}}^2}-1, \\ K_3 &= \left(\frac{2Re_{\mathrm{p}}^2}{1+Re_{\mathrm{p}}}\right)\left(\frac{-410\varepsilon+9.20\times10^{7}Re_{\mathrm{p}}K_0^{20}}{6600\varepsilon+4.92\times10^{-4}Re_{\mathrm{p}}}\right) \\ &\left(\frac{+1900\varepsilon^2-6.60\times10^{-2}Re_{\mathrm{p}}}{-4.3\times10^4\varepsilon^2-1.31\times10^{-4}Re_{\mathrm{p}}^2+7.38\times10^4\varepsilon^3}\right) \end{aligned} \tag{4.9}$$

where Re_{p} is the particle Reynolds number without voidage and is defined as follows:

$$Re_{\mathrm{p}} = \frac{u\rho_{\mathrm{f}}d_{\mathrm{p}}}{\mu} \tag{4.10}$$

Finally, the drag coefficient for multiple particles is calculated by substituting F_{D} from equation (4.1), (4.6), or (4.8) into the following equation:

$$\overline{C_{\mathrm{D}}} = \frac{F_{\mathrm{D}}}{\left(\frac{\pi d_{\mathrm{p}}^2}{4}\right)\frac{\rho_{\mathrm{f}}(v_{\mathrm{p}}-u)^2}{2}} \tag{4.11}$$

4.2.2 Analysis conditions

The schematic of the problem is shown in Figure 4.1. Since the analysis domain is a monolayer of particles, the particles are arranged two dimensionally. This arrangement is selected to easily examine the effect of particle arrangement and the relationship between the drag force and flow behavior.

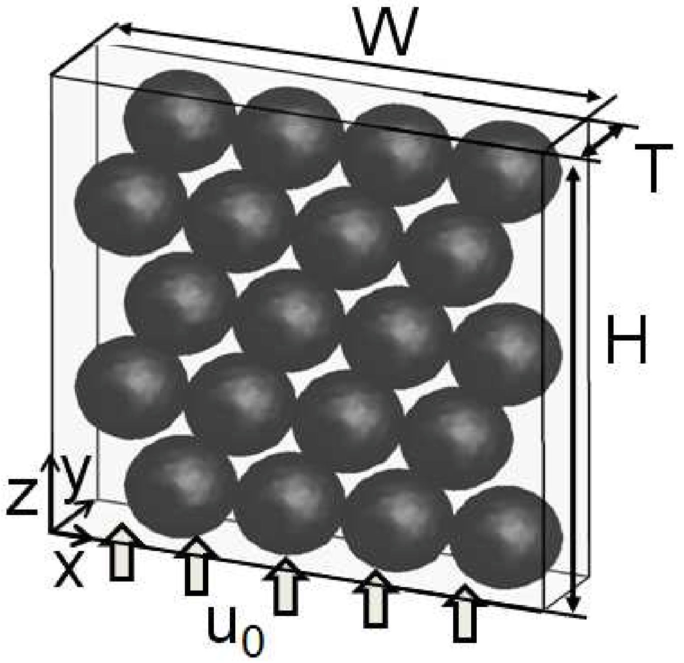

Figure 4.1: Schematic of the problem for drag force

On the other hand, the calculations for the gas phase were performed using the three–dimensional Navier–Stokes (NS) equation to precisely investigate the flow between particles. The gas is assumed to be uniformly injected through the bottom plane. From the simulation results, the force acting on each particle is obtained. In the present study, the average force was calculated.

The analysis conditions are listed in Table 4.1. The width and height of the analysis region are five times the particle diameter. This size was chosen to approximately match the size of a computational mesh used in a standard DEM simulation.

Table 4.1: Simulation conditions for drag force

Particle diameter $[m]$	1.0×10^{-3}
Particle density $[kg/m^3]$	2.65×10^3
Particle number	1, 5, 9, 12, 16, 25
Voidage [-]	0.476, 0.665, 0.707, 0.812, 0.895, 0.979
Gas density $[kg/m^3]$	1.20
Gas viscosity $[Pas]$	1.86×10^{-5}
Particle Reynolds number Re_p [-]	0.1, 0.5, 1, 5, 10, 50, 100, 300
Computational grid size $[m]$	Case 1, 2, 4, 5, 6, 7, and 9 : $\Delta x = \Delta y = \Delta z = 5.0 \times 10^{-5}$, Case 3 : $\Delta x = \Delta z = 4.01 \times 10^{-5}$, $\Delta y = 5.0 \times 10^{-5}$ Case 8 : $\Delta x = 4.31 \times 10^{-5}$, $\Delta z = 4.97 \times 10^{-5}$, $\Delta y = 5.0 \times 10^{-5}$
Column witdh and height $[m]$	Case 1, 2, 4, 5, 6, 7, and 9 : $5.0 \times 10^{-3}, 5.0 \times 10^{-3}$, Case 3 : $4.01 \times 10^{-3}, 4.01 \times 10^{-3}$ Case 8 : $4.31 \times 10^{-3}, 4.97 \times 10^{-3}$
Column thickness $[m]$	1.0×10^{-3}

Thus, it can be said that the flow in a computational mesh in a two–dimensional DEM simulation was directly solved, except for the boundary conditions. The numbers of particles are 1, 5, 9, 12, 16, and 25. The arrangements of particles are shown in Figure 4.2. The particles are considered to be fixed at their positions.

Hill *et al.* [33], [34] investigated the effect of the drag force on flows in simple cubic, face-centered cubic, and random arrays of particles by using the lattice Boltzmann simulations. In the present study, the inline and staggered arrangements, which are extreme cases of the particles are considered.

The values of the corresponding voidage (void fraction) for the above–mentioned numbers of particles are 0.476, 0.665, 0.707, 0.812, 0.895, and 0.979, respectively. The computational grid size Δ was set to be $\Delta/d_\mathrm{p} = 1/20$. This is because the difference between the values of C_D when the values of Δ/d_p were 1/10 and 1/30 was about 15% while this difference when the values of Δ/d_p were 1/20 and 1/30 was about 4%.

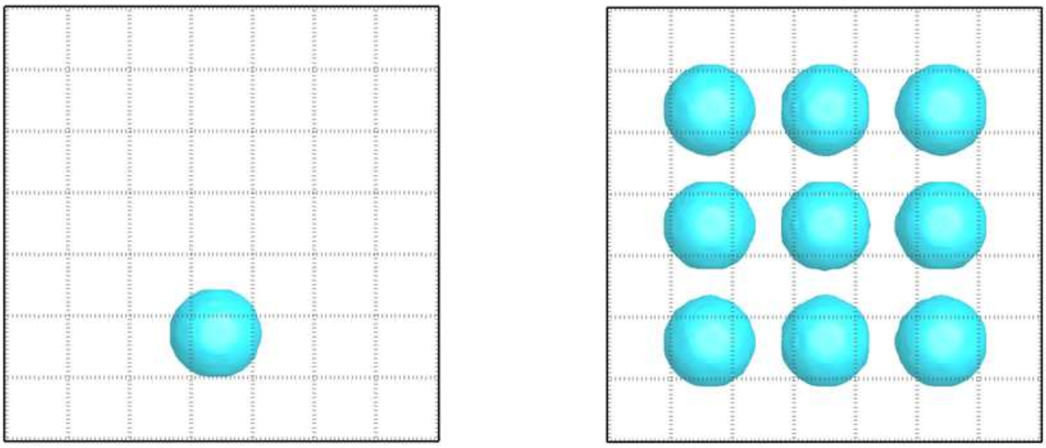

(a) Case 1 ($\varepsilon = 0.979$)

(b) Case 2 ($\varepsilon = 0.707$)

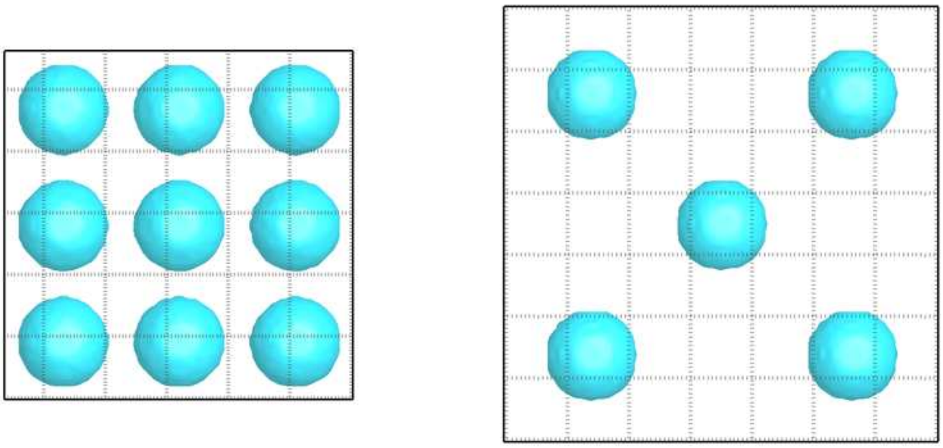

(c) Case 3 ($\varepsilon = 0.707$)

(d) Case 4 ($\varepsilon = 0.895$)

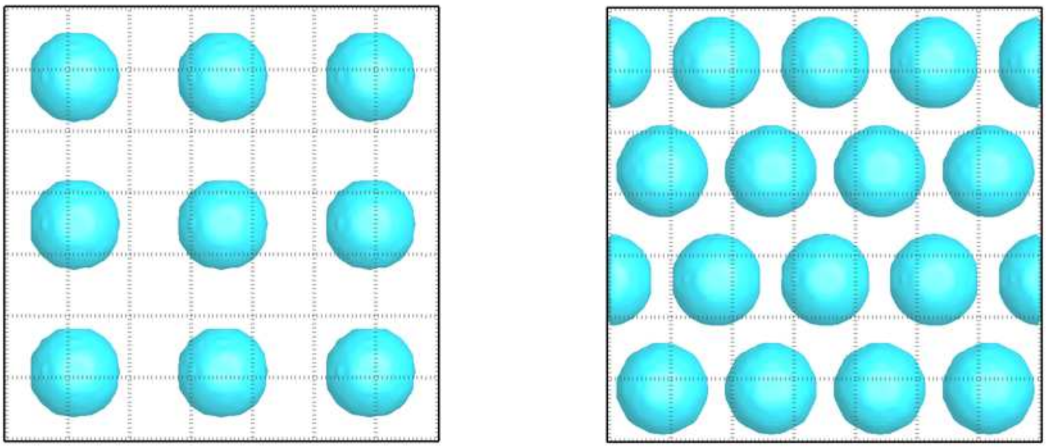

(e) Case 5 ($\varepsilon = 0.812$)

(f) Case 6 ($\varepsilon = 0.665$)

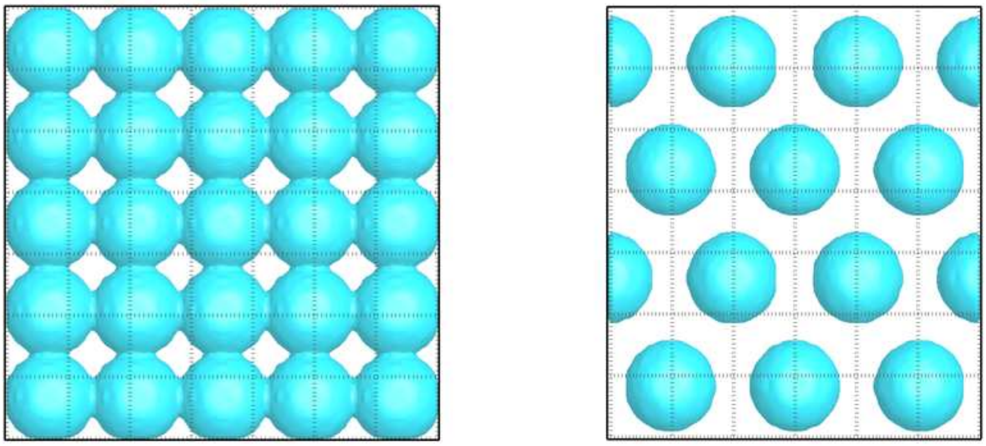

(g) Case 7 ($\varepsilon = 0.476$)

(h) Case 8 ($\varepsilon = 0.707$)

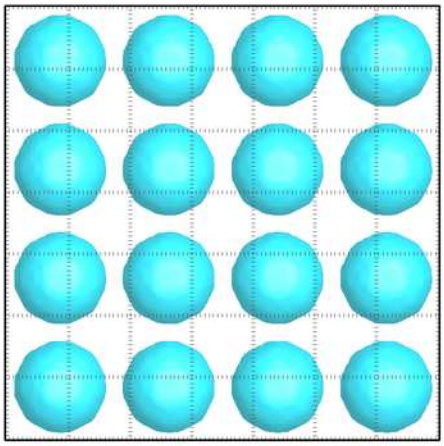

(i) Case 9 ($\varepsilon = 0.665$)

Figure 4.2: Particle arrangement

4.2.3 Numerical procedure

Time discretization was approximated using an explicit method and inertial terms corresponding to the third–order upwind scheme for the N–S equations. The pressure field was solved using the HS–MAC (SOLA) method. The boundary conditions for the numerical simulation are shown as follows:

$$u_x = 0, \frac{\partial u_y}{\partial x} = \frac{\partial u_z}{\partial x} = 0 \text{ (planes of } x = 0 \text{ and } W \text{)} \tag{4.12}$$

$$u_y = 0, \frac{\partial u_x}{\partial y} = \frac{\partial u_z}{\partial y} = 0 \text{ (planes of } y = 0 \text{ and } T \text{)} \tag{4.13}$$

$$u_x = u_y = 0, u_z = u_0 \text{ at } z = 0 \text{ (at the plane of } z = 0 \text{)} \tag{4.14}$$

$$\frac{\partial u_x}{\partial z} = \frac{\partial u_y}{\partial z} = \frac{\partial u_z}{\partial z} = 0 \text{ at } z = H \text{ (at the plane of } z = H \text{)} \tag{4.15}$$

Equation (4.13) is valid because the effect of particle arrangement on the calculation of the drag force was examined by assuming the arrangement to be two–dimensional. The slip condition was assumed for the side planes, as indicated by equation (4.12). As described previously, the analysis domain appears equivalent to one computational mesh in a DEM simulation.

However, the actual boundary conditions for a computational mesh in a DEM simulation of a fluidized bed are variable and complex. The main purpose of this study is to present the most precise discussion on the accuracy of some estimation equations for the drag force by considering a simple problem. Accordingly, we assumed a one–dimensional upward flow and the slip condition at the boundary.

4.3 Results and Discussion for chapter 4

4.3.1 Drag force on a single particle

In order to confirm the accuracy of the simulation used in this study, the simulation results were compared with the results estimated using the Schiller and Naumann (Schiller and Naumann, [36]) and White (White, [37]) equations. Furthermore, the effect of the monolayer of particles on the drag force was examined by comparing the simulation results obtained in this study with the results obtained using fully three–dimensional simulations.

Figure 4.3 shows the results in terms of the drag coefficient. The thickness of the analysis domain for the fully three–dimensional simulations, is given by $T = 5d_\mathrm{p}$ $(= W = H)$. The difference between the thickness of the particle monolayer and that of the fully three–dimensional domain was within 8%, except at high Reynolds numbers ($Re_\mathrm{p} > 100$).

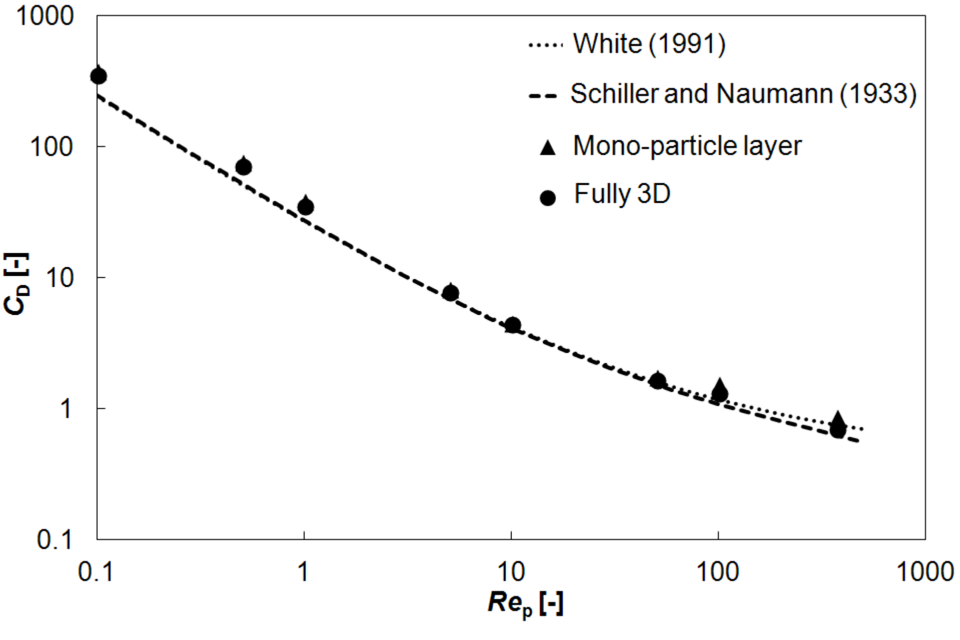

Figure 4.3: Drag coefficient for a single particle

When the Reynolds number was greater than 5, the simulation results agreed well with the estimation results. On the other hand, the difference between these results was over

50% at low Reynolds numbers. This difference would have been caused by the effect of the analysis area.

Since the viscosity is dominant when the Reynolds number is low, the effect of viscosity spreads widely.

Thus, a small analysis area would not be sufficient. However, a good overall agreement was obtained between the simulation and estimation results.

4.3.2 Effect of domain on voidage definition

Though some definitions are available for voidage, in the present study, particles were arranged in an orderly manner. In such a case, voidage can be defined on the basis of the type of particle arrangement. However, this voidage is different from the total voidage in the analysis region when particles are concentrated and a large space exists around the particles, as in case 2 shown in Figure 4.2.

Figure 4.4 shows the simulation results for cases 2 and 3. The results for case 3 (inline particle arrangement) agreed well with the estimation results for a voidage (ε) of 0.707, which is defined according to the type of particle arrangement.

On the other hand, the results for case 2 were not in good agreement with the estimation results. However, they agreed well at $\varepsilon = 0.812$, which is defined for the total voidage in the analysis region.

Since the slip condition was assumed in this simulation, the non–agreement between the results can be regarded to be due to the repetition of the analysis domain. In such a case, the total voidage corresponds to the voidage defined for one analysis region.

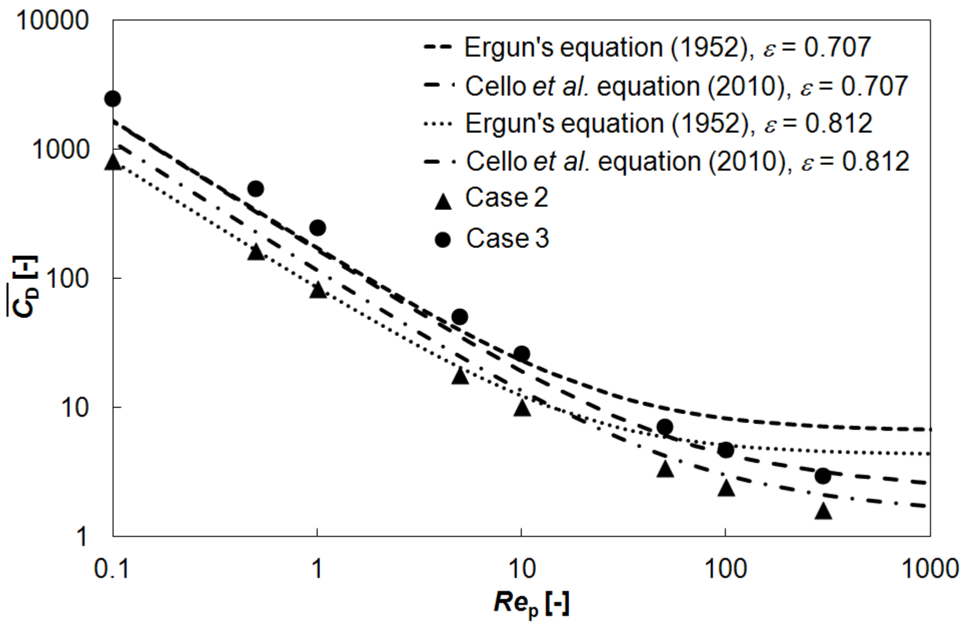

Figure 4.4: Effect of voidage definition on drag force

4.3.3 Drag force on dilute particles

Figure 4.5 shows the comparison between the drag force simulated using the IB method and that estimated using the Wen and Yu [30] and Cello *et al.* [35] equations. The voidage values for the above two cases are 0.895 and 0.812, respectively.

In both cases (a) and (b), the simulation results were larger than the results estimated using the Wen and Yu [30] equation. On the other hand, the simulation results agreed well with those estimated using the Cello *et al.* [35] equation.

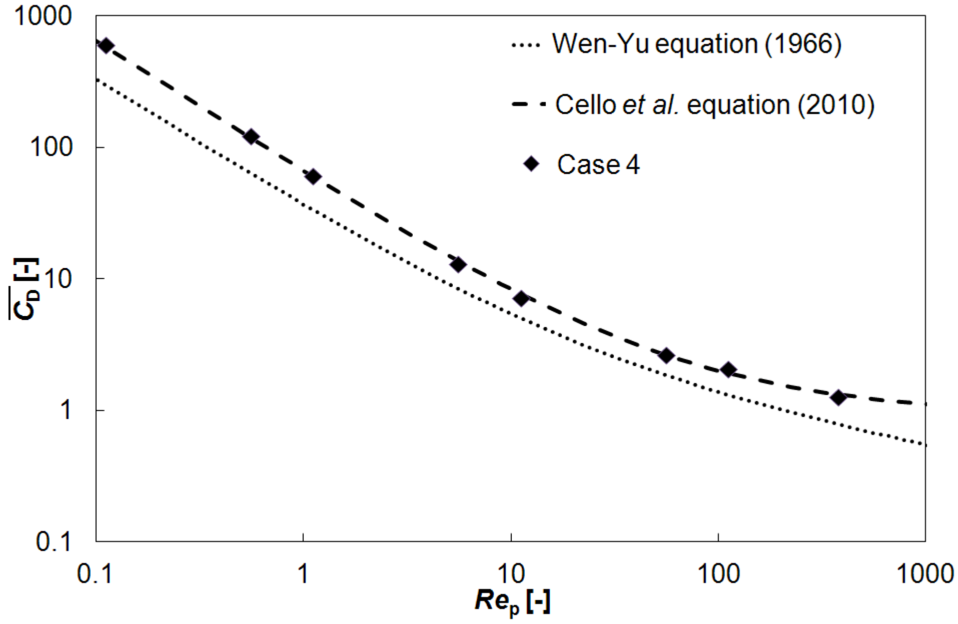

(a) Case 4 ($\varepsilon = 0.895$)

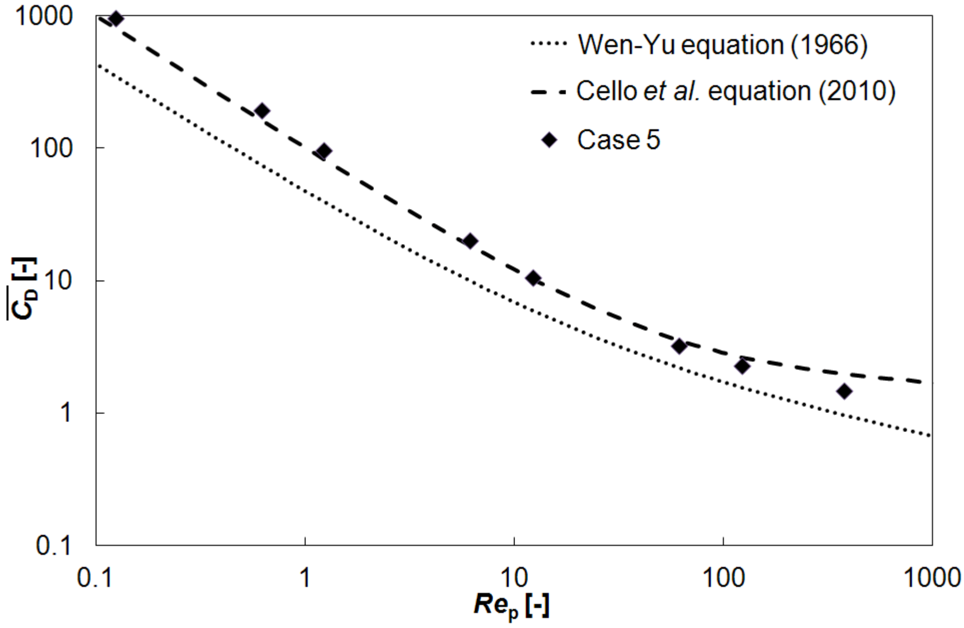

(b) Case 5 ($\varepsilon = 0.812$)

Figure 4.5: Drag coefficient for dilute particles

4.3.4 Drag force on dense particles

Figure 4.6 shows the results for the drag force on dense particles. The drag coefficients obtained using the simulation are compared with those estimated using the Ergun [31] and the Cello *et al.* [35] equation. In case 6 for a stagggered particle arrangement, the simulation results are close to the results estimated using the Ergun equation.

On the other hand, in case 7, the simulation results are close to the results estimated using the Ergun equation at low Reynolds numbers ($Re_\mathrm{p} < 10$), and at high Reynolds numbers ($Re_\mathrm{p} > 10$), the simulation results obtained using the IBM approach the results calculated using the Cello *et al.* [35] equation.

The Reynolds number for a fluidized bed under the conditions applied in our previous simulations (Kuwagi *et al.*, [38] [39]) is around 100. In these simulations, the particles' movement simulated using the DEM was more active than that simulated using the IBM. From the results obtained in this study, the drag force calculated using the Ergun equation for Re_p values around 100 is about two times that calculated using the IBM, except for case 6.

However, the difference between the drag coefficients in cases 6 and 7 was observed at high Reynolds numbers ($Re_\mathrm{p} > 50$). Therefore, the effect of particle arrangement will be examined below.

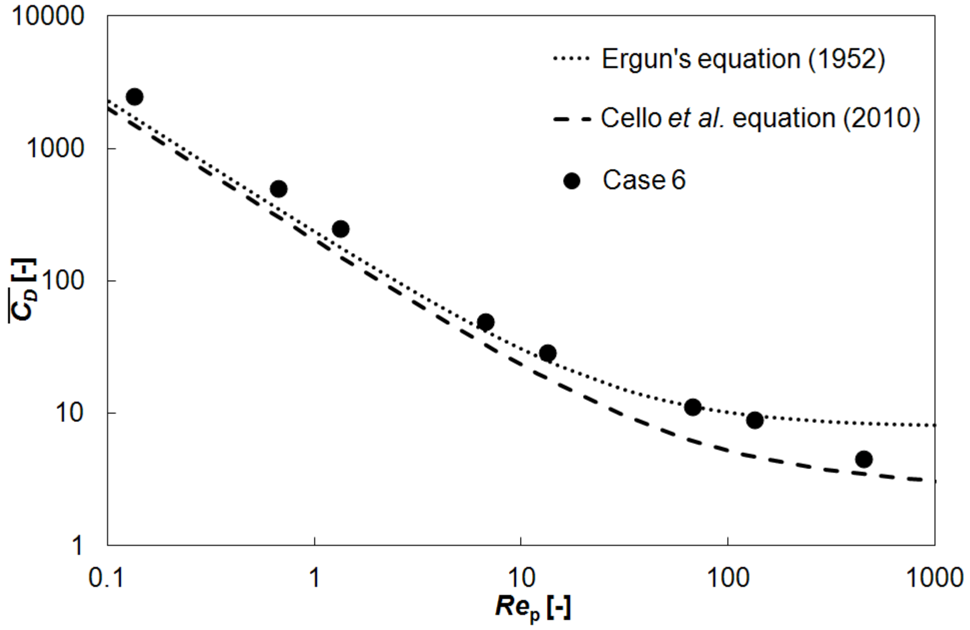

(a) Case 6 ($\varepsilon = 0.665$)

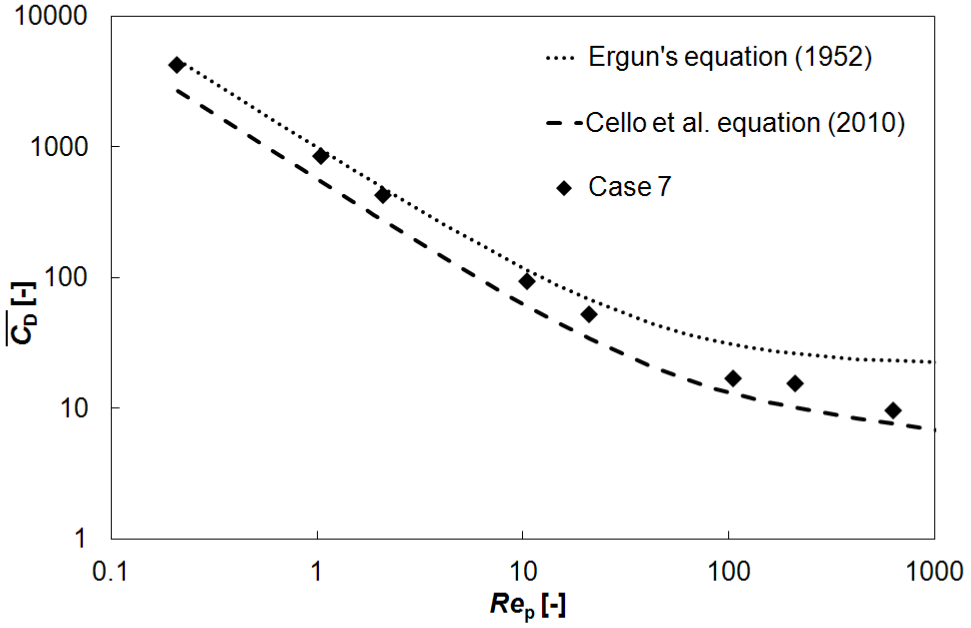

(b) Case 7 ($\varepsilon = 0.476$)

Figure 4.6: Drag coefficient for dense particles

4.3.5 Effect of particle arrangement

Figure 4.7 shows the simulation results for two types of particle arrangement: cases 3 (inline) and 8 (staggered) for which $\varepsilon = 0.707$, and cases 6 (staggered) and 9 (inline) for which $\varepsilon = 0.665$. The simulation results are compared with the results estimated using two equation, i.e., the Ergun (Ergun, [31]), and Cello (Cello *et al.,* [35]) equations. A significant difference cannot be observed in both figures at low Reynolds numbers ($Re_{\mathrm{p}} < 10$).

On the other hand, at high Reynolds numbers ($Re_{\mathrm{p}} > 50$), the effect of particle arrangement or particle structure becomes larger as the Reynolds number increases. The present analysis domain is a monolayer of particle, and the slip condition is assumed for side walls. This situation corresponds to the analysis domain being repeated in the y–direction. Accordingly, the particle arrangement in the present system is supposed to be inline in the y–direction.

Since the effect of a three–dimensional flow would be small for this particle arrangement, the present simulations on a monoplayer of particle would provide valid data when $Re_{\mathrm{p}} < 50$.

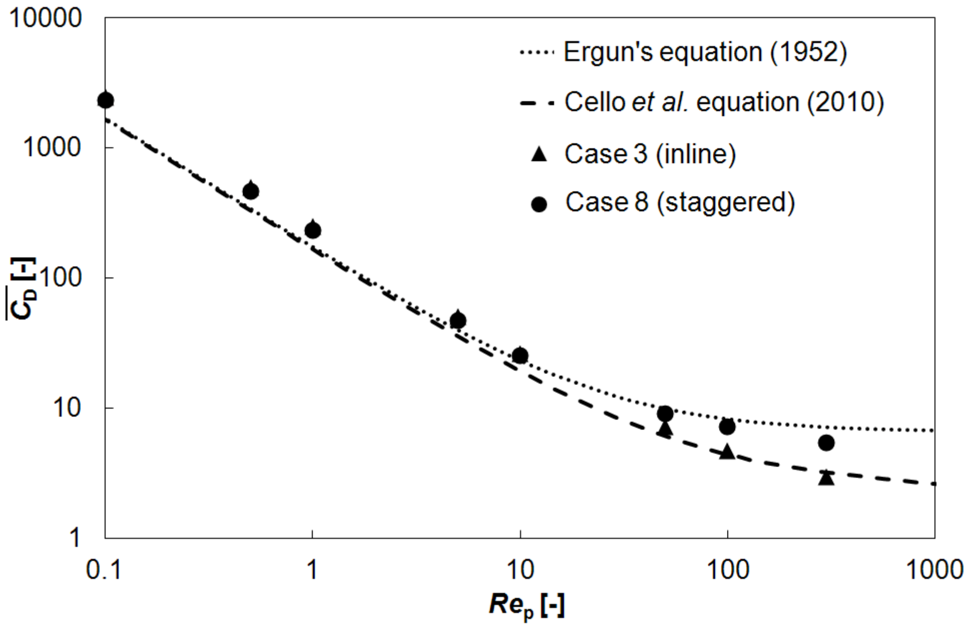

(a) Cases 3 and 8 ($\varepsilon = 0.707$)

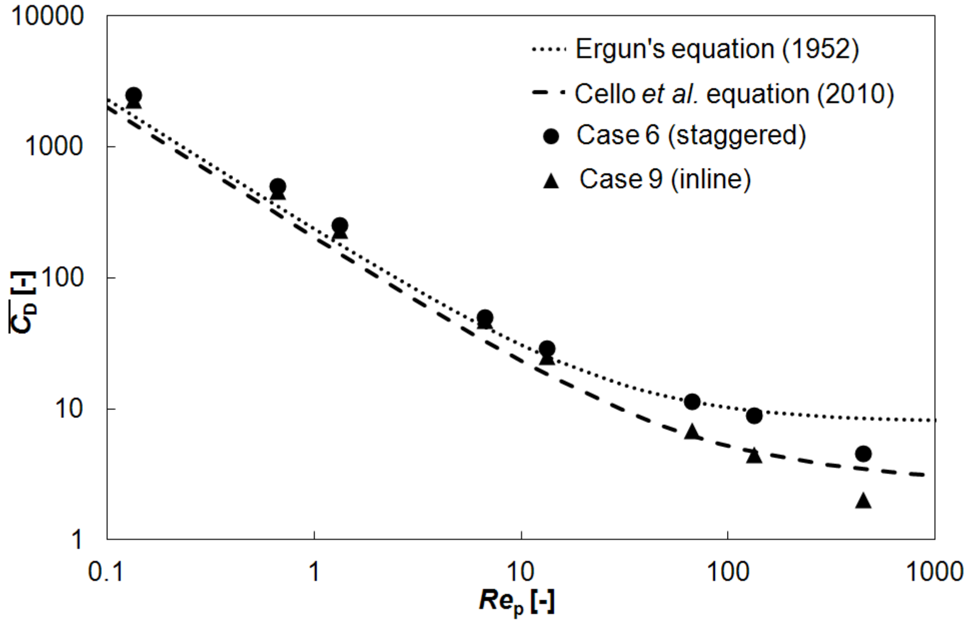

(b) Cases 6 and 9 ($\varepsilon = 0.665$)

Figure 4.7: Effect of particle arrangement on drag force

Figure 4.8 shows the stream lines passing through the bottom wall for cases 6 and 9 at $Re_{\mathrm{p}} = 13.3$ and $Re_{\mathrm{p}} = 133$. Although the flow is regular at $Re_{\mathrm{p}} = 13.3$, some wake vortices can be observed at $Re_{\mathrm{p}} = 133$ for both cases 6 and 9. The vortex formation in the wake would affect the average drag force since the vortex structure at $Re_{\mathrm{p}} = 133$ appears three–dimensional. Thus, three–dimensional analyses would be required to examine the effect of particle arrangement on the drag force.

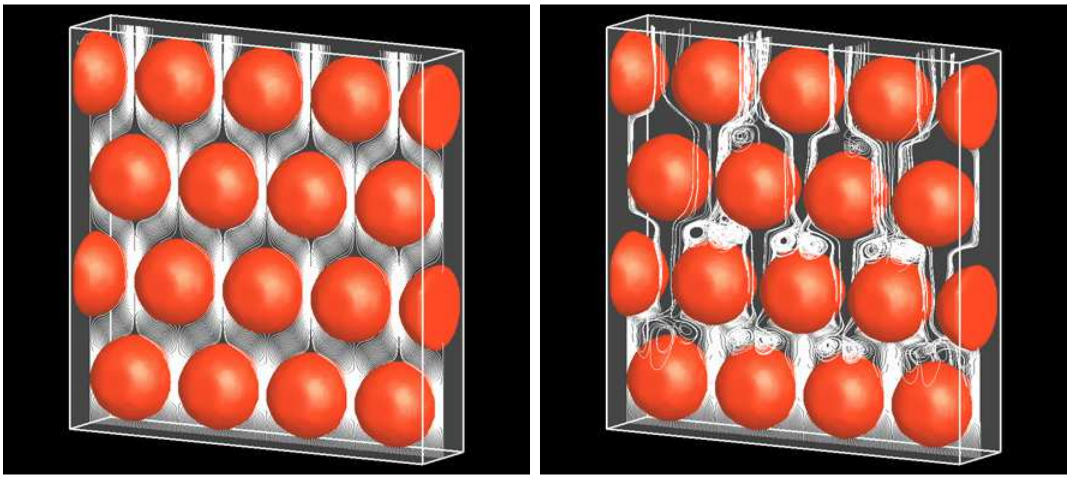

(a) Case 6 ($Re_{\mathrm{p}} = 13.3$) (b) Case 6 (Re_{p} =133)

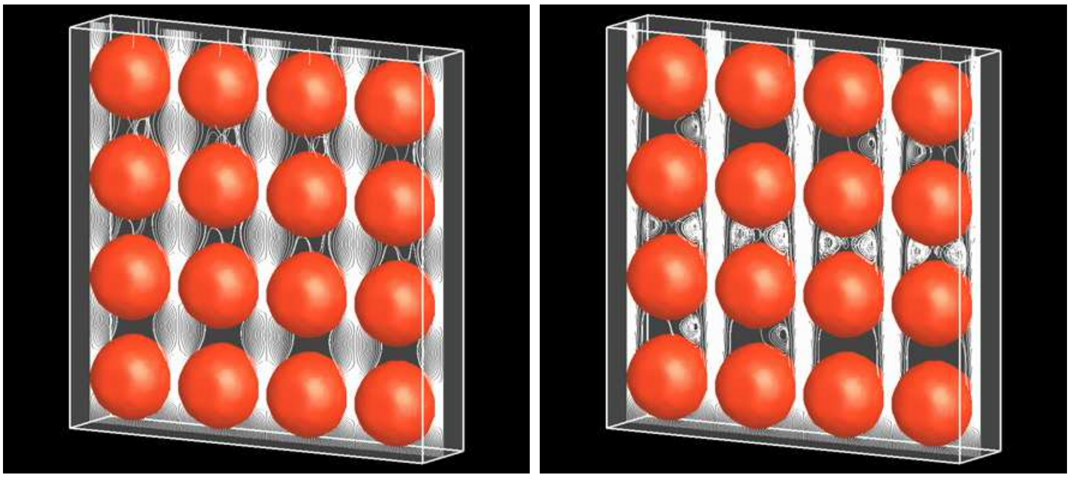

(c) Case 9 ($Re_{\mathrm{p}} = 13.3$) (d) Case 9 ($Re_{\mathrm{p}} = 133$)

Figure 4.8: Stream lines passing through bottom wall

4.4 Chapter conclusions

A numerical study of drag force acting on densely packed and dilute particles is presented. This study is performed using the IBM. In order to confirm the accuracy of the simulation code used in this study, the drag force on a single particle was simulated. The simulation results were compared with the results estimated using the Schiller and Naumann (Schiller and Naumann, [36]) and White (White, [37]) equations. Except at low Reynolds numbers, the simulation results agreed well with the estimation results.

In the cases of dilute–particle arrangements, the simulated drag coefficient agreed well with that estimated using the Cello *et al.* [35] equation. On the other hand, the drag coefficient for dense particles simulated using the IBM approached the values estimated using the Ergun (Ergun, [31]) equation in the case of staggered particle arrangement, whereas in the case of inline particle arrangement, the simulated drag coefficient approached the values estimated using the Cello *et al.* [35] equation as the Reynolds number increased.

The effect of particle arrangement at same voidage was also confirmed. From the simulation results, it was found that particle arrangement did not significantly affect the drag force when $Re_{\mathrm{p}} < 10$. On the other hand, the effect of particle arrangement increased as Re_{p} increased.

Since some vortices were observed at $Re_{\mathrm{p}} = 133$, the structure of these vortices would affect the average drag force. In order to examine the effect of particle arrangement on the drag force at high Reynolds numbers, fully three–dimensional analyses would be required.

CHAPTER 5

MODELING OF THERMAL RESISTANCE MODEL FOR TWO CONTACTING PARTICLES

5.1 Introduction

In recent years, Discrete Element Method (DEM) has been widely used for the heat transfer problems and trouble analyses along with the development of the fluidized bed engineering. The DEM is becoming a widely accepted tool to analyze various granular flows and powder processes. The DEM is also possible to deal with problems in various scales in a fluidized bed.

After Rong and Horio [40] obtained remarkable results for a numerical simulation of a fluidized bed combustor by the DEM, a lot of experiments and new results have been conducted such as (Bodhisattwa et al., [41]. Morikawa et al. [42] also used the DEM to analyze the heat and flow in a fluidized bed combustor. They obtained a good qualitative agreement of the heat transfer coefficient between the bed and the heat transfer tube. However, the equation to estimate contact heat transfer between colliding particles has not been validated sufficiently.

In order to analyze the heat transfer in a fluidized bed using the DEM, we need to know (1) the particle-particle contact heat transfer, (2) the particle-gas heat transfer and (3) the particle-wall surface heat transfer. For (2), Ranz and Marshall [43] equation is often used. On the other hand, for (1) and (3), Rong and Horio [40] assumed a gas membrane between contact planes and calculated with the heat conduction equation, i.e. Fourier‘s law. However, the actual contact area i.e. the particle surface has surface roughness. Accordingly, the major problem in modeling the contact heat transfer model is how to consider the surface roughness on surface of particle.

For the contact heat transfer between particles, the thermal contact resistance model was applied and the thermal resistance was modeled by placing a small solid block between the two contacting spheres in the simulation. In the present paper, the applicability of this model was then examined by comparing with the experiments.

5.2 Theoretical analysis

5.2.1 Numerical simulation for contact transfer modelling

Figure 5.1 shows a schematic of the problem. The characteristics of the cylindrical bar in the simulation are the same with the stainless steel SUS304 that are used in the experiments. The diameter of the cylindrical bar is 0.0191m and the radius and height of the cylindrical analysis volume are 0.12 and 0.14m, respectively.

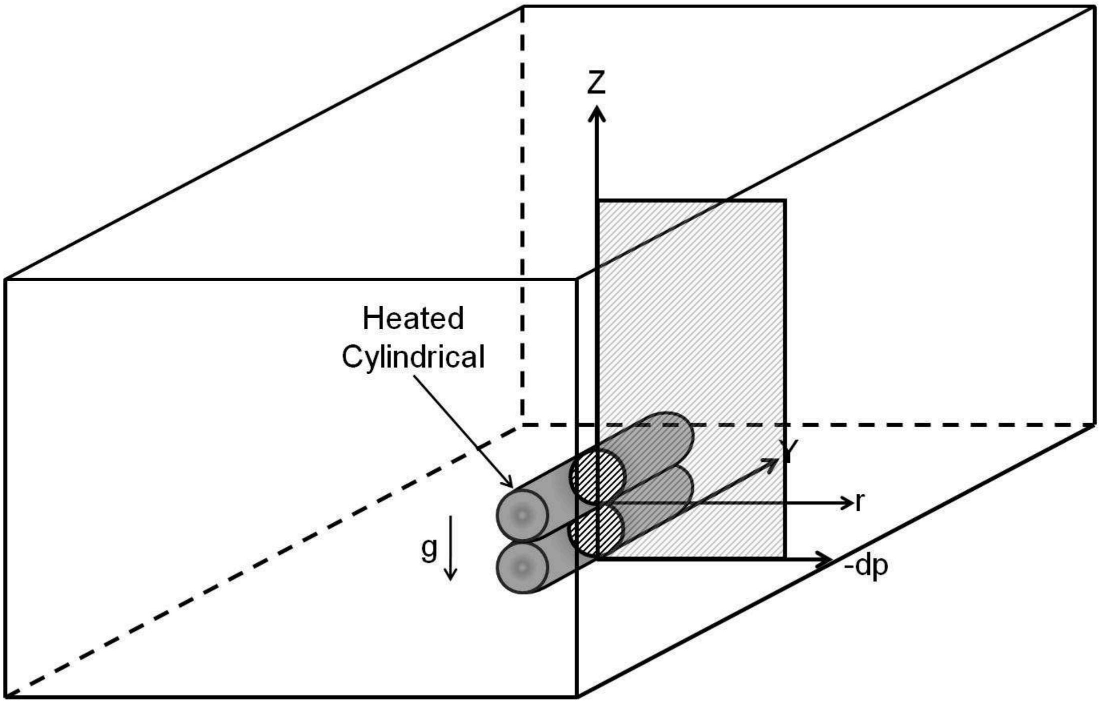

Figure 5.1: Problem Schematic

For the numerical simulation, FLUENT 6.1.22 was utilized. The computational grid system for the present simulation is shown in Figure 5.2. It is assumed that the flow and the temperature are axisymmetric.

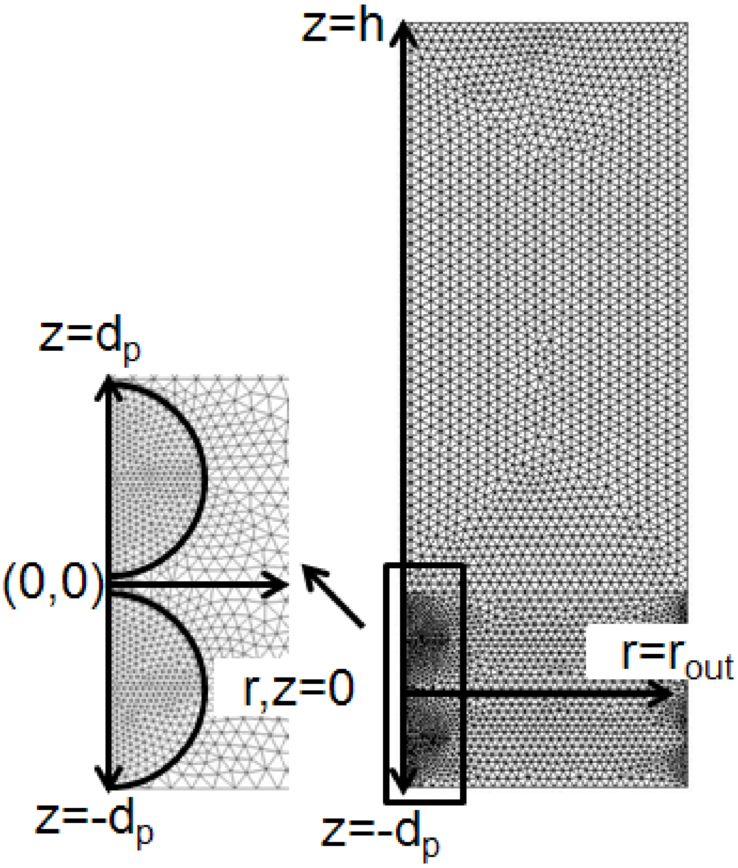

Figure 5.2: Computational mesh

The properties of the cylindrical bar and the air used in the simulation are indicated in Table 5.1.

Table 5.1: Properties of sphere and air

Properties	sphere	air
$\rho\ [kg \cdot m^{-3}]$	7930	1.205
$c_p\ [J \cdot kg^{-1} K^{-1}]$	500	718
$\lambda\ [W \cdot m^{-1} K^{-1}]$	1,5,8,16.8	0.0257
$\mu\ [Pa \cdot s]$	-	1.512×10^{-5}

For the present numerical simulation, the upper particle was heated to 50, 100 and 150°C. The lower particle was initially set at 23°C, which is the same as the ambient temperature. This state was set as the initial condition. The boundary conditions are shown as follows:

Velocity,

$$\vec{v} = 0 \qquad at \qquad r = r_{\mathrm{out}} \tag{5.1}$$

$$v_{\mathrm{r}} = 0, \frac{dv_{\mathrm{z}}}{dr} = 0 \qquad at \qquad r = 0 \tag{5.2}$$

$$\frac{dv}{dz} = \frac{dv_{\mathrm{z}}}{dz} = 0 \qquad at \qquad z = h, -d_{\mathrm{p}} \tag{5.3}$$

$$\vec{v} = 0 \qquad \text{on sphere surface} \tag{5.4}$$

Temperature,

$$T = 23°C \qquad at \qquad r = r_{\text{out}} \tag{5.5}$$

$$\frac{\partial T}{\partial x} = 0 \qquad at \qquad r = 0 \tag{5.6}$$

$$T = 23°C \qquad at \qquad z = -d_{\text{p}} \tag{5.7}$$

$$\frac{\partial T}{\partial y} = 0 \qquad at \qquad z = h \tag{5.8}$$

5.2.2 Modeling of the thermal resistance

If the particle surface roughness is directly taken into account in a numerical simulation of heat transfer between contacting particles, the configuration of surface roughness must be considered. Since the actual scale of the surface roughness from a measurement is around $0.1 - 10\mu$m, it is almost impossible to simulate with the present simulation method due to the problem of computer capacity.

Accordingly, the thermal resistance was modeled by using a virtual small solid in the present simulation. A small solid was placed between the contacting particles as shown in Figure 5.3.

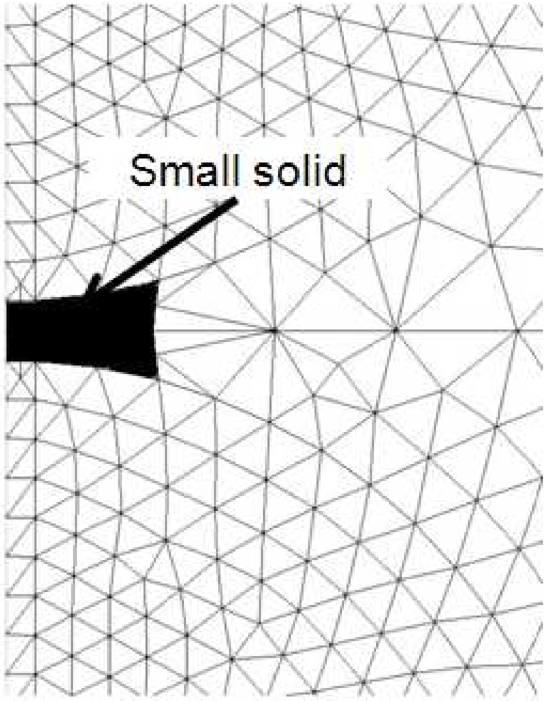

Figure 5.3: Computational mesh assigned for small solid

The radius and thickness of the small solid are 2.5 and 1mm, respectively. The equation for thermal resistance model is expressed as follows:

$$q = h_m(\theta_{\mathrm{h}} - \theta_{\mathrm{c}}) \tag{5.9}$$

where h_{m} is the thermal conductance and $1/h_m$ is the thermal resistance. On the other hand, the thermal conduction equation can be expressed as follow:

$$q = \frac{\lambda}{\delta}(\theta_{\mathrm{h}} - \theta_{\mathrm{c}}) \tag{5.10}$$

where λ is the thermal conductivity of the small solid and δ is considered as the surface roughness. By comparing equation (5.9) and equation (5.10), $\frac{\delta}{\lambda}$ is the equivalent thermal resistance. The thermal conductivity of the small solid was changed from $\lambda = 1, 5, 8, 16.8\mathrm{W} \cdot \mathrm{m}^{-1}\mathrm{K}^{-1}$ in the simulations to obtain the value equivalent to the measured thermal resistance.

5.3 Experiment

5.3.1 Research equipment

Infra-Red Thermo Camera

Table 5.2: Infra-Red Thermo Camera

Model	TH9100 Pro Series (NEC Inc.)
Temperature measurement	Range1: 20 ∼ 126, 100 ∼ 176 °C Range2: 0 ∼ 124, 250 ∼ 176 °C
Temperature resolution	0.06 ∼ 176 °C
Focus range	$30cm \sim \infty$
Angle of view	Horizontal 21.7 ∼ 176 Vertical 16.4 ∼ 176
Sampling frames speed	60 frame/s
Effective pixels	320 (H) ∼ 180, 240 (V) dots
Depth of data	4 bits
Measurement mode	Run/Freeze
Auto functions	Full-auto, Level-trace, Auto-gain controller
Real time recording image resolution	1664 pixels
Dimensions	L 189 ∼ 180, W 108 ∼ 180, H 113 mm
Weight	$1.4kg$ (without battery)
Long wavelength spectral range	$(8\mu m \sim 14\mu m)$
Effective pixels	41 Megapixels
Minimum sensitivity	1 Rucks
Proximity magnifying lens	$95\mu m$
Focal length	$17mm$ Fix focal

Figure 5.4: Thermal infra-red camera

3D Ultraviolet laser profile microscope

Table 5.3: 3D Ultraviolet laser profile microscope specifications

Model	Microscope Head VK-9710 (KEYENCE. Inc)
Controller	VK-9700 (KEYENCE. Inc)
Objective lens magnification	$10\times \sim 150\times$
Observation range (horizontal)	$1350\mu m \sim 90\mu m$
Observation range (vertical)	$1012\mu m \sim 67\mu m$
Operation distance	$16.5mm \sim 0.2mm$
Height measurement range	$7mm$
Resolution display	$0.001\mu m$
Repeat accuracy	$0.02\mu m$
Weight	Microscope head: $26kg$; Controller: $11kg$

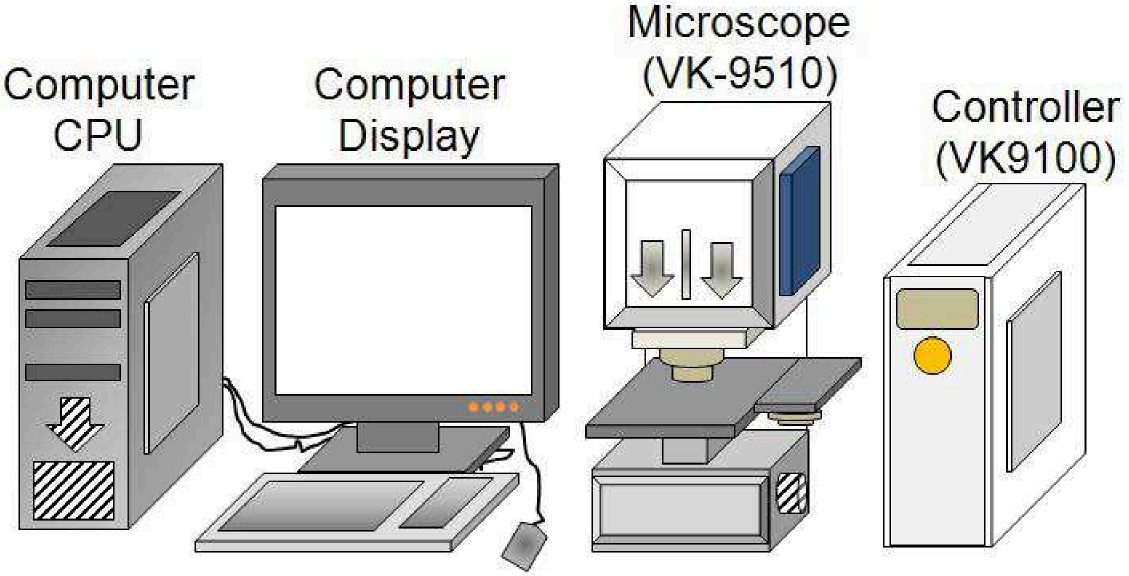

Figure 5.5: 3D Ultraviolet laser profile microscope

Heating equipment

This section gives the description about the volt slider, mantle heater for cylinder pipes which is mainly the common tools used for the heat transfer research.

Mantle heater connected to the volt slider were wrapped around the pipe and heated. The stainless steel cylindrical bar were put inside the pipes to be heated. At that time, the temperature adjustment is done while measuring the temperature of the bar with the temperature-measuring device by the volt slider.

Table 5.4: Heating equipment specifications

Voltage slider	
Model	N-130-10 YAMABISHI ELECTRIC
Heating mantle with cylinder	
Measurement (Diameter × Length)	$20 \times 100mm$
Maximum Temperature	$400 \sim$ °C
Power Supply Voltage	AC100V

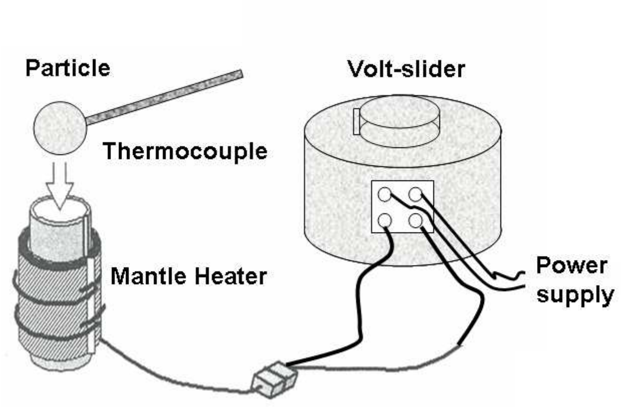

Figure 5.6: Apparatus set-up used to heat particle at desired temperature

Particle Imaging Velocimeter (PIV)

Figure 5.7 shows the outline of the PIV system. The system is composed of double pulse YAG laser source, synchronizer, CCD camera, control PC, and image processing software ”Insight”.

The PIV system is used for the speed measurement of the flow field. It is a speed measuring instrument (Velocimeter) that calculates the speed by irradiating the laser light (double pulse laser light) twice in a very short course, and by measuring the distance of the bar by the two images taken makes the flow field visibly.

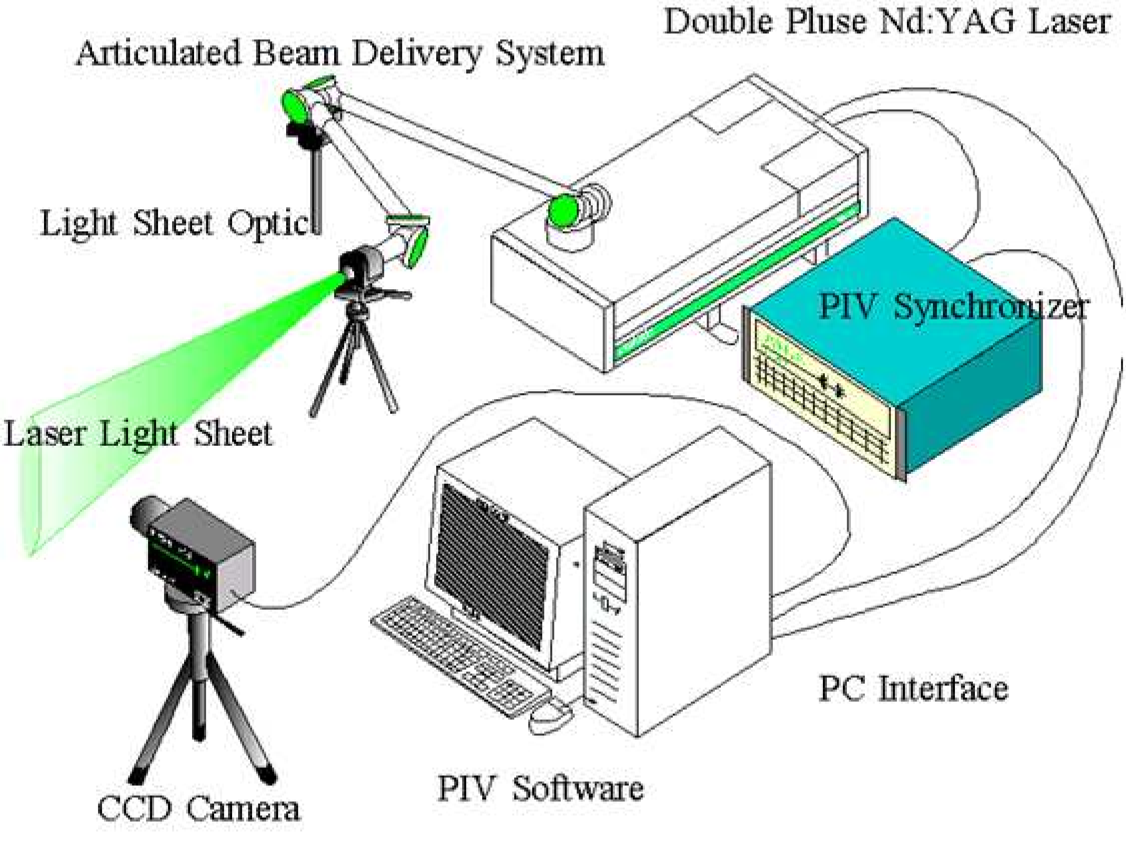

Figure 5.7: PIV system set-up

Table 5.5: Particle Image Velocimetry (PIV) system specifications.

Double pulse YAG Laser Source	
Model	PV200 (B.M. Industries)
Laser type	Double Pulse Nd: YAG Laser
Pulse interval	$5 \sim 20ns$
Pulse energy	$10mJ \sim 3.0J$
Laser wavelength	$532nm$
Lens type	Concave with focal length = 1000 mm
Power supply	AC 200V; 50 - 60Hz
Synchronizer	
Model	610032 Laser Pulse Synchronizer (TSI Inc.)
Power Supply	ACV 100; 50-60 Hz
Input	External synchronizer
	Photo camera feedback signal
	Image shifter system signal
Output	Flash lamp
	Q switch trigger signal
	Mirror image shifter trigger signal
CCD Camera	
Model	PIVCAM 10 - 30 CCD Camera (Kodak Inc.)
CCD type	Progressive Scan Interline CCD
Effective pixels	$1000 \sim 1016$ pixels
Pixel format	$9\mu m \sim 9\mu m$
Frame rate	30 fps (Max)
Telezoom Lens	AF NIKKOR 24 - 50 mm F3 (Nikon Inc.)

Simulation Software

FLUENT software contains the broad physical modeling capabilities needed to model flow, turbulence, heat transfer, and reactions for industrial applications ranging from air flow over an aircraft wing to combustion in a furnace, from bubble columns to oil platforms, from blood flow to semiconductor manufacturing, and from clean room design to wastewater treatment plants [43].

FLUENT technology is a leader in the number of complex physical models offered for solution on unstructured meshes. Combinations of elements in a variety of shapes are permitted such as quadrilaterals and triangles for 2-D simulations and also hexahedra, tetrahedral, polyhedral, prisms and pyramids for 3-D simulations. Meshes can be created using ANSYS or third-party meshing products such as Gambit, TGrid and many others. Meshes containing many cells, even over a billion, can quickly be automatically partitioned when they are read into ANSYS FLUENT software running on a compute cluster. Additional built-in tools built can be used to further manipulate meshes.

For the mesh software, Gambit, a grid generation tool and also for geometric modeling are used. GAMBIT can create their own geometry or import geometry from most CAD packages. It also can automatically mesh surfaces and volumes while allowing the user to control the mesh through the use of sizing functions and boundary layer meshing.

Table 5.6: PC specification for simulation

Model	ASUS
CPU	Intel Celeron (R) 2.4GHz
Memory	1.4GB
OS	Windows XP Professional

5.3.2 Experiment method

Two stainless steels cylindrical bar (SUS304) were utilizes as particles in the present experiment. The size of the particles is 0.0191m, which is the same used in the numerical simulation. For the experiment, the two particles were set in a vertical arrangement and statically in contact as shown in Figure 5.8.

The temperature distribution of the stainless steel bar along the center axis having a half groove as shown in Figure 5.8 was measured. The temperature on the groove, i.e. the temperature on the center axis was observed using IR camera (NEC san-ei Instruments Ltd., Japan, TH9100 PMV). The temperature distribution was recorded and then calculated using the thermal imager software (TH91-703).

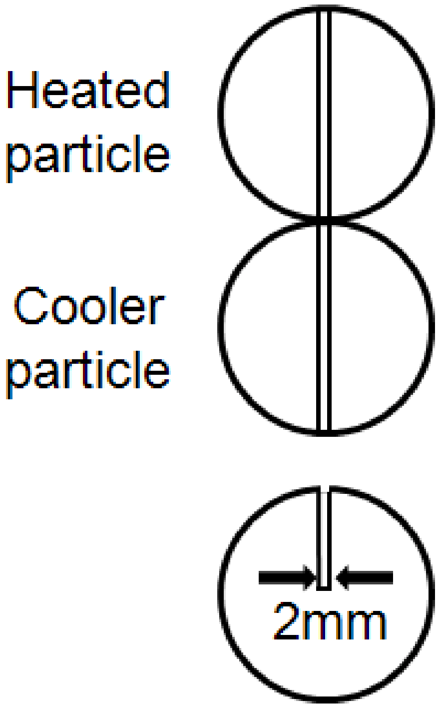

Figure 5.8: Grooved particles for temperature distribution measurement

In order to reduce the effect of the air inflow and any other disturbances, the analysis domain around the particles was surrounded by an acrylic cylindrical tube whose radius and height are 0.12 and 0.14m, respectively.

The experiment conditions for the stainless steel particles are shown in Table 5.7.

Table 5.7: Experiment conditions

Particle diameter (SUS304) [m]	0.0191
Particle mass [kg]	2.82×10^{-2}
Specific heat $[J \cdot kg^{-1}K^{-1}]$	0.50×10^{3}
Young modulus [GPa]	184.36 at 150°C
Gas viscosity $[Pa \cdot \mathrm{s}]$	1.512×10^{-5}
Poisson ration [-]	0.29
Heated temperature [°C]	50, 100, 150
Contact force [N]	100, 200, 300, 400, 500

The temperature of particles was measured using two methods, Infra Red thermal imager camera (IR camera) and the thermocouple shown in Figure 5.9.

The stainless steel spheres used as particles were painted in matte black color to reduce the reflection for the IR camera before the measurement. Experiments using the thermocouple have been made to check the effect of the paint. Since the temperature differences between the non-painted and the painted ones were $1 - 2$°C, the influence was ignored.

The upper particle was heated to 50, 100 and 150°C while the lower particle was set to the same as room temperature: 23°C. After the upper particle was heated it was then brought into contact with the lower particle. This condition was regarded as the initial condition.

As shown in Figure 5.9, a small hole was drilled so that the thermocouple can be inserted into the center of the stainless steel particles to measure the temperature. The temperature was recorded on the computer. The pressure gauge was used to set a contact force between

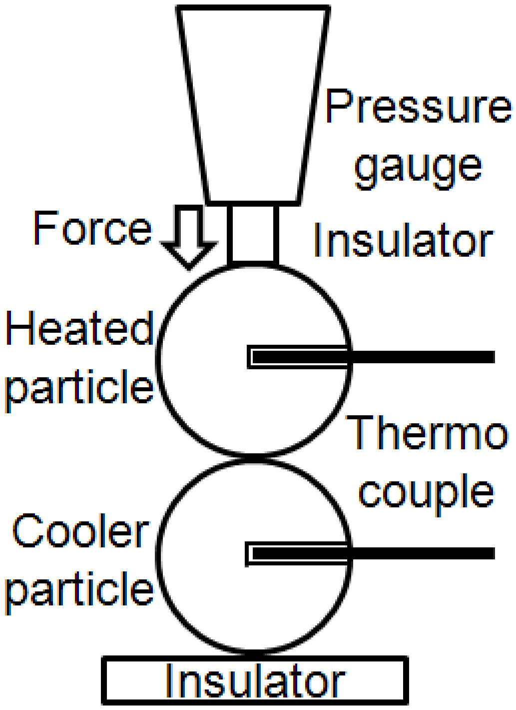

Figure 5.9: Temperature measurement using thermocouple

the contacting particles. The contact forces were 100, 200, 300, 400 and 500N.

The gas flow of the particles at 50, 100, 150°C was observed with Schlieren apparatus (Katou Kouken Ltd., S880, Japan).

5.4 Results and Disccussion

5.4.1 Flow visualization around the contacting spheres

In order to validate the numerical simulation, the gas flow pattern and the temperature distribution around the two contacting particles were compared with the experimental one. Figure 5.10 shows the temperature distribution of the gas phase observed by Schlieren method.

Figure (a) is for the initial temperature of 50°C, Figure (b) of 100°C and Figure (c) is of 150°C. All the photos were taken at the same time equal to t=180s. From these photos observed by Schlieren method,the temperature distribution, seen as a white shadow around the upper particle,shown that when the upper particle temperature increases, the white shadow of the temperature of gas layer around the particle is also increases.

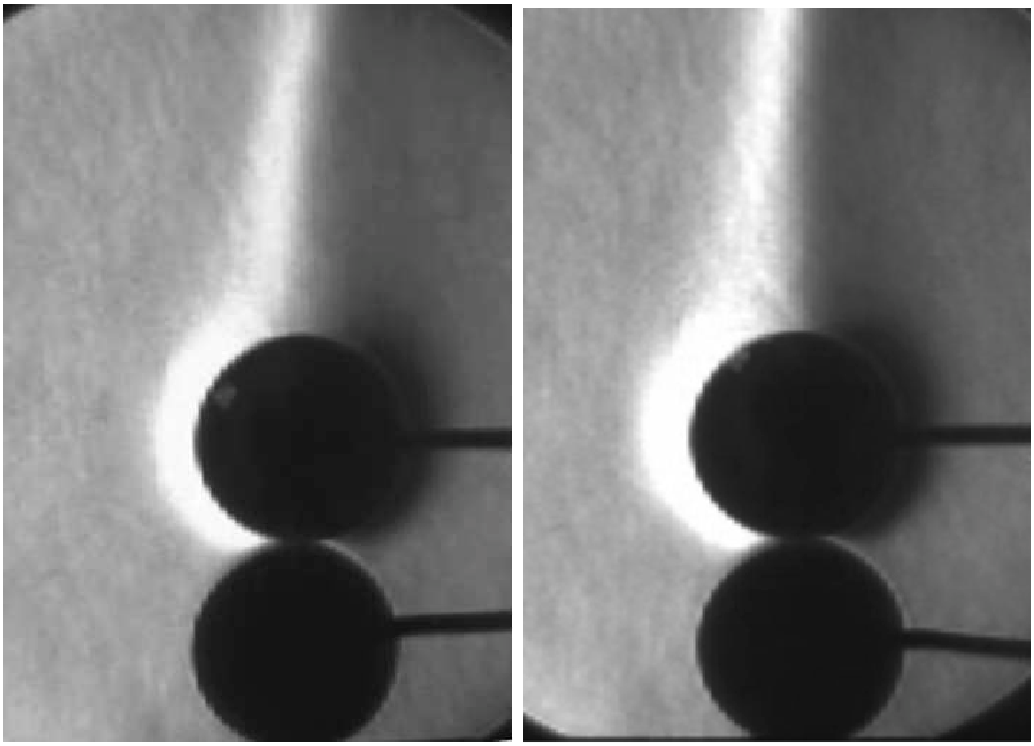

(a) Upper particle heated at 50°C (b) Upper particle heated at 100°C

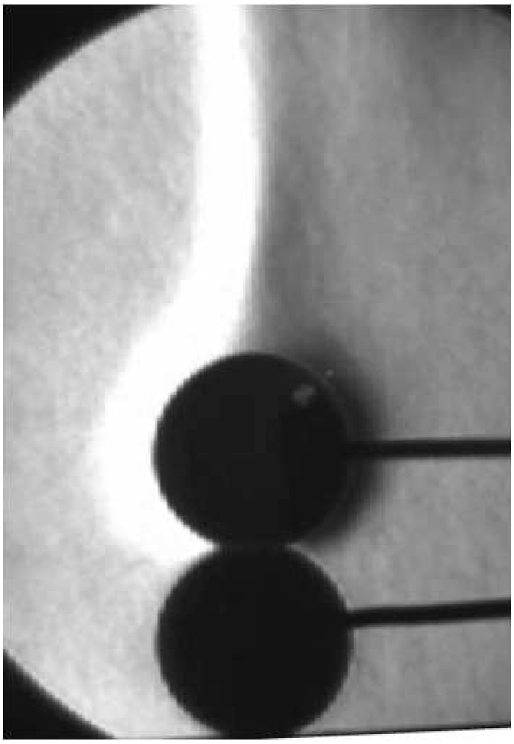

(c) Upper particle heated at 150°C

Figure 5.10: Gas phase observed by Schlieren method

Figure 5.11 shows isotherms visualized by the simulation around the contacting particles and the data were also taken at the time: t=180s. Here, the temperature of the upper particle was set at (a) 50°C (b) 100°C and (c) 150°C before the contact. The temperature distribution of gas phase is similar to that observed with Mach-Zehnder interferometer by Kuwagi *et al.* [44]. Furthermore, the temperature phase around the upper particle well agrees with the simulated one. From the visualization, the heat from the upper particle is transferred not only to the atmosphere but also to the lower particle by thermal conduction. From these figures, the heat from the upper particle of (a) 50°C is transferred more slowly than from the upper particle of (b) 150°C.

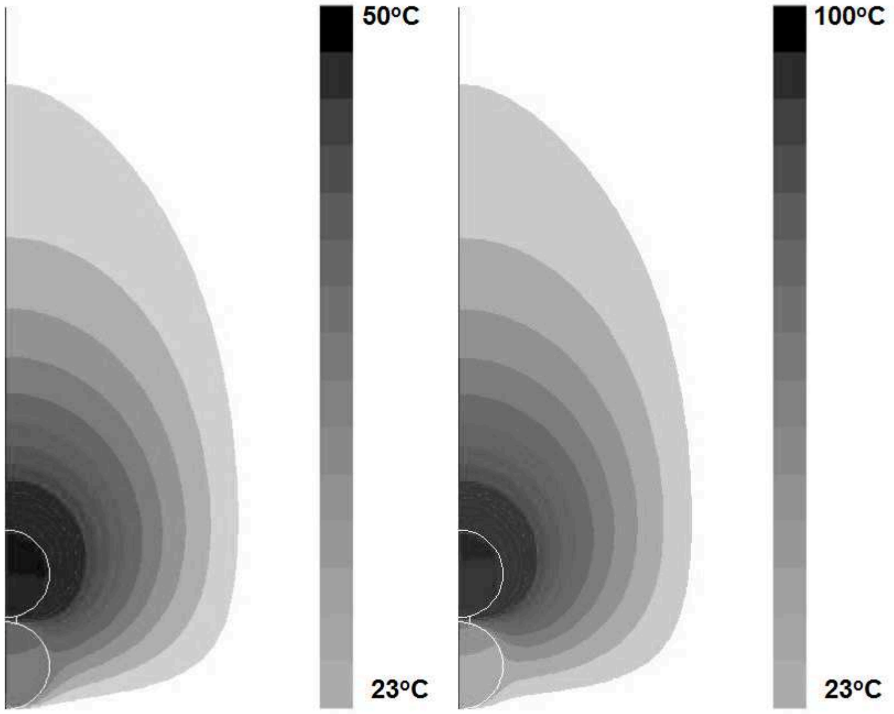

(a) Upper particle heated at 50°C (b) Upper particle heated at 100°C

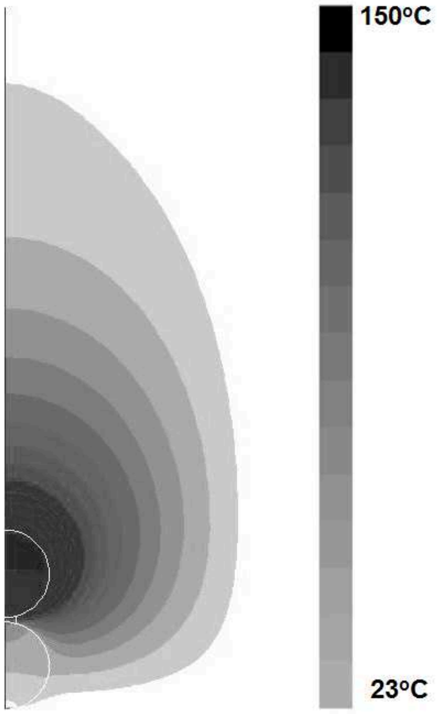

(c) Upper particle heated at 150°C

Figure 5.11: Isotherms around contacting particles

5.4.2 Temperature distribution along center axis

Figure 5.12 shows the temperature distribution along the center axis for (a) experiment, (b) simulation with $\lambda = 0.5\mathrm{W}\cdot\mathrm{m}^{-1}\mathrm{K}^{-1}$ for the small solid, (c) simulation with $\lambda = 1\mathrm{W}\cdot\mathrm{m}^{-1}\mathrm{K}^{-1}$ and (d) simulation with $\lambda = 16.8\mathrm{W}\cdot\mathrm{m}^{-1}\mathrm{K}^{-1}$. The temperature distribution was recorded from t=0s until 300s.

In Figure 5.12 (d), since the value of the thermal conductivity is the same as that of particle, this state can be regarded as non thermal resistance, i.e. perfect contact. The heat from the upper particle is transferred to the lower particle and then both of the particle temperature becomes almost equal at the time t=300s.

By comparing with experimental data shown in Figure 5.12 (a), the thermal conductivity should be lower than $16.8\mathrm{W}\cdot\mathrm{m}^{-1}\mathrm{K}^{-1}$. The thermal conductivity of the small solid was then changed to the lower value and Figure 5.12 (c) with the thermal conductivity $\lambda = 1\mathrm{W}\cdot\mathrm{m}^{-1}\mathrm{K}^{-1}$ gives the best agreement with the experiment in Figure 5.12 (a).

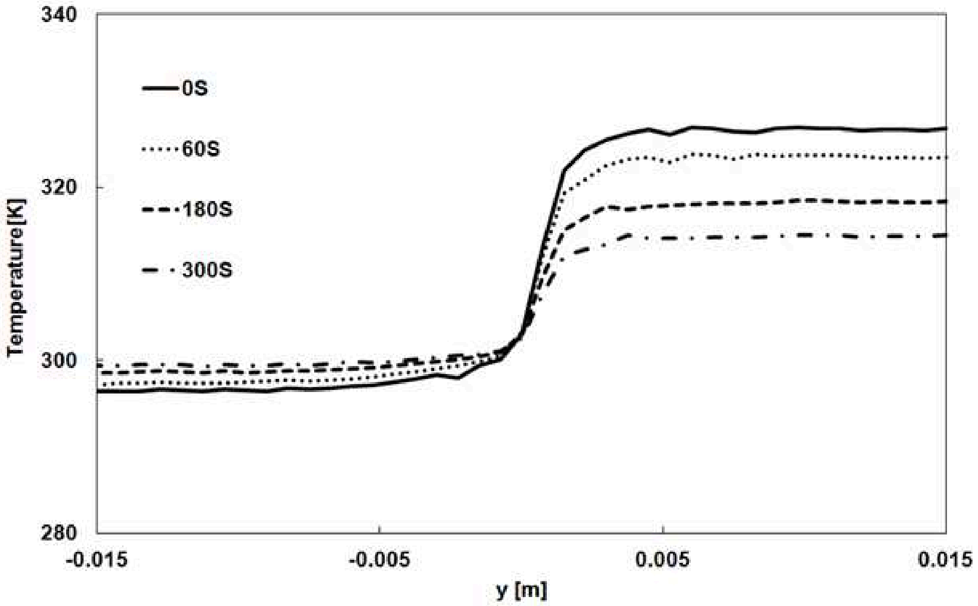

(a) Experiment

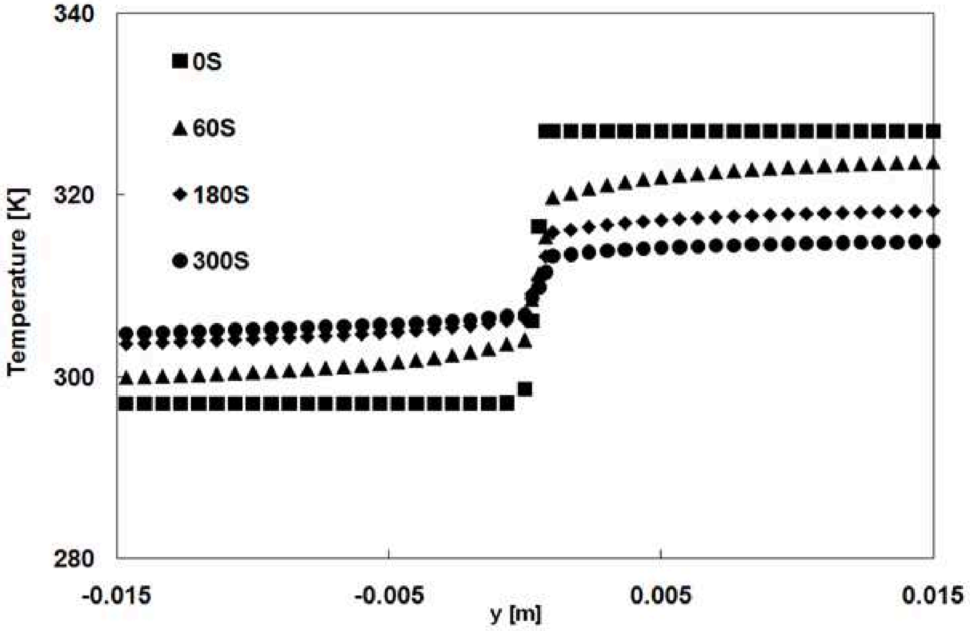

(b) simulation with $\lambda = 0.5$

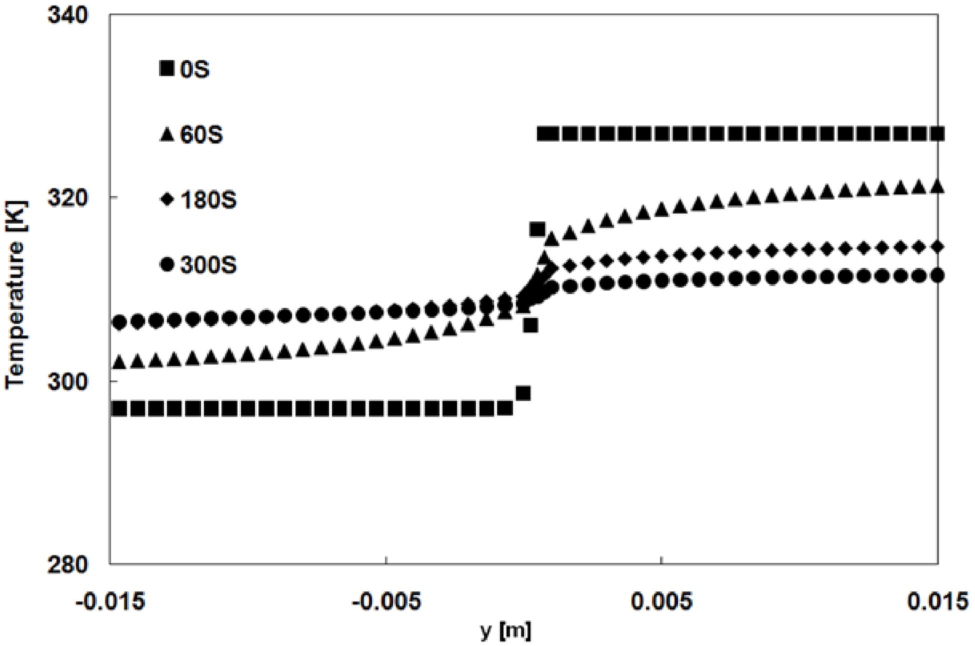

(c) simulation with $\lambda = 1$

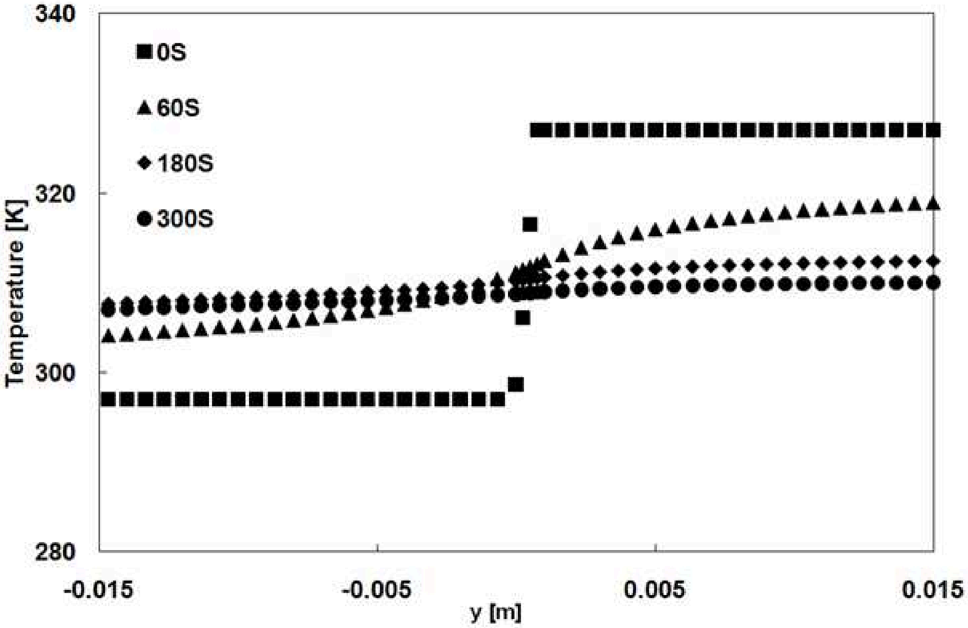

(d) simulation with $\lambda = 16.8$

Figure 5.12: Temperature distribution along center axis

Figure 5.13 shows the temperature at the center of both the upper and lower particles with various thermal resistances in the simulation. As explained above for the Figure 5.12, when the thermal conductivity is at $16.8\mathrm{W}\cdot\mathrm{m}^{-1}\mathrm{K}^{-1}$ there is no thermal resistance. The thermal conductivities were changed from 0.5 to $16.8\mathrm{W}\cdot\mathrm{m}^{-1}\mathrm{K}^{-1}$.

From this change of thermal conductivity, the case of $1\mathrm{W}\cdot\mathrm{m}^{-1}\mathrm{K}^{-1}$ best agrees with the experimental one. In Figures 5.13 (a), (b) and (c), the thermal conductivity at $1\mathrm{W}\cdot\mathrm{m}^{-1}\mathrm{K}^{-1}$ gives best agreement in all three temperature cases.

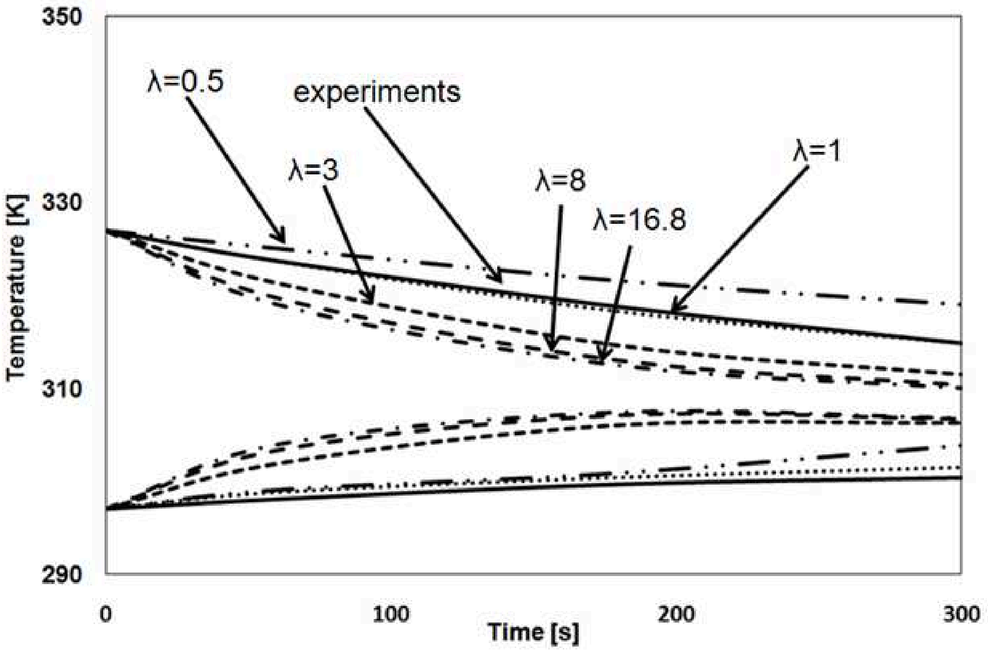

(a) Results started at temperature $T = 50°\mathrm{C}$

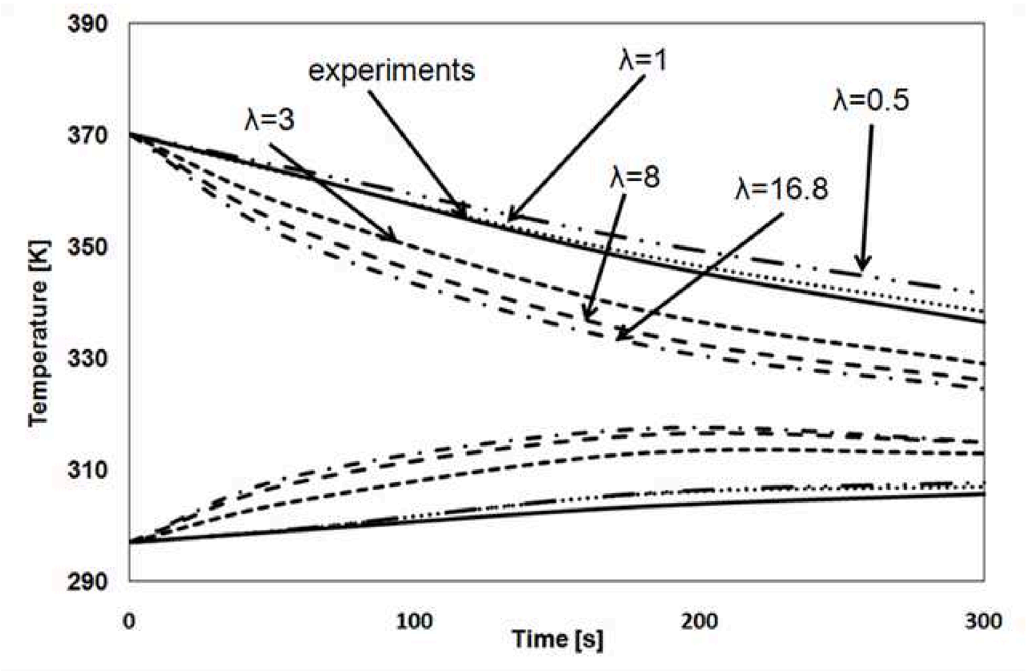

(b) Results started at temperature $T = 100°\mathrm{C}$

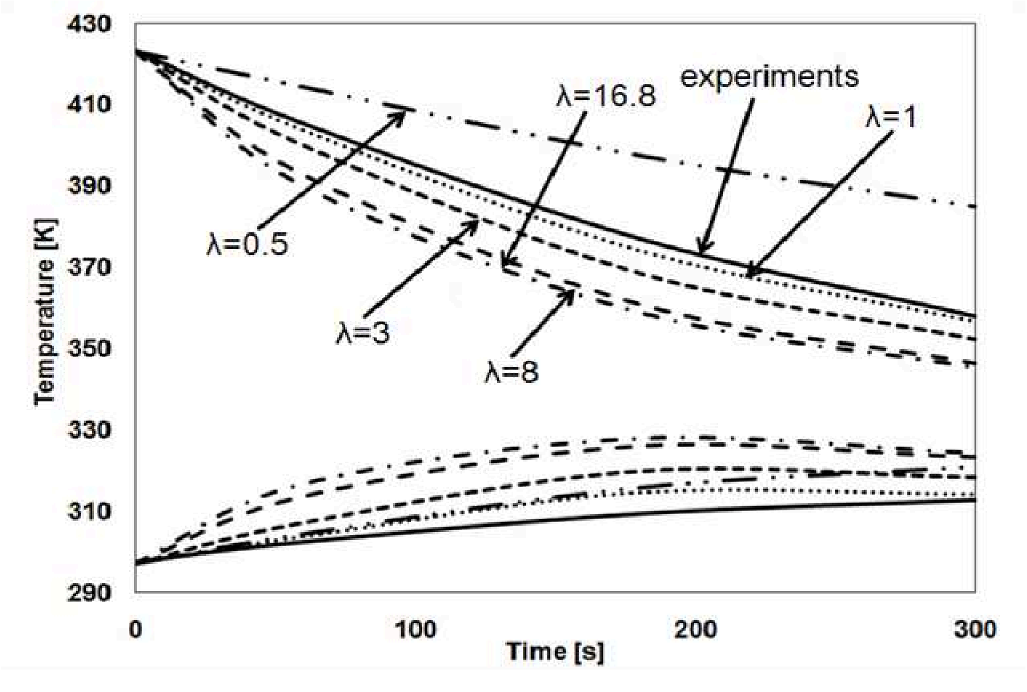

(c) Results started at temperature $T = 150°\mathrm{C}$

Figure 5.13: Temperature validation at center of particles

5.4.3 Contact heat transfers at various temperatures

Figure 5.14 shows the contact heat transfer with the initial temperatures of the heated particle: (a) 50, (b) 100 and (c) 150°C The graphs also show the contact heat transfers calculated with Zhang *et al.* [45] equation for the thermal resistance model. The calculated contact heat transfers between particles contacting horizontally are also plotted. Figure 5.14 (a), the contact heat transfer between the horizontally contacting particles well agrees with that vertically contacting particles, although the calculated result becomes larger as the contact force becomes larger.

In Figure 5.14 (b), the contact heat transfer between vertically contacting particles well agrees with that between the horizontally contacting particles. The values of contact heat transfer calculated for this initial temperature are 1.5 times larger than the experimental ones. This would be caused by some difference in the contact area and the surface roughness between the real situation and the calculation.

In Figure 5.14 (c), the contact heat transfers between the vertically contacting particles are larger than the horizontal contacting particles and also by experimental result (Kuwagi *et al.* [44]. The calculated results are a few times larger when the contact force is large. The experiment results also shows that the contact heat transfers for both the vertical and horizontal arrangements also become larger as the contact force is larger but the increments are small.

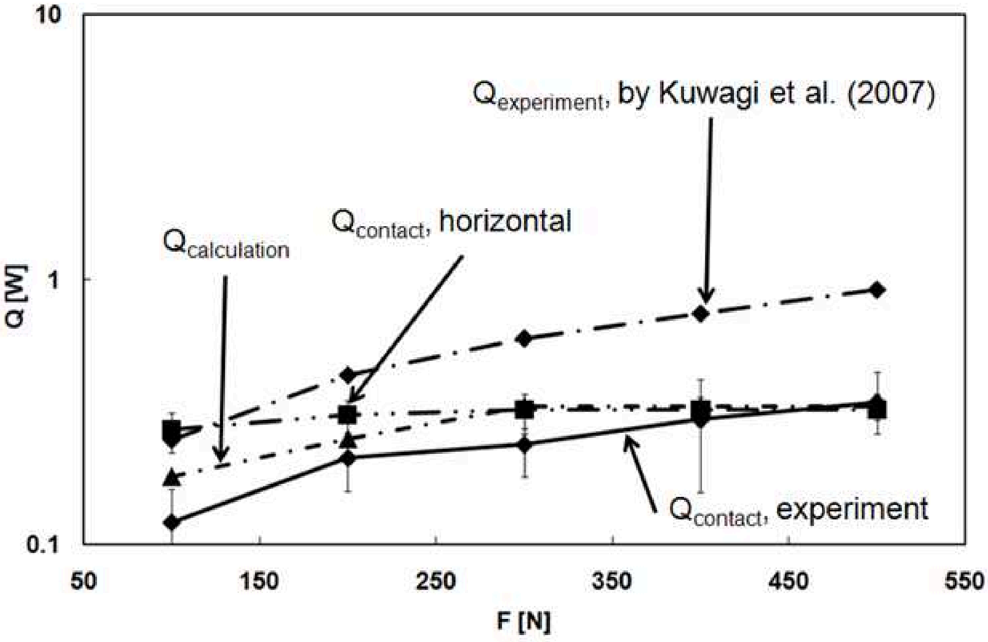

(a) Results at initial temperature $T = 50°\mathrm{C}$

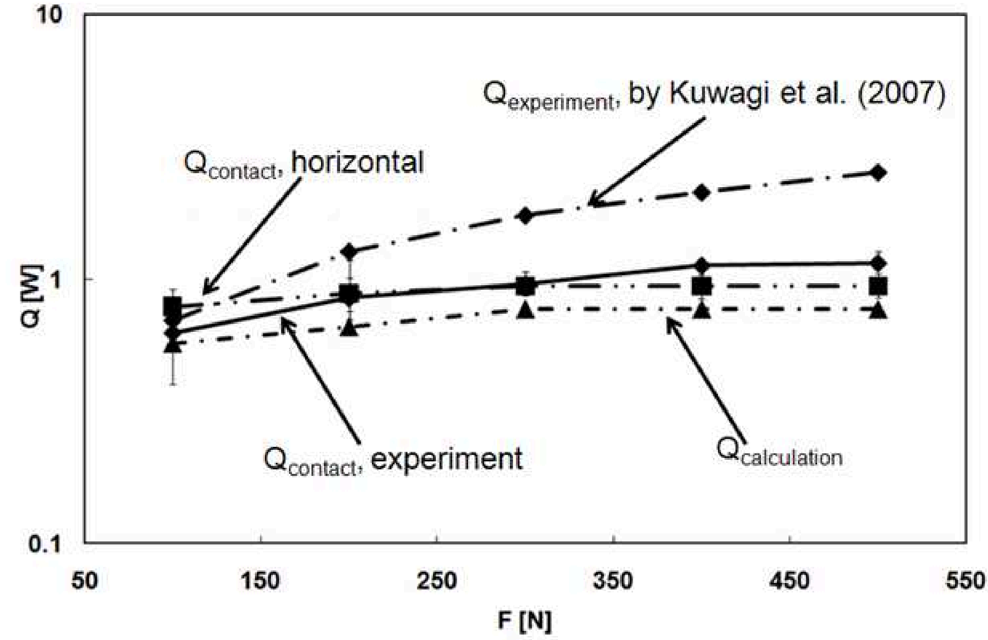

(b) Results at initial temperature $T = 100°\mathrm{C}$

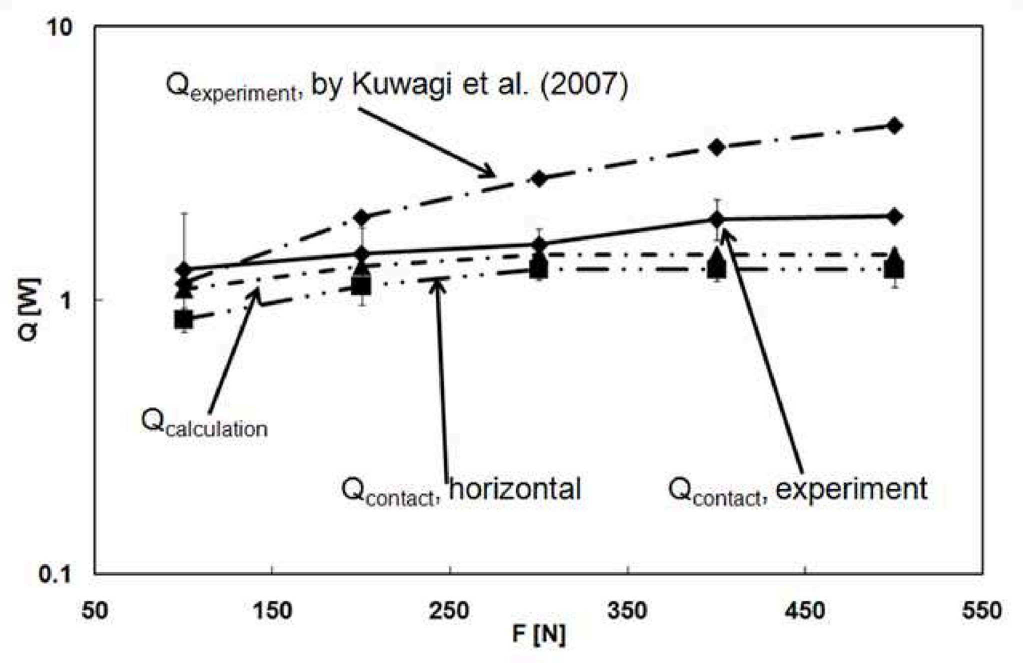

(c) Results at initial temperature $T = 150°\mathrm{C}$

Figure 5.14: Contact heat transfer at various temperatures

5.5 Chapter conclusions

For the modeling of thermal resistance between contacting particles, a small solid was used to simulate thermal resistance in the numerical simulation. As a result, the temperature distribution similar to that caused by the thermal resistance could be reproduced.

The temperature distribution simulated with the thermal conductivitiy of $1\text{W} \cdot \text{m}^{-1}\text{K}^{-1}$ well agreed with the experimental one near the contact point, where thermal conductivity for SUS304 of $16.8\text{W} \cdot \text{m}^{-1}\text{K}^{-1}$ did not agree with the experimental one.

From the results of the contact heat transfer, the difference of the heat transfer between the horizontal and the vertical arrangements of the particles was small. Accordingly, the effect of the particles arrangement would be able to be ignored in the contact heat transfer. Thus, the horizontal arrangement data, which can be easily obtained in the experiments, can be used for a comparison with the numerical simulation and vertical arrangements in terms of contact heat transfer.

When surface roughness and contact force are changed in the experiments, the width, thickness and conductivity of the small solid between particles in the present model should be also changed to obtain the same results as the experiments. In order to establish the present model with the small solid, the relationship between contact force and the width of small solid must be examined. Furthermore, the influence of surface roughness on the thickness of the small solid must be studied.

CHAPTER 6

CONCLUSIONS

Discrete Element Method (DEM) is a very useful tool to analyze a fluidized bed for various powder processes also possible to incorporate problem–factors in the level of particle size. However, in spite of the fact that DEM can be applied to problem pertaining to cohesion, heat transfer and chemical reaction, it is impossible to use DEM for dealing with phenomena whose scale is smaller than the particle size, such as the heat transfer between the colliding particles, the effect of drag, lubrication, and lift forces.

In order to examine and clarify the small scale phenomena occurred in fluidized bed, we had utilized Immersed Boundary Method (IBM) which is one of the DNS and also a study of heat transfer between the particles has been done.

In chapter 3, in order to validate the IBM for multiphase flow, a study of lift forced and viscous torque has been carried out. In this study, the effect of calculation of the analysis domain size, simulation mesh size, and simulation sub-mesh size has been implemented.

From these results of the study of effectiveness of IBM, it is considered the influence of the simulation sub-mesh size gives less effect to the analysis results; however a much finer simulation mesh system would be needed for the present simulation.

In chapter 4, The IBM was used to study the drag force acting on both dilute and dense particles and in order to examine the effect of particle arrays, the relationship between the drag force and flow in a simple manner, particles were arranged in a two-dimensional pattern.

In this study, for the drag force on a single particle, the simulation results were compared with the results estimated using the Schiller and Naumann (Schiller and Naumann, [36]) and White (White, [37]) equations. For the cases of dilute–particle arrangements, the simulated drag coefficient agreed well with that estimated using the Cello *et al.* [35] equation. On the other hand, the drag coefficient for dense particles approached the values estimated using the Ergun (Ergun, [31]) equation in the case of staggered particle arrangement, whereas in the case of inline particle arrangement, the simulated drag coefficient approached the values estimated using the Cello *et al.* [35] equation as the Reynolds number increased.

Lastly in chapter 5, for the contact heat transfer between particles, the thermal contact resistance model was applied and the thermal resistance was modeled by placing a small solid block between the two contacting spheres in the simulation. The applicability of this model was then examined by comparing with the experiments.

When the surface roughness and contact force are changed in the experiments, the width, thickness and conductivity of the small solid between particles in the present model should be also changed to obtain the same results as the experiments. In order to establish the present model with the small solid, the relationship between contact force and the width of small solid must be examined. Furthermore, the influence of surface roughness on the thickness of the small solid must be studied.

6.1 Chapter nomenclature

a^* = dimensionless velocity gradient [-]

A = frontal area [-]

$\overline{C_{\mathrm{D}}}$ = drag coefficient for multiple particles [-]

C_{D} = drag coefficient [-]

C_{L} = lift coefficient [-]

C_{LR} = lift rotation coefficient [-]

C_{T} = dimensionless torque coefficient [-]

c_{p} = specific heat of particles $[J \cdot kg^{-1}K^{-1}]$

d_{p} = particle diameter $[m]$

d_{p} = particle diameter $[m]$

E = Young modulus $[Pa]$

F = contact force $[N]$

F_{D} = drag force $[N]$

F_{L} = lift force $[N]$

F_{LR} = lift rotation force $[N]$

$F_{\mathrm{D,stokes}}$ = drag force in Stokes flow $[N]$

$\vec{F}_{\mathrm{n}}$ = force in normal direction $[N]$

$\vec{F}_{\mathrm{t}}$ = force in tangential direction $[N]$

f_{D} = drag force per unit volume $[N \cdot m^{-3}]$

f = dimensionless drag force [-]

f_{ib} = body force term for the IB method $[N \cdot m^{-3}]$

f_{vis} = viscous force $[N \cdot m^{-3}]$

$\vec{g}$ = gravitational acceleration $[m \cdot s^{-2}]$

I = current $[A]$

g = gravitational acceleration $[m \cdot s^{-2}]$

H_{m} = thermal resistance $[\mathrm{W} \cdot \mathrm{m}^{-1}\mathrm{K}^{-1}]$

H,h = height of column $[m]$

$\vec{I}_{\mathrm{p}}$ = inertia moment of particle $[kg \cdot m^{-2}]$

K_0 = model coefficient defined in Eq. (13) [-]

K_1 = model coefficient defined in Eq. (13) [-]

K_2 = model coefficient defined in Eq. (13) [-]

K_3 = model coefficient defined in Eq. (13) [-]

L = lenghtand width of column $[m]$

m_{p} = particle mass $[kg]$

P = pressure $[N]$

Q_{cont} = contact heat transfer $[W]$

q = heat transfer $[W]$

$Re_{\mathrm{p}\varepsilon}$ = particle Reynoylds number in the case of voidage [-]

Re_{p} = particle Reynoylds number [-]

Re_{R} = rotating Reynoylds number [-]

r_{p} = particle radius $[m]$

T = temperature $[^{\circ}C]$

T = thickness of column $[m]$

T_{f} = torque [-]

t = time $[s]$

u = gas velovity $[m \cdot s^{-1}]$

u_{f} = fluid velocity $[m \cdot s^{-1}]$

u_{g} = gravitational velocity $[m \cdot s^{-1}]$

u_{r} = rotational velocity $[m \cdot s^{-1}]$

V_{p} = particle volume $[m^3]$

v_{p} = particle velocity $[m \cdot s^{-1}]$

W = width of column $[m]$

x, y, z = coordinate $[m]$

β = drag factor defined in Eq. (4.2) $[N \cdot m^{-4} \cdot s]$

Δ = computational grid size $[m]$

Δt = time step $[s]$

Δx = computational grid size $[m]$

Δy = computational grid size $[m]$

Δz = computational grid size $[m]$

δ = computational sub grid size $[m]$

ε = voidage [-]

ε_{p} = particle volume fraction [-]

μ = viscosity $[Pa \cdot s]$

ρ_{f} = fluid density $[m]$

ρ_{g} = gas density $[kg \cdot m^{-3}]$

ω_{p} = angular velocity of particle $[rad \cdot s^{-1}]$

λ = thermal conductivity of small solid $[\mathrm{W \cdot m^{-1} K^{-1}}]$

ϵ = Poisson ratio [-]

ρ = density $[kg \cdot m^{-3}]$

δ = surface roughness $[m]$

BIBLIOGRAPHY

[1] D Kunii and O Levenspiel. *Fluidization Engineering.* Elsevier, 2 edition, 1991.

[2] IUSE Fraunhofer. *Fraunhofer Institute for Environmental, Safety and Energy Technology UMSICHT in Oberhausen, Germany.* Copyright Fraunhofer IUSE.

[3] Li H. He, F. and Z. Zhao. *Advancements in Development of Chemical-Looping Combustion: A Review.* International Journal of Chemical Engineering, 2009.

[4] M. G. Niall. *Diagram showing recirculation of energy in CLC.* Niall, Mc. G., Licensed to Public Domain, 2009.

[5] Y. Shigeru K. Kiribayashi Toshitsugu, T. and T. Hiroshi. Particle and bubble movements around tubes immersed in fuidized beds.a numerical study. 1993.

[6] P. A. Cundall and O. D. L. Strack. Geotechnique. 1979.

[7] Kawaguchi T. Tsuji, Y. and T. Tanaka. Discrete particle simulation of two-dimensional fluidized bed. 1993.

[8] H. Mikami, T. Kamiya and M. Horio. Numerical simulation of cohesive powder behavior in fluidized bed. 1998.

[9] Mikami T. Kuwagi, K. and M. Horio. Numerical simulation of metallic solid bridging particles in a fluidized bed at high temperature. 2000.

[10] G. C. Kuczynski. *Diffusion in sintering of metallic particles.* Metal Transactions, 185:169, 1949.

[11] D. Rong and M. Horio. *DEM simulation of char combustion in a fluidized bed.* The 2nd International Conference on CFD in the Minerals and Process Industries, 65-70, 1999.

[12] Joseph D. D. Bai R. Glowinski R. Pan, T.-W. and V. Sarin. *Fluidization of 1204 spheres: simulation and experiment.* Journal of Fluid Mechanics, 2002.

[13] Hesla T. Joseph D. Pan T. W. Glowinski, R. and J. Periaux. *Distributed lagrange multiplier methods for particulate flows.* Computational Science for the 21st Century, 1997.

[14] Utsunomiya H. Shimoyama Y. Hirano H. Kuwagi, K. and T. Takami. *Examination of various estimation equations for drag force by using immersed boundary method.* Journal of Chemical Engineering, 2012.

[15] R. Kurose and S. Komori. *Drag and lift forces on a rotating sphere in a linear shear flow.* Journal of Fluid Mechanics, 1999.

[16] K. Sugioka and S. Komori. *Drag and lift forces acting on a spherical gas bubble in homogeneous shear liquid flow.* Journal of Fluid Mechanics, 2009.

[17] K. Sugioka and S. Komori. *Drag and lift forces acting on a spherical water droplet in homogeneous linear shear air flow.* Journal of Fluid Mechanics, 2007.

[18] Lohse D. Prosperetti D. A. Bluemink, J. J. and Wijngaardeen L. V. *Drag and lift forces on particles in a rotating flow.* Journal of Fluid Mechanics, 2010.

[19] H. Takagi. *Viscous flow induced by a slow rotation of a sphere.* Journal of the Pysical Society of Japan, 1977.

[20] E. M. Grugel. *Modelling the viscous torque acting on a rotating object.* Journal of Chemical Physics, 1996.

[21] P. G. Saffman. *The Lift on a Small Sphere in a Slow Shear Flow.* Journal of Fluid Mechanics, 1965.

[22] G. Magnus. *On the Deviation of Projectiles, and: On a Sinking Phenomenon Among Rotation Bodies.* Annalen der Physik, 1852.

[23] Takiguchi T. Hamasaki H. Kajishima, T. and Y. Miyake. *Turbulence Structure of Particle-Laden Flow in a Vertical Plane Channel Due to Vortex Shedding.* JSME International Journal Series B, 2001.

[24] Annaland M. V. S. Deen, N. G. and J. A. M. Kuipers. *Direct Numerical Simulation of Complex Multi-Fluid Flows Using a Combined Front Tracking and Immersed Boundary Method.* Chemical Engineering Science Journal, 2009.

[25] van Sint Annaland M. Deen N. G. Van der Hoef, M. A. and J. A. M. Kuipers. *Numerical Simulation of Dense Gas-Solid Fluidized Beds: a Multi Scale Modeling Strategy.* Annual Review of Fluid Mechanics, 2008.

[26] Narutomi R. Yokomine T. Ebara S. Tsuji, T. and A. Shimizu. *Unsteady Three-Dimensional Simulation of Interactions Between Flow and Two Particles.* International Journal of Multiphase Flow, 2003.

[27] J.B. McLaughlin. *Inertial Migration of a Small Sphere in Linear Shear Flows.* Journal of Fluid Mechanics, 1991.

[28] Mikami T. Kuwagi, K. and M. Horio. *Numerical Simulation of Metallic Solid Bridging Particles in a Fluidized Bed at High Temperature.* Powder Technology, 2000.

[29] B. Oesterle and T. B. Dinh. *Experiment on The Lift of a Spinning Sphere in a Range of Intermediate Reynolds Numbers.* Experiments in Fluid, 1998.

[30] C. Y. Wen and Y. H. Yu. *Mechanics of Fluidization.* Chemical Engineering Progress Symposium Series, 1966.

[31] S. Ergun. *Fluid Flow through Packed Columns.* Chemical Engineering Progress, 1952.

[32] R. Di Felice. *The Voidage Function for Fluid-Particle Interaction Systems.* International Journal of Multiphase Flow, 1994.

[33] Koch D. L. Hill, R. J. and A. J. C. Ladd. *The First Effects of Fluid Inertia on Flows in Ordered and Random Arrays of Spheres.* Journal of Fluid Mechanics, 2001a.

[34] Koch D. L. Hill, R. J. and A. J. C. Ladd. *Moderate-Reynolds-Number Flows in Ordered and Random Arrays of Sphere.* Journal of Fluid Mechanics, 2001b.

[35] Di Renzo A. Cello, F. and F. P. Di Maio. *A Semi-Smpirical Model for the Drag Force and Fluid-Particle Interaction in Polydisperse Suspensions.* Chemical Engineering Science Journal, 2010.

[36] L. Schiller and A. Z. Naumann. *Uber die grundlegenden Berechnungen bei der Schwerkraftaufbereitung.* Zeit. Ver. Dert. Ing., 1933.

[37] F. M. White. *Viscous Fluid Flow.* McGraw Hill, New York, 1991.

[38] Shimoyama Y. Shima T. Mokhtar M. A. Alias A. Kuwagi, K. and H. Hirano. *Numerical Study of Drag Force Acting on Dense Particles with Immersed Boundary (IB) Method.* 2nd Asian Conference on Innovative Energy and Environmental chemical Engineering, 2010b.

[39] Utsunomiya H. Shimoyama Y. Hirano H. Kuwagi, K. and T. Takami. *Direct Numerical Simulation of Fluidized Bed with Immersed Boundary Method.* Fluidization XIII, 2010a.

[40] Mikami T. Rong, D. G. and M. Horio. *Particle and bubble movements around tubes immersed in Fuidized beds.a numerical study.* Chemical Engineering Science, 1999.

[41] Fernando J. M. Bodhisattwa, C. and M. S. Tomassone. *Experimentally Validated Computations of Heat Transfer in Granular Materials in Rotary Calciners.* Powder Technology, 2010.

[42] Rong D. Morikawa, H. and M. Horio. *DEM Simulation of Bubbling Fluidized Bed including Char Combustion and Cooling by Immersed Tubes.* Proceedings of the 6th SCEJ symposium of fluidization, 2000.

[43] W. E. Ranz and W. R. Marshall. *Evaporation from drops. Parts I and II.* Chemical Engineering Progress, 1952.

[44] Hirano H. Kuwagi, K. and T. Takami. *Experimental and Numerical Study on Heat Transfer Between Two spheres.* JP Journal of Heat and Mass Transfer, 2007.

[45] Cong P. Fujiwara S. Zhang, X. and M. Fujii. *Numerical Simulation of Thermal Contact Resistance – A New Calculation Method in Cylindrical Coordinates.* Thermal Science and Eng., The Japan Society of Heat Transfer, 2002.

[46] http://www.ansys.com/products/fluid dynamics/fluent/.

APPENDIX A

IMPORTANT TABLE

Appendix A goes here. Table A.1 is copied from Chapter 2.

Table A.1: Numerical analysis method for solid-gas two-phase flow

	Fluid	Powder	Appicability	Computer load
Two-Fluid Model (TFM)	Euler	Euler	Low	Low
DSMC	Euler	Lagrange	Medium	Medium
DEM	Euler	Lagrange	Medium $\sim$ high	Medium $\sim$ high
DNS	Euler	Boundary	High	High

APPENDIX B

MORE DATA

Appendix B goes here. Table B.1 is copied from Chapter 3.

Table B.1: Simulation conditions

Particle diameter $[m]$	$1.0\times\ 10^{-3}$
Particle density $[kg/m^3]$	$2.65\times\ 10^{3}$
Particle number	1
Gas density $[kg/m^3]$	1.20
Gas viscosity $[Pas]$	$1.86\times\ 10^{-5}$
Case 1 (Saffman force)	
Particle Reynolds number Re_{p} [-]	$1.374, 3.434, 13.74, 68.68, 137.4, 274.4, 480.8$
Dimensionless velocity gradient : $a^* = \frac{r_{\mathrm{p}}\partial w}{w_{\mathrm{i}}\partial x}$	0.1
Case 2 (Magnus force)	
Particle Reynolds number Re_{p} [-]	$1.099, 5.495, 32.97, 65.93, 82.42, 109.9$
Rotation Reynolds number Re_{R} [-]	$0.137, 0.275, 0.412, 0.549, 0.687, 1.374$
Case 3 (Viscous torque)	
Rotation Reynolds number Re_{R} [-]	$0.137, 0.275, 0.412, 0.549, 0.687, 1.374$

APPENDIX C

MORE DATA

Appendix C goes here. Table C.1 is copied from Chapter 3.

Table C.1: Analysis area and calculation mesh conditions

Case number	L/d_p	T/d_p	Δ/d_p	δ/Δ
1-1	5	1	1/10	1/4
1-2	5	5	1/10	1/4
1-3	10	1	1/10	1/4
1-4	10	1	1/20	1/4
1-5	10	1	1/10	1/10
1-6	10	1	1/10	1/15
1-7	10	1	1/10	1/20
2-1	5	1	1/10	1/4
2-2	5	5	1/10	1/4
2-3	5	1	1/20	1/4
2-4	10	1	1/10	1/4
2-5	10	1	1/20	1/4
2-6	10	1	1/10	1/10
2-7	10	1	1/10	1/15
2-8	10	1	1/10	1/20
3-1	5	1	1/10	1/4
3-2	10	1	1/10	1/4
3-3	5	1	1/20	1/4
3-4	5	1	1/10	1/10
3-5	5	1	1/10	1/15

Δ : Simulation mesh size

δ : Simulation sub- mesh size

APPENDIX D

MORE DATA

Appendix D goes here. Table D.1 is copied from Chapter 4.

Table D.1: Simulation conditions for drag force

Particle diameter $[m]$	1.0×10^{-3}
Particle density $[kg/m^3]$	2.65×10^3
Particle number	1, 5, 9, 12, 16, 25
Voidage [-]	0.476, 0.665, 0.707, 0.812, 0.895, 0.979
Gas density $[kg/m^3]$	1.20
Gas viscosity $[Pas]$	1.86×10^{-5}
Particle Reynolds number Re_{p} [-]	0.1, 0.5, 1, 5, 10, 50, 100, 300
Computational grid size $[m]$	Case 1, 2, 4, 5, 6, 7, and 9 : $\Delta x = \Delta y = \Delta z = 5.0 \times 10^{-5}$, Case 3 : $\Delta x = \Delta z = 4.01 \times 10^{-5}$, $\Delta y = 5.0 \times 10^{-5}$ Case 8 : $\Delta x = 4.31 \times 10^{-5}$, $\Delta z = 4.97 \times 10^{-5}$, $\Delta y = 5.0 \times 10^{-5}$
Column witdh and height $[m]$	Case 1, 2, 4, 5, 6, 7, and 9 : $5.0 \times 10^{-3}, 5.0 \times 10^{-3}$, Case 3 : $4.01 \times 10^{-3}, 4.01 \times 10^{-3}$ Case 8 : $4.31 \times 10^{-3}, 4.97 \times 10^{-3}$
Column thickness $[m]$	1.0×10^{-3}

APPENDIX E

MORE DATA

Appendix E goes here. Table E.1 is copied from Chapter 5.

Table E.1: Properties of sphere and air

Properties	sphere	air
$\rho\ [kg \cdot m^{-3}]$	7930	1.205
$c_p\ [J \cdot kg^{-1}K^{-1}]$	500	718
$\lambda\ [W \cdot m^{-1}K^{-1}]$	1,5,8,16.8	0.0257
$\mu\ [Pa \cdot s]$	-	1.512×10^{-5}

APPENDIX F

MORE DATA

Appendix F data goes here. Table F.1 is copied from Chapter 5.

Table F.1: Infra-Red Thermo Camera

Model	TH9100 Pro Series (NEC Inc.)
Temperature measurement	Range1: $20 \sim 126$, $100 \sim 176$ °C Range2: $0 \sim 124$, $250 \sim 176$ °C
Temperature resolution	$0.06 \sim 176$ °C
Focus range	$30cm \sim \infty$
Angle of view	Horizontal $21.7 \sim 176$ Vertical $16.4 \sim 176$
Sampling frames speed	60 frame/s
Effective pixels	320 (H) ~ 180, 240 (V) dots
Depth of data	4 bits
Measurement mode	Run/Freeze
Auto functions	Full-auto, Level-trace, Auto-gain controller
Real time recording image resolution	1664 pixels
Dimensions	L $189 \sim 180$, W $108 \sim 180$, H 113 mm
Weight	$1.4kg$ (without battery)
Long wavelength spectral range	$(8\mu m \sim 14\mu m)$
Effective pixels	41 Megapixels
Minimum sensitivity	1 Rucks
Proximity magnifying lens	$95\mu m$
Focal length	$17mm$ Fix focal

APPENDIX G

MORE DATA

Appendix G data goes here. Table G.1 is copied from Chapter 5.

Table G.1: 3D Ultraviolet laser profile microscope specifications

Model	Microscope Head VK-9710 (KEYENCE. Inc)
Controller	VK-9700 (KEYENCE. Inc)
Objective lens magnification	$10\times \sim 150\times$
Observation range (horizontal)	$1350\mu m \sim 90\mu m$
Observation range (vertical)	$1012\mu m \sim 67\mu m$
Operation distance	$16.5mm \sim 0.2mm$
Height measurement range	$7mm$
Resolution display	$0.001\mu m$
Repeat accuracy	$0.02\mu m$
Weight	Microscope head: $26kg$; Controller: $11kg$

APPENDIX H

MORE DATA

Appendix H data goes here. Table H.1 is copied from Chapter 5.

Table H.1: Heating equipment specifications

Voltage slider	
Model	N-130-10 YAMABISHI ELECTRIC
Heating mantle with cylinder	
Measurement (Diameter × Length)	$20 \times 100mm$
Maximum Temperature	$400 \sim$ °C
Power Supply Voltage	AC100V

APPENDIX I

MORE DATA

Appendix I data goes here. Table I.1 is copied from Chapter 5.

Table I.1: Particle Image Velocimetry (PIV) system specifications.

Double pulse YAG Laser Source	
Model	PV200 (B.M. Industries)
Laser type	Double Pulse Nd: YAG Laser
Pulse interval	$5 \sim 20ns$
Pulse energy	$10mJ \sim 3.0J$
Laser wavelength	$532nm$
Lens type	Concave with focal length = 1000 mm
Power supply	AC 200V; 50 - 60Hz
Synchronizer	
Model	610032 Laser Pulse Synchronizer (TSI Inc.)
Power Supply	ACV 100; 50-60 Hz
Input	External synchronizer Photo camera feedback signal Image shifter system signal
Output	Flash lamp Q switch trigger signal Mirror image shifter trigger signal
CCD Camera	
Model	PIVCAM 10 - 30 CCD Camera (Kodak Inc.)
CCD type	Progressive Scan Interline CCD
Effective pixels	$1000 \sim 1016$ pixels
Pixel format	$9\mu m \sim 9\mu m$
Frame rate	30 fps (Max)
Telezoom Lens	AF NIKKOR 24 - 50 mm F3 (Nikon Inc.)

APPENDIX J

MORE DATA

Appendix J data goes here. Table J.1 is copied from Chapter 5.

Table J.1: PC specification for simulation

Model	ASUS
CPU	Intel Celeron (R) 2.4GHz
Memory	1.4GB
OS	Windows XP Professional

APPENDIX K

MORE DATA

Appendix K data goes here. Table K.1 is copied from Chapter 5.

Table K.1: Experiment conditions

Particle diameter (SUS304) [m]	0.0191
Particle mass [kg]	2.82×10^{-2}
Specific heat $[J \cdot kg^{-1}K^{-1}]$	0.50×10^{3}
Young modulus [GPa]	184.36 at 150°C
Gas viscosity $[Pa \cdot \mathrm{s}]$	1.512×10^{-5}
Poisson ration [-]	0.29
Heated temperature [°C]	50, 100, 150
Contact force [N]	100, 200, 300, 400, 500